



Fundamental studies on the catalytic properties of manganese oxides in oxidation reactions

Der Fakultät für Chemie der Universität Duisburg-Essen zur Erlangung des
akademischen Grades

Dr. rer. nat.

vorgelegte Dissertation

von

Niklas Cibura

aus

Münster

Max-Planck-Institut für Chemische Energiekonversion

2019

“When you change the way you look at things, the things you look at change.”

— Max Planck

Die vorliegende Arbeit wurde vom 01.09.2015 bis zum 30.06.2019 in der Forschungsgruppe „Nanobased Heterogeneous Catalysts“ unter Betreuung von Herrn Prof. Dr. Robert Schlögl am Max-Planck-Institut für chemische Energiekonversion in Mülheim an der Ruhr angefertigt.

DuEPublico

Duisburg-Essen Publications online



Offen im Denken



Diese Dissertation wird über DuEPublico, dem Dokumenten- und Publikationsserver der Universität Duisburg-Essen, zur Verfügung gestellt und liegt auch als Print-Version vor.

DOI: 10.17185/duepublico/70448
URN: urn:nbn:de:hbz:464-20190903-084613-5

Alle Rechte vorbehalten.

Datum der mündlichen Prüfung: 12.08.2019

Vorsitzender: Prof. Dr. Stefan Rumann

1. Gutachter: Prof. Dr. Robert Schlögl
2. Gutachter: Prof. Dr. Jennifer Strunk

Acknowledgments

First, I would like to thank Prof. Dr. Robert Schlögl for giving me the opportunity to conduct this work at the Max Planck Institute for Chemical Energy Conversion and guiding this work to fruition.

Furthermore, I want to thank Prof. Dr. Frank Neese for accepting me in the International Max Planck Research School on Reactive Structure Analysis for Chemical Reactions (IMPRS – RECHARGE) and the coordinator of the school Rita Gröver for enabling every member of RECHARGE to learn, discuss, exchange and sequentially grow from the opportunities presented to us.

Next, my heartfelt gratitude goes to all my working group “Nanobased Heterogeneous Catalysts (NanoCat)”, former and current members alike: Prof. Dr. Jennifer Strunk for guiding the first years of my research and the continuous support she has been lending our group till today, Dr. Simon Ristig for guiding our group and defending our interests from the very first day he acquired the position of group leader, Alina Jakubowski for the invaluable work she conducted for us (including BET, XRD and syntheses that were used in this work), Martin Dilla, Thomas Lange and Dr. Ahmet Becerikli for their never ceasing support with any task, failing or successful attempts alike.

There was not a single day during my work in this group in which I did not enjoy the company of all of them and I view myself lucky to have found such great coworkers and friends.

I also want to thank all other members of the MPI CEC for the years of cooperation, productive exchange and the good times we shared. At this point I want to especially thank, Fabian Wachholz and Pascal Düngen for the Raman measurements they have done or helped me with.

Furthermore, I would like to thank the people from the Fritz-Haber Institute in Berlin as well who received me with open arms during my long measurement periods. Again I want to especially thank those who helped me with my research: Dr. Annette

Trunschke for giving me guidance on catalysis and the opportunity for all the 2-propanol measurements, Dr. Pierre Kube and Marie-Mathilde Millet for all the help with the 2-propanol oxidation set-up and the data interpretation and Dr. Frank Girgsdies for all the XRD knowledge he provided which I was missing, including the Rietveld analysis.

I want to thank all the members of the NanoEnergieTechnikZentrum (NETZ), especially the groups of Dr. Galina Marzun and Prof. Dr. André Gröschel who made working there a true pleasure. Also, I want to thank Sebastian Rosendahl for all the technical support he has been lending our group over the past three years.

I want to thank all the members of IMPRS-RECHARGE for the fun and productive exchange we had and the great discussions we shared during our time in the research school.

Last, I want to thank my family who supported me all these years during my work and especially my girlfriend Annika Wagstyl who had to cope with all my frustration and anguish over unsuccessful experiments and failed attempts. She never stopped believing in me and supported me during all these years.

Thank you for being at my side!

Abstract

Manganese oxides are a commonly employed, cheap and abundant option for oxidation catalysis. Although increasingly complex Mn-based materials like todorokites or birnessites recently gained attention, only few comparative studies of the different fundamental binary MnO_x phases can be found.

As spectroscopy often induces irradiation damage in this class of compounds, an alternative physico-chemical route is required to ensure phase purity of these samples. In the first part of this work temperature programmed oxidation (TPO) and temperature programmed reduction (TPR) are shown to be able to fill this role and completely analyze the composition of even a mainly amorphous manganese oxide sample. Raman spectroscopy and X-ray diffraction (XRD) are shown to perfectly complement these investigations. Based on these methods, a comprehensive characterization of four binary MnO_x phases of highest purity is presented here.

In the second part of this work the performance of the binary oxides is examined in two catalytic reactions, the total oxidation of CO to CO_2 and the partial oxidation of 2-propanol. For the second reaction a 100% selectivity to acetone was found for all samples. The specific catalytic behavior of the samples in the two test reactions indicates a higher activity of the Mn(II)/Mn(III) pair in partial oxidation and of Mn(III)/Mn(IV) in total oxidation reactions, respectively.

As the analysis of the samples after catalytic testing revealed no changes in the bulk structure of MnO, Mn_3O_4 and $\alpha\text{-Mn}_2\text{O}_3$, a correlation of bulk properties and catalytic behavior was examined. The Mn-O bond lengths and the work function of the material seem to be suitable to explain the catalytic behavior observed here.

Zusammenfassung

Manganoxide sind in ihrer Anwendung weit verbreitet, günstig und in großer Menge in der Kruste unseres Planeten vorhanden. Auch in der Oxidationskatalyse finden sie weithin Anwendung. Obwohl zunehmend komplexe Mn-Materialien wie Todorokite oder Birnessite besonders in jüngster Vergangenheit ausgiebig erforscht werden, sind vergleichende Studien zu den grundlegenden binären Manganoxiden sehr selten.

Da es bekannt ist, dass spektroskopische Methoden häufig Strahlschäden in dieser Materialklasse erzeugen, ist eine Kombination von physico-chemischen Methoden notwendig, die eine phasenreine Untersuchung ermöglichen. Zu diesem Zweck wurde im ersten Abschnitt dieser Arbeit gezeigt, dass die temperaturprogrammierte Oxidation (TPO) und die temperaturprogrammierte Reduktion (TPR) in der Lage sind diese Funktion zu erfüllen und sogar vorwiegend amorphe Proben vollständig in ihrer Zusammensetzung zu untersuchen. Zudem wurde gezeigt, dass Raman-Spektroskopie und Röntgenbeugung (XRD) ideale komplementäre Techniken für diese Untersuchungen darstellen. Die Daten wurden an vier höchstreinen binären MnO_x erhoben.

Der zweite Abschnitt dieser Arbeit befasst sich mit der Untersuchung der katalytischen Eigenschaften der vier binären Oxide in zwei Oxidationstestreaktionen: Die Totaloxidation von CO zu CO_2 und die Partialoxidation von 2-Propanol. Für die zweite Reaktion konnte eine Selektivität von 100% zu Aceton für alle Proben gefunden werden. Des Weiteren wurden unterschiedliche Reaktivitäten der Proben in den beiden Testreaktionen festgestellt. Die Ergebnisse deuten auf eine höhere Aktivität des Mn(II)/Mn(III) Redox-Paares in der Partialoxidation und des Mn(III)/Mn(IV)-Paares in der Totaloxidation hin.

Bei der Analyse der Proben nach Einsatz in den Testreaktionen wurde festgestellt, dass sich MnO , Mn_3O_4 und $\alpha\text{-Mn}_2\text{O}_3$ strukturell nicht verändern. Aus diesem Grund wurde Zusammenhänge zwischen Bulkeigenschaften und den Ergebnissen der Testreaktionen untersucht. Hierbei scheinen die Bindungslänge der Mn-O Bindung und die Austrittsarbeit am besten zur Erklärung der katalytischen Eigenschaften geeignet.

Contents

Contents	VIII
List of Abbreviations	X
List of Figures	XI
List of Tables	XVI
1. Introduction	1
1.1 Motivation.....	1
1.2 Theoretical background.....	3
1.2.1 An evaluation of the current energy system	3
1.2.2 Energy storage on a world scale	7
1.2.3 Hydrogen from water splitting.....	8
1.2.4 Industrial application of manganese (oxides)	10
1.2.5 Physico-chemical properties of MnO _x	12
1.3 Scientific objective of this work	16
2. Methods and techniques.....	17
2.1 Vibrational spectroscopy	17
2.2 Catalytical CO and 2-propanol oxidation.....	23
2.2.1 Introduction to catalysis	23
2.2.2 MnO _x in CO and 2-propanol oxidation	26
2.3 Temperature programmed oxidation/reduction	28
3. Experimental.....	37
3.1 Sample supply	37
3.2 Characterization and methods	37
3.2.1 Raman spectroscopy.....	37
3.2.2 Temperature programmed oxidation and reduction.....	38
3.2.3 CO and 2-propanol oxidation.....	38
3.2.4 Powder X-ray diffraction	39
3.2.5 N ₂ and krypton physisorption experiments	40

Contents

4. Phase identification of Mn oxides	41
4.1 Characterization of the high purity Mn oxides	41
4.2 Temperature programmed oxidation	43
4.2.1 Parameter variation	43
4.2.2 TPO of high purity Mn oxides	46
4.2.3 Investigation of MnO _x samples of unknown composition.....	52
4.3 Temperature programmed reduction	56
4.4 Raman spectroscopy of the high purity samples.....	59
5. Catalysis of Mn oxides.....	67
5.1 Sample selection and characterization.....	67
5.2 CO oxidation over MnO _x	75
5.3 2-propanol oxidation over MnO _x	82
5.3 Comparison of MnO _x in the two oxidation test reactions.....	91
6. Correlation between catalytic behavior and bulk properties.....	93
7. Conclusion and Outlook.....	100
8. References	102
9. Eidesstattliche Erklärung	111
10. Curriculum Vitae	112

List of Abbreviations

BET	Brunauer-Emmet-Teller
CAES	Compressed air energy storage
CCD	Charge-coupled device
FT	Fourier transformed
ICSD	International Crystal Structure Database
IEP	Isoelectric point
IPCC	Intergovernmental Panel on Climate Change
IR	Infrared
MvK	Mars-van-Krevelen
PS II	Photosystem II
PV	Photovoltaic
PZC	Point of zero charge
PXRD	Powder X-ray diffraction
TPO	Temperature programmed oxidation
TPR	Temperature programmed reduction
UV	Ultraviolet
vis	visible
WF	Work function
XRD	X-ray diffraction

List of Figures

Figure 1: Primary energy consumption per capita in GJ from 1990 to 2016 for selected examples. <small>data from [11]</small>	3
Figure 2: Primary energy world consumption in million tonnes oil equivalents from 1991 to 2016. ^[12]	4
Figure 3: a) World CO ₂ emissions per year in Mt from 1994 to 2016. <small>data from [11]</small> b) Atmospheric CO ₂ concentration measured by the ESRL Global Monitoring Division in Mauna Loa in ppm from 1974 to 2017. <small>data from [13]</small>	5
Figure 4: Change in the stored energy content of our planet in oceans, land and atmosphere including the measurement uncertainties in ZJ from 1971 to 2011 measured for the 5 th assessment report of the IPCC. ^[14]	6
Figure 5: Potential energy V for a diatomic molecule over the atom distance r calculated for the models of the harmonic oscillator and the Morse potential.....	18
Figure 6: Commonly observed fundamental vibrations of a molecule. <small>adapted from [77]</small> ..	19
Figure 7: Illustration of the absorption and scattering events in IR and Raman spectroscopy. <small>adapted from [76]</small>	20
Figure 8: Schematic plot of a Raman spectrum depicting Stokes, Anti-Stokes and Rayleigh lines and indicating relative intensities. <small>adapted from [76]</small>	21
Figure 9: Potential energy for an uncatalyzed (black) and catalyzed (red) chemical reaction leading from reactants to products. Additionally, the activation energy E_A and the reaction enthalpy ΔH are illustrated. <small>adapted from [78]</small>	24
Figure 10: Sequence of steps in the reduction (left to right) of a metal oxide to metal according to the contracting sphere model. The inner grey space represents the initial oxide phase and the shade area represents the growing metal phase during the reduction process. r_0 is the initial radius of the metal oxide and r_1 is the current radius of the oxide particle.	30
Figure 11: Degree of reduction α over time for the contracting sphere model.....	30
Figure 12: Sequence of steps in the reduction (left to right) of a metal oxide to metal according to the nucleation model. The inner grey space represents the initial oxide phase and the shade area represents the growing metal phase during the reduction process.....	31

Figure 13: Degree of reduction α over time for the nucleation model.	32
Figure 14: Exemplary $\ln(T_M^2/\beta)$ vs $1/T_M$ plot for the determination of E_A from the slope m and k_0 from the intercept with the y-axis.	34
Figure 15: Measured XRD data and reference line spectra for all manganese oxide samples. Additionally, Laue indices are given for all individual reflexes.	41
Figure 16: Rietveld refinement of all investigated samples depicting the measured XRD pattern (black), the fitted data (red) and the difference between those two (grey).	42
Figure 17: TPO profiles of MnO for heating rates of 2 and 10 K/min in the temperature domain (left) and the time domain (right).	43
Figure 18: TPO profiles of MnO at a heating rate of 2 K/min with an initial oxygen concentration of 1, 2 and 5 vol-%.	45
Figure 19: TPO data of MnO and the chemical transitions during the reaction.	46
Figure 20: Left: XRD pattern of the sample formed from MnO in the TPO experiment stopped at 700 °C and a reference line pattern of α -Mn ₂ O ₃ . Right: XRD pattern of the sample formed from MnO at the end of the TPO experiment at 1000 °C and a reference line pattern of Mn ₃ O ₄	47
Figure 21: TPO data of Mn ₃ O ₄	48
Figure 22: TPO data of α -Mn ₂ O ₃ and the chemical transition during the reaction. ...	49
Figure 23: TPO data of β -MnO ₂ and the chemical transitions during the reaction. ...	50
Figure 24: TPO data of all high purity MnO _x samples. The temperature regimes of the main transitions are indicated at 550 °C and 800 °C. The Y-axis was offset for better visibility. The baseline concentration was 1.1 vol-% of O ₂	51
Figure 25: Left: Measured XRD pattern of the unknown precipitated sample calcined at 800 °C and a reference line pattern of α -Mn ₂ O ₃ . Right: TPO measurement of the same sample highlighting the peak temperatures and giving the calculated quantification of the reaction.	52
Figure 26: Left: Measured XRD pattern of the unknown precipitated sample calcined at 600 °C and a reference line pattern of α -Mn ₂ O ₃ . Right: TPO measurement of the same sample highlighting the peak temperatures and giving the calculated quantification of the reaction.	53

Figure 27: Left: Measured XRD pattern of the unknown precipitation sample without calcination and a reference line pattern of Mn_3O_4 . Right: TPO measurement of the same sample highlighting the peak temperatures and giving the calculated quantification of the reaction.....	54
Figure 28: TPR data of all high purity MnO_x samples. The temperature regimes of the main transitions are indicated with dashed lines. The Y-axis was offset for better visibility.	56
Figure 29: Raman spectrum of bulk MnO measured using a 532 nm and a 780 nm laser.....	60
Figure 30: Raman spectrum of bulk Mn_3O_4 measured using a 532 nm and a 780 nm laser.....	61
Figure 31: Raman spectrum of bulk α - Mn_2O_3 measured using a 532 nm and a 780 nm laser.....	63
Figure 32: Raman spectrum of bulk β - MnO_2 measured using a 532 nm and a 780 nm laser.....	65
Figure 33: Raman spectra of all high purity MnO_x samples with characteristic features highlighted in red. The intensity of Mn_3O_4 has been scaled for better comparability of the data.....	66
Figure 34: XRD patterns of the new sample batches of MnO and the reference line pattern of MnO.....	67
Figure 35: Left: TPO data of the new sample batches of MnO. The Y-axis was offset for better visibility. The baseline concentration was 1.1 vol-% O_2 . Right: Raman spectra of the new sample batches of MnO.....	68
Figure 36: XRD patterns of the new sample batches of Mn_3O_4 and the reference line pattern of Mn_3O_4	69
Figure 37: Left: TPO data of the new sample batches of Mn_3O_4 . The Y-axis was offset for better visibility. The baseline concentration was 1.1 vol-% O_2 . Right: Raman spectra of the new sample batches of Mn_3O_4	70
Figure 38: XRD patterns of the new sample batches of Mn_2O_3 and the reference line pattern of Mn_2O_3	70

Figure 39: Left: TPO data of the new sample batches of Mn_2O_3 . The Y-axis was offset for better visibility. The baseline concentration was 1.1 vol-% O_2 . Right: Raman spectra of the new sample batches of Mn_2O_3	71
Figure 40: XRD patterns of the new sample batches of MnO_2 and the reference line pattern of MnO_2	71
Figure 41: Left: TPO data of the new sample batches of MnO_2 . The Y-axis was offset for better visibility. The baseline concentration was 1.1 vol-% O_2 . Right: Raman spectra of the new sample batches of MnO_2	72
Figure 42: Results of the XRD analysis depicting the measured XRD pattern (black), the fitted data after the method of Rietveld (red), the difference between those two (grey) and the reference pattern from ICSD (green). Additionally, the Laue indices are given above the individual reflexes.	73
Figure 43: CO conversion of all MnO_x samples and inert SiC during a heating ramp of 10 K/min.	75
Figure 44: Rate of CO_2 formation normalized to the Krypton BET specific surface area for all MnO_x samples and SiC.	76
Figure 45: Arrhenius plots for all MnO_x samples and the respective apparent activation energies in the CO oxidation.	77
Figure 46: Determination of the O_2 reaction orders for all MnO_x samples in the CO oxidation.	78
Figure 47: Determination of the CO reaction orders for all MnO_x samples in the CO oxidation.	79
Figure 48: Product selectivities towards acetone (left) and CO_2 (right) as a function of the temperature in the 2-propanol oxidation for all MnO_x samples.	82
Figure 49: Conversion (left) and acetone formation rate normalized to the Krypton BET surface area (right) during a heating ramp in the oxidation reaction of 2-propanol for all MnO_x samples.	83
Figure 50: Acetone formation during the removal of oxygen from the reaction feed in the 2-propanol oxidation for all MnO_x samples. The time between two measurements is 45 min for all samples.	84
Figure 51: Arrhenius plots for all MnO_x samples and the respective apparent activation energies in the 2-propanol oxidation.	85

List of Figures

Figure 52: Determination of the 2-propanol reaction orders for all MnO _x samples in the 2-propanol oxidation.	86
Figure 53: Determination of the O ₂ reaction orders for all MnO _x samples in the 2-propanol oxidation.	87
Figure 54: Acetone evolution during the 16 h of steady state conditions for all MnO _x samples in the 2-propanol oxidation.	88
Figure 55: TPO analysis for the post-mortem samples after 16 h of steady state conditions. The Y-axis is offset for better visibility. The baseline of all samples is 1.0 vol-% of O ₂	88
Figure 56: Results of the XRD analysis after catalysis depicting the measured XRD pattern (black), the fitted data after the method of Rietveld (red), the difference between those two (grey) and the reference pattern from ICSD (green and violet). Additionally, the Laue indices are given above the individual reflexes.	89
Figure 57: Normalized product formation rates at 200 °C r_{cat} , Mn-O bond length L_{Mn-O} , enthalpy of formation ΔH^0_{298K} , mean Mn-O bond strength E_{Mn-O} and work function WF plotted against the mean oxidation state of Mn in MnO _x	98

List of Tables

Table 1: Specific surface area measured by N ₂ BET for all high purity samples.	42
Table 2: Integration results of all experiments during the parameter variation tested on MnO.....	44
Table 3: Numerical values used in the calculation of TPO stoichiometries for the high purity samples.	51
Table 4: Numerical data used in the calculation of the initial composition of the non-calcined precipitation sample.....	55
Table 5: Numerical values used in the calculation of TPR stoichiometries for the high purity samples.	57
Table 6: List of all observed Raman bands, their assignments and the respective references for all MnO _x samples.....	62
Table 7: Refined lattice parameters, domain sizes and microstrain (with estimated standard deviations) obtained from the Rietveld fits.....	73
Table 8: Specific surface area measured by N ₂ and Krypton BET for the selected MnO _x samples.	74
Table 9: Compiled apparent activation energies E_A and reaction orders a for all MnO _x samples in the CO oxidation.....	80
Table 10: Apparent activation energies E_A and reaction orders a in the CO oxidation for a variety of non-supported metal oxide materials from literature.....	81
Table 11: Compiled apparent activation energies and reaction orders for all MnO _x samples in the low temperature (≤ 210 °C) 2-propanol oxidation.	90
Table 12: Compilation of all numerical values obtained in the catalytic test reactions of CO and 2-propanol oxidation for all MnO _x samples.....	92
Table 13: Literature values for the enthalpy of formation ΔH^0_{298K} and Gibbs energy of formation ΔG^0_{298K} at RT. ^[121]	94
Table 14: Measured band gap energies E_g from literature. Compare also chapter 1.2.5. ^[121]	95
Table 15: Literature values for the Mn-O bond length, bond strength and the work function.....	97

1. Introduction

1.1 Motivation

The society of humankind as we know it today is built upon a vast energy usage and with increasing world population and an ever more digitalized world the demand for energy is continuously rising. This energy has to be low in entropy and a possibility for storage is needed to achieve a steady supply available at all times. At the present time fossil fuels are used to cover these demands, due to their (still) high availability and high energy density. But in a long-term perspective these resources will not be able to cover the energy demands of the world due to their fossil nature. The planet has built the reservoirs of fossil fuels we use today over millions of years, which is orders of magnitude slower than our consumption speed due to the ever-growing demand for energy. Therefore, a long term stable and renewable supply of energy has to be utilized to satisfy the energy demand in the future. Solar energy is the most prominent source of renewable energy, because the sun provides the highest amount of energy to the earth compared to other renewable sources such as wind, geothermal, tides, etc..^[1] Nowadays, photovoltaics (PV) is already widely used to harvest solar energy and turn it into electrical energy. Already today a theoretical amount of 4% of all desert surface had to be covered with PV panels to satisfy the global energy demand.^[2] But the problem of the utilization of renewable energy in an electrical form lies in the storage capabilities. So far, only few efficient long-term storages for electrical energy on a world scale have been developed which are limited by space or missing height differences in landscape, making the complete electrification of the energy system an impossible task today. On the other hand, even with long term storage possibilities for electrical energy, some tasks are, on the current technology level, hard to envision using electricity as an energy supply, i.e. aviation, naval or heavy-duty truck transport. It is likely, that long-term chemical energy supplies (fuels) will be needed for these assignments in times to come. Therefore, efficient ways to transform electrical energy into chemical energy are needed as future fuels and long-term energy storages. Quite a number of different

1. Introduction

possible routes have been proposed, e.g. in form of ammonia, methanol, hydrocarbons and more,^[3] but the most prominent idea for a chemical energy storage molecule is hydrogen from the water splitting reaction.^[1,3,4] This reaction splits water, which is quite abundant in most parts of the world, into the energy carrier hydrogen and oxygen. The latter can be released into the air, due to its non-toxic nature, making it a clean and “green” reaction. Water splitting can be driven by electricity (electrolysis), sunlight (photocatalysis) or a mixture of both (photoelectrochemically). Nowadays, the major impediment to realizing water splitting on an industrial scale to offer a commercially viable alternative to hydrogen produced from fossil fuels is finding a suitable, abundant and especially low-cost catalyst for this reaction. The state-of-the-art catalyst for this reaction is iridium oxide, which contains one of the most expensive and scarce metals on this planet. Even though good efficiencies can be achieved utilizing IrO_x in the water splitting reaction, this will never be a catalyst used on a world scale application to solve the energy problem at hand, because we simply do not have enough material. Therefore, cheap and abundant alternatives are needed. In this regard manganese oxides are promising. Manganese is the third most abundant transition metal and the 12th most abundant element overall in the crust of the earth and therefore quite cheap.^[5] Additionally, manganese is known for a highly flexible valency featuring stable oxidation states from 0 to +VII and is applied manifold in industrial oxidation catalysis.^[6–8] Furthermore, in the natural water splitting reaction performed in the Photosystem II (PSII) by plants an oxidic manganese cluster is utilized as the oxidation catalyst.^[9,10] It should be noted however, that the complex environment of the cluster, namely the protein shell around it, is of major importance for this reaction to occur, since extracting the cluster from PSII and using it as an oxidation catalyst shows no activity towards water splitting at all. Nevertheless, all of these factors make manganese an interesting candidate for further studies.

1.2 Theoretical background

1.2.1 An evaluation of the current energy system

Energy is the most important resource of humankind. Be it to keep us fed in the form of food, to keep us warm in the form of heating, to help us transport goods or ourselves in the form of mobility, to help us produce products and goods or to enjoy any other convenience through electricity. The amount of energy consumed with food and the amount of energy converted by humans has reached the same proportions already a decade ago.^[4] Our society today is built upon a vast energy consumption which is ever rising in face of world progress and an increasing world population, i.e. rising energy consumption per capita, especially in the densely populated parts of the world, which counteracts the decreasing energy needs of nations with better technological standards (compare Figure 1).^[11]

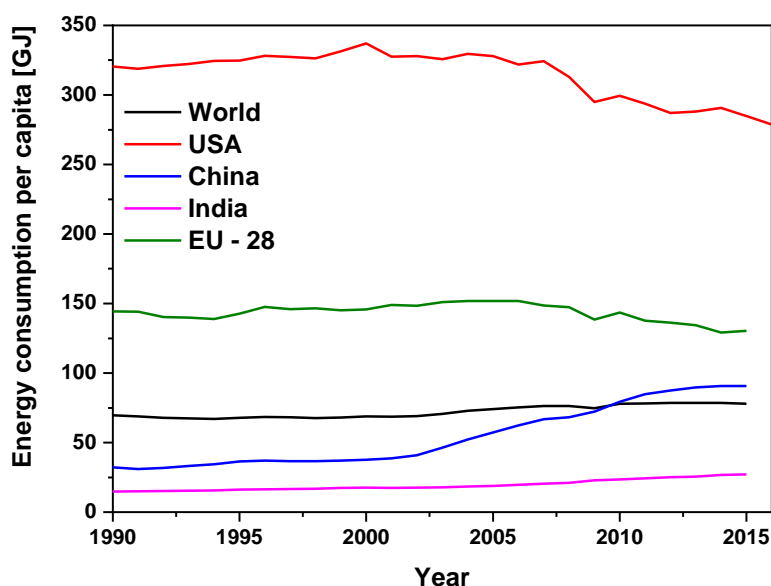


Figure 1: Primary energy consumption per capita in GJ from 1990 to 2016 for selected examples. data from [11]

Nevertheless, the current situation cannot be maintained forever due to the finite nature of our current energy supply (not regarding the food sector). In the year 2016 only 3.16% of the energy demand of the world was provided by renewable sources as depicted in Figure 2.^[12] Hydroelectricity has been depicted separately, because it

1. Introduction

is mainly an energy storage and the full carbon footprint of this technology is reliant on the rest of the energy system. The remaining energy was provided by non-renewable sources which are mainly fossil fuels. Further, the relative share of renewable energy is rising, but at the same time the overall world energy consumption is also rising, which leads to an increase in the total amount of fossil fuels consumed over the last decades.^[12] Therefore, it is imperative that the structure of our energy system changes in the future, if we are to maintain our current way of life in industrialized nations and want to evolve the technological standards in non-industrialized nations.

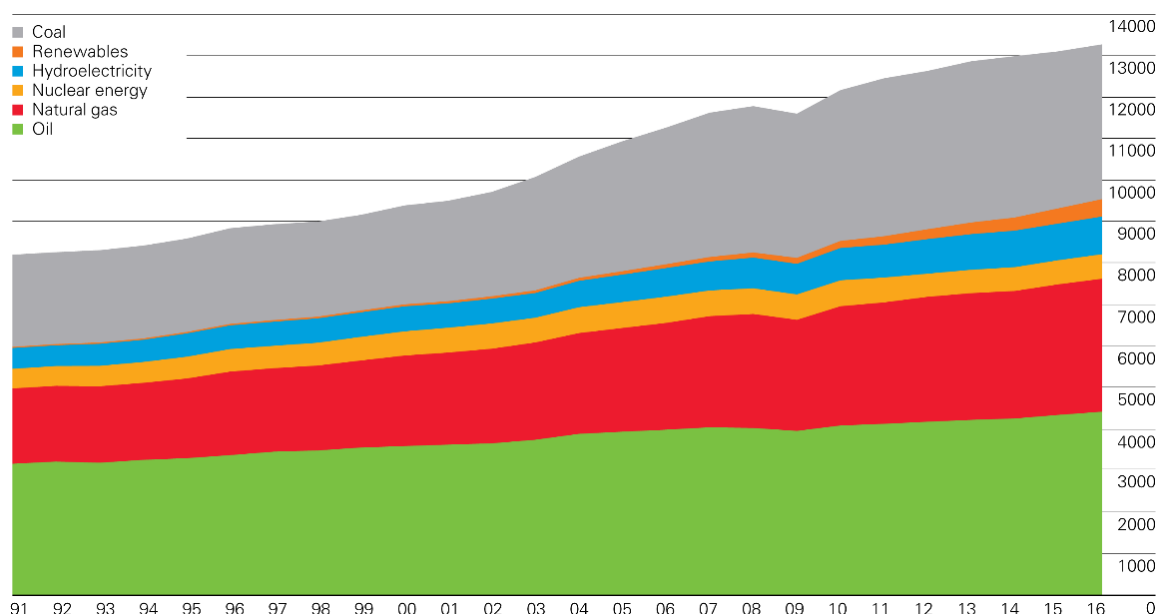


Figure 2: Primary energy world consumption in million tonnes oil equivalents from 1991 to 2016.^[12]

An additional problem which arises from the usage of fossil fuels as the main energy source of humanity are the increasing CO₂ emissions per year and therefore also the increasing CO₂ concentration in the atmosphere (compare Figure 3a and b), which leads to climate changes.^[11,13] Therefore, it is indispensable to stop the utilization of fossil fuels as energy materials even before the reserves on earth run out to protect our climate.

Global warming is widely discussed and there are even those who deny it completely, but considering the change of stored energy of our planet which was studied by the Intergovernmental Panel on Climate Change (IPCC) reveals an

1. Introduction

astonishing accumulation of energy (compare Figure 4).^[14] The ongoing debate, whether global warming exists or not, can be understood when looking at the changes of stored energy in our atmosphere and in the landmass of the planet over the last 40 years. These changes relate to the perceived change in climate for humans living on the land. Taking the uncertainty of the measurement into account the increase in energy is too small to evidently prove a warming effect for land and atmosphere. On the other hand, the energy stored in the oceans of our planet is increasing with alarming speed and even considering the uncertainty of the assessment there is no doubt that vast amounts of energy are accumulating in the oceans of our planet.

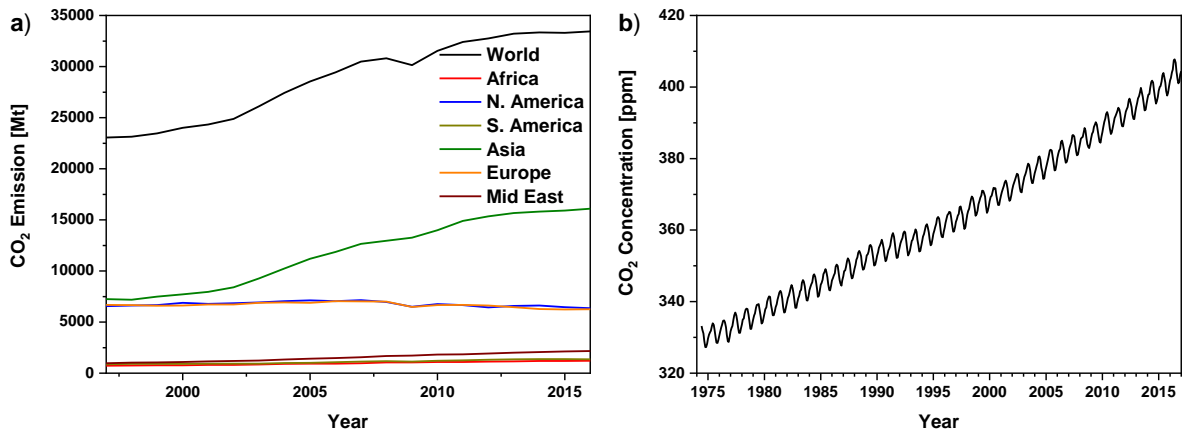


Figure 3: a) World CO₂ emissions per year in Mt from 1994 to 2016. data from [11] b) Atmospheric CO₂ concentration measured by the ESRL Global Monitoring Division in Mauna Loa in ppm from 1974 to 2017. data from [13]

The points discussed above all lead to one single conclusion: the currently employed energy system needs to change into a renewable and sustainable one, which can close all the resource cycles involved in it (e.g. the CO₂ cycle) and put less stress and burden on the environment of the planet. Unfortunately, this problem stands opposed to the problem of poverty in a big part of the world as Sir Nicholas Stern pointed out in his *Stern Review*.^[15] These are two problems which we are currently facing and it is indispensable to tackle both of them at the same time. We cannot deny poorer countries the development and progress which industrialized countries already achieved at the cost of our environment. At the same time, these nations will be consuming the most fossil fuels if they take the same development route as

1. Introduction

today's industrialized nations. Therefore, the approach Sterns took, to assess the problem from an economical point of view is very reasonable.

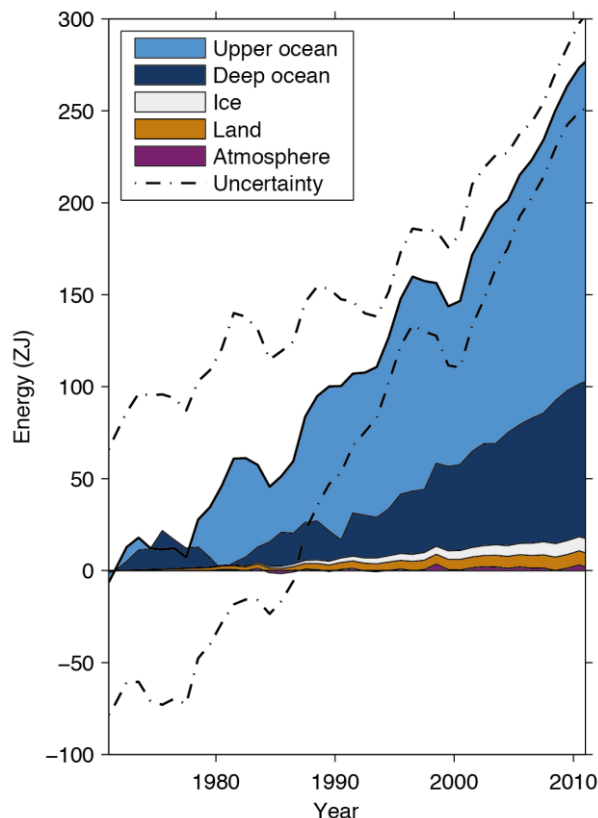


Figure 4: Change in the stored energy content of our planet in oceans, land and atmosphere including the measurement uncertainties in ZJ from 1971 to 2011 measured for the 5th assessment report of the IPCC.^[14]

The contribution of industrialized nations like Germany or even the USA to the world energy system is not big enough to solve the current crisis even by implementing 100% sustainable and renewable energy, if nations with large populations (e.g. China or India) progress to the same technological standard by utilizing fossil energy. Therefore, the most important achievements science can make today, is opening new routes and possibilities for implementing renewable energy sources and to increase the efficiency of those processes to make them economically competitive to the state-of-the-art energy system. In this way, even poor nations will invest into a sustainable energy system rather than the current one built on fossil fuels.

1.2.2 Energy storage on a world scale

The biggest difference between energy from fossil fuels and renewable energy is the form in which we extract them. Fossil fuels are storable materials (i.e. coal, oil and gas) with a high volumetric and gravimetric energy density, which is an ideal combination for energy applications.^[1] Most renewable energy on the other hand is directly interconverted into electrical energy (e.g. solar, wave, tidal or wind energy). The upside is, that electrical energy can be interconverted into any other type of energy and is one of the most useful forms of energy for humankind. The downside is, however, that we have yet to find a suitable way to store this energy. Up to now, all electrical energy is generated in the amounts in which it is consumed. We store fossil fuels and manage the electricity grid in such a manner, that we ramp our power plants up or down according to the current consumption. This bears no problems if the energy used comes from easily storable fossil fuels, but if we consider the sources of renewable energy the problem becomes evident. All renewable energy is generated by naturally occurring events (e.g. sunshine or wind) which are not constantly available, such as the sun setting in the evening and wind blowing in different strengths during the day. Therefore, we need energy storages for times in which less energy is generated than we are consuming. This could be counteracted to a certain degree by connecting electrical grids all over the world to compensate electricity shortages or overproduction.^[1] Nevertheless, energy storage is a problem of a new energy system which we did not have to face up to now.

Direct electrical storages such as capacitors or accumulators often exhibit a higher charge-discharge efficiency than other storage media due to the absence of an interconversion step from one energy form to the other.^[1] Unfortunately, these storages face issues of severe self-discharging (capacitors) or low stability (accumulators) which leads to short storage times. Therefore, such storage media are well suited for smaller timeframes and lower amounts of energy stored (electrical circuits or electrical machines), but they cannot be applied on a world scale for storing hundreds of TW energy over timescales of years.

Better options for long term storage of electrical energy are pumped hydroelectric power and compressed air energy storage (CAES).^[1] Both methods are based on a

1. Introduction

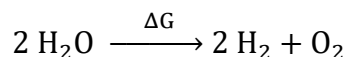
similar principle: water or air is pumped into a confined space, i.e. a mountain reservoir or underground cavern, with excess energy from the electrical grid to store this energy in form of potential energy. It can then be released through turbines at any time to reclaim the energy stored. Especially for hydroelectricity the cycle efficiencies are very good with roughly 80% making this technique the current state of the art electrical energy storage and the benchmark for every other storage medium. The downside of these techniques is the geographical need for suitable storage places. Due to the enormous dimensions of the energy system, it is unlikely to have all grid scale energy storage in the form of geographically restrained storage, even more so considering the wish of every individual nation to have enough energy stored to function independently from other nations. Thus, pumped hydroelectricity and CAES will surely help to provide some of the much-needed storage capacity for renewable energy, but a more localized and transportable storage option is still required, in the sense of an energy point source which can be applied everywhere. The only candidate for these requirements is a chemical energy storage very similar to fossil fuels which has a high volumetric or gravimetric energy density or even both.

1.2.3 Hydrogen from water splitting

Hydrogen is one of the centerpiece molecules in most renewable energy scenarios due to the versatility in the utilization of this molecule. It could be used as a direct energy storage molecule due to its storability (in orders of months and years) and high gravimetric energy density. Additionally, hydrogen has the advantage of a rich chemistry able to convert molecules of low energy density and a relatively high carbon footprint, in the case of organic compounds, into molecules of higher energy density at the same carbon footprint due to energy storage in additional H-bonds. Different predictions of energy scenarios are available, which range from pure hydrogen economy over hydrogen enriched biomass as new energy carriers all the way to an ammonia-based energy system.^[1,3] Nevertheless, hydrogen is the central compound which needs to be produced by renewable means often referred to as “green hydrogen” to realize any of the above scenarios or a mix of all of them.

1. Introduction

The water splitting reaction is one of the most promising candidates to generate hydrogen from renewable energy. The electricity from renewable sources could be used for electrochemical water splitting in electrolyzers or sunlight could directly be used in a photocatalytic reaction. Even the thermal splitting of water by concentrated sunlight is an applied technique.^[3,16] All of the aforementioned methods follow this equation, with the only difference being the kind of energy used to drive the reaction:



The standard potential of this reaction is $E^0 = +1.23 \text{ V}$, which is the theoretical minimal amount of energy required to drive it in the desired direction. On the other hand, when hydrogen is used as a direct energy storage molecule, this would also be the amount of energy released upon combustion with oxygen. De facto, both half reactions (reduction and oxidation) have an overpotential, which needs to be overcome in addition to the thermodynamic potential to drive the reaction. This overpotential occurs due to the catalytic efficiency on the surface of an electrode or catalyst material and is a measure for the activity of a catalyst. For the reduction half reaction, the overpotential is negligible if platinum is used as electrode/catalyst, but also with cheaper and more abundant alternatives the overpotential is quite small in comparison to the oxidation half reaction. Due to its huge overpotential ranging from 0.2 to 0.6 V the oxidation of water is the rate-limiting step of this reaction.^[17] In a similar fashion, the efficiency of photocatalytic water splitting is too low for an industrial application and needs new materials as well. Analogous consideration as above can be made for the photocatalytic water splitting and again the oxidation seems to be the rate-limiting process.^[9,18]

Thus, the search for water oxidation catalysts which are abundant, cheap, and low-cost is the most important factor for promoting the efficiency and applicability of hydrogen generation from water splitting on a world scale. Talking about abundance of a material for the application in the energy sector on world scale implies massive amounts, which might only be available from the most common elements in the earth crust. This is one of the reasons why manganese might be a potential candidate for water oxidation catalysis.

1.2.4 Industrial application of manganese (oxides)

Manganese is widely used in industry in a multitude of processes and the worldwide manganese ore production has an estimated worth of 10-11 billion US\$ per year (estimations done for the year 2013 by Risk & Analyst Ltd^[19]). Furthermore, the total economic value of manganese ore, taking the multiplying effect of the supply chain into account, is around 21-23 billion US\$. These numbers already indicate the importance of manganese for industrial applications.

90% of the annual manganese production is used in the steel process turning iron into durable steel. In this process the manganese improves mechanical properties of the steel, decreases the critical cooling rate during the hardening process of the material, acts as a deoxidizer to prevent the elements from segregating and enhances the machinability due to the formation of soft inclusions with sulfur.^[20] Another big field of application for manganese for roughly 150 years is the battery industry.^[21,22] Manganese was used in some of the very first galvanic batteries: the Leclanché cell by George Leclanché^[23] was patented in 1866 and featured a redox reaction between Zn and MnO₂ in a wet galvanic cell. This research was the foundation for the later developed dry version of this galvanic battery, the zinc-carbon batteries by Carl Gassner^[24] who patented them 19 and 21 years later in Germany and the USA, respectively. But even today, the state-of-the-art lithium ion batteries which are widely used for cell phones, laptops or even electro mobility still utilize manganese.^[25]

Another major application of this element can be found in the production of fertilizers and food additives in the form of manganese sulfates and MnO.^[21] Again this application has production margins of multiple thousand tons per year. Apart from catalysis, pigments are the last prominent application of Mn which will be discussed here. Manganese compounds are known for the multitude of colors they can take on and some found their way into industry in the form of pigments: the purple pigment “manganese violet” with the chemical formula NH₄MnP₂O₇,^[21] the blue pigments “manganese blue” which is BaMnO₄·BaSO₄^[21] and “YInMn Blue” with the chemical formula YIn_{1-x}Mn_xO₃^[26] and finally the black pigment “manganese dioxide” in its pure form MnO₂.^[21] The use of manganese compounds for their coloring properties was

1. Introduction

already discovered by Neanderthals in the prehistorian age.^[27] They utilized the natural Mn-containing mineral umber for cave drawings which can still be viewed and analyzed today.

The next section will depict the role of Mn in industrial oxidation reactions with a focus on oxidation catalysis. One of the most prominent applications of Mn catalysts is the oxidative desulfurization of diesel and jet fuels over a Mn zeolite catalyst.^[28,29] Furthermore, Mn complexes are widely used as oxidants in organic syntheses (e.g. vitamin A synthesis^[30] or aldehydes and ketones^[6]). Multiple bleaching catalysts are patented and applied in detergents including Mn salts and Mn(III)-saltren and also used in the pulp and paper industry.^[28] For instance *catexel* offers commercial manganese catalysts^[31] for hydrogen peroxide activation, bleaching of wood pulp and raw cotton or the oxidative drying of alkyd resin-based coatings. A more specific application in the field of organic synthesis is the Jacobsen epoxidation which is often implemented in the synthesis of pharmaceuticals as the manganese-based catalyst is of low toxicity and cost.^[7,8] But also the pure oxidic phases of Mn in the form of MnO and MnO₂ are often applied in oxidation catalysis for the manufacturing of allyl alcohols, ceramics, paints and colored glass.^[21]

The last world scale application of a MnO_x compound as oxidation catalyst is only of indirect industrial character, but it is nonetheless one of the most important reactions occurring on our planet. Photosynthesis is estimated to yield around 100 billion tons of dry biomass per year and supplies the food for all animals and humans on our planet.^[9] Even our fossil energy supplies (i.e. oil, gas and coal) are derived from millions of years of photosynthesis. The energy from the sun is herein transformed into oxygen and organic molecules, but the biggest obstacle of the whole process is the splitting of water into oxygen and a hydrogen equivalent reduction species.^[9] The catalysis of reduction and oxidation half reactions occur in the Photosystem I and Photosystem II (PSII), respectively. The water oxidizing complex in the PSII is a Mn₄O_xCa cluster which is able to evolve O₂ from splitting H₂O.^[10] It is of major importance to note that the protein shell and the charge transfer mechanism of the whole system is of essential necessity for the process to occur. Therefore, a direct adaptation of the catalyst system presented by nature is very unlikely to work, due to the missing directing and stabilizing environment of the CaMn₄O_x cluster.

Nevertheless, the general potential of manganese oxide was demonstrated by nature and now research needs to find a way to utilize it in a similar fashion to also realize water splitting on a world scale.

1.2.5 Physico-chemical properties of MnO_x

This chapter has been published in Green^[32] and was reformatted and slightly modified here for reasons of clarity and comprehensibility.

There are four stable oxides (MnO , Mn_3O_4 , Mn_2O_3 , MnO_2) and one metastable oxide (Mn_5O_8) available for manganese featuring the oxidation states +II, +III and +IV. The stable manganese oxides, especially MnO_2 , feature a broad range of crystal structures. For Mn_xO_y compounds the origin from the respective minerals is quite important and therefore compounds are often referred to by their underlying minerals name in literature.

The underlying mineral of MnO is the Manganosite, which has the rock salt crystal structure.^[33] This is the only stable configuration of MnO . Mn_3O_4 has only one stable structure as well, which is a tetragonally deformed spinel structure ($\text{Mn}^{\text{II}}\text{Mn}^{\text{III}}_2\text{O}_4$).^[34] The respective mineral is called Hausmannite. Two stable structures are known for manganese(III)oxide: $\alpha\text{-Mn}_2\text{O}_3$ and $\gamma\text{-Mn}_2\text{O}_3$. $\alpha\text{-Mn}_2\text{O}_3$ corresponds to the Bixbyite mineral and has a transition in its structure at almost room temperature. Above 29 °C it has a cubic and below 29 °C an orthorombic crystal structure.^[35] $\gamma\text{-Mn}_2\text{O}_3$ on the other hand has a tetragonal structure which is related to the spinel structure. The α configuration is the thermodynamically stable form and can be obtained from the $\gamma\text{-Mn}_2\text{O}_3$ after 48 h at 500 °C or after 1 year at room temperature.^[35] MnO_2 has the largest variety in crystal structures, therefore only stable and in literature most relevant structures will be discussed here. The most stable structure is $\beta\text{-MnO}_2$ from the mineral Pyrolusite, which features a rutile crystal structure.^[33] As a second form the $\alpha\text{-MnO}_2$ has a tetragonal structure, which is often stabilized by bigger cations (K^+ , Ag^+ , Pb^{2+} , Ba^{2+}), and has no underlying mineral.^[36] Another structure of MnO_2 is solely named after the mineral Ramsdellite (therefore sometimes the annotation R-

1. Introduction

MnO₂ can be found) and has an orthorhombic crystal structure.^[37] The last stable configuration of manganese(IV)oxide is γ -MnO₂ which has no underlying mineral and can be described as an intergrowth of the Ramsdellite and Pyrolusite structures.^[38] The different structures of MnO₂ are of special interest in electrochemistry, due to open channels in all of the structures. Ions can be transported through these channels, making them interesting for ion battery applications.^[38]

All manganese oxides are insoluble in water, but soluble under acidic conditions while forming the respective Mn^{X+}-salts. MnO₂ can also be solved under basic conditions.^[33]

The thermal stability of manganese oxides follows a disproportion reaction into lower valent oxides and oxygen. MnO₂ is stable up to 550 °C after which it decomposes to Mn₂O₃. This compound is stable up to 900 °C where it decomposes to Mn₃O₄, which finally decomposes to MnO at a temperature above 1172 °C.^[33] At moderate temperatures of 250-300 °C on the other hand MnO is oxidized to Mn₂O₃. The metastable Mn₅O₈ can also be obtained by a moderate temperature treatment at 250-550 °C of Mn₃O₄ in air.^[33] Mn₅O₈ is stable in air up to a temperature of 550 °C where it transitions to Mn₂O₃.^[39]

Temperature programmed reduction (TPR) reactions of pure manganese oxides have been conducted in H₂,^[40–45] but also in CH₄.^[40] The crystallinity and the crystal structure of the sample are reported to influence the reduction temperature.^[40,42,45] Mn₃O₄ features a one-step reduction, whereas Mn₂O₃ and MnO₂ feature multi-step reductions, but all yield quantitatively MnO as a reduction product.^[40–45] Generally the reduction of pure Mn_xO_y compounds in H₂ takes place below 500 °C,^[40–45] whereas reduction in CH₄ occurs at higher temperatures of 450 °C-950 °C.^[40] MnO₂ is reported to show two major reduction peaks in H₂ at temperatures of 300-350 °C and 400-500 °C, which are attributed to the reduction of MnO₂ to Mn₃O₄ and afterwards to MnO.^[40,42,45] Similar patterns were also reported for Mn₂O₃ with reduction temperatures around 300 and 400 °C following the same reduction pathway as MnO₂.^[40] Hausmannite reduction is reported to take place at around 450 °C featuring a direct transition to the stable MnO.^[40] Further reduction of MnO could only be observed under addition of carbon or hydrogen at temperatures above 1200 °C.^[43,46]

1. Introduction

For the application of manganese oxides in photocatalysis the band gap energy is of special interest. The number of values reported for the band gap energies of the different manganese oxides are rather low and only in recent years due to the rising interest in nanoparticles and thin films the number of reported band gap energies is rising. Reports on the application of UV-vis and optical absorption spectroscopy methods, which are commonly used for the determination of optical band gap energies, can mostly be found for nanosized materials, and are a rarity for bulk materials and minerals of the manganese oxides. Values reported for nanosized oxides vary strongly, which might be due to the quantum size effect influencing the band gap of these materials. MnO nanoparticles in composite materials are reported to have a band gap of 2.0 eV.^[47] For nanosized Mn₃O₄ a large number of values for the band gap energy over an unusually large range are reported ranging from 2.07,^[48] 2.30,^[49] 2.50,^[50] 2.54,^[45] all the way to 3.28-3.75^[51] and 3.70 eV.^[47] The obtained band gap energy depends on the preparation method. In a similar manner pure Mn₂O₃ nanoparticles have reported band gap energies of 1.20,^[52] 1.91,^[53] 2.01,^[53] 2.09,^[53] 2.99^[54] and 3.69 eV,^[51] which are again dependent on the preparation method of the particles. A mesoporous structure containing Mn₃O₄ and Mn₂O₃ was found to have band gap energies of 2.46 and 3.18 eV after calcination and uncalcined, respectively.^[55] Studies on MnO₂ nanosheets revealed a band gap energy of 2.23 eV.^[56] One report on successful UV-vis studies of Na Birnessite-type MnO₂ mineral revealed a band gap of 2.1 eV.^[57] To gain insight into the band structure of bulk materials an approach with x-ray spectroscopy can sometimes be found in literature. The band gap energy can be estimated as O(2p) → Mn(3d) ligand-to-metal charge-transfer transition.^[58] 1.0, 1.2 and 1.8 eV were found to be the band gap energies of Pyrolusite, Cryptomelane and Birnessite, respectively.^[58] Similar studies were undertaken for MnO utilizing bremsstrahlung isochromat spectroscopy to reveal a band gap energy of 3.9 ± 0.4 eV.^[59] Due to the difficulties in the experimental determination of these energies, also theoretical calculations of the band structure of pure MnO were conducted and resulted in different values of 2.95,^[60] 2.8,^[61] 3.5^[59] and 3.92 eV.^[61] Calculations and theoretical modeling of the band gaps of manganese oxides are challenging and should not be judged due to missing reliable experimental data.^[62]

1. Introduction

The last property of manganese bulk oxides to be discussed here is the surface charging. It is of major importance for catalytic processes, due to its influence on the adsorption properties of the material, and for the probability of charge transport to the surface. Therefore, closer attention will be paid to the point of zero charge (PZC), which describes the pH value at which no surface charge is present on the material, and the isoelectric point (IEP), which describes a pH value at which a molecule on the surface of the material has no net electrical charge. The PZC of Hausmannite (Mn_3O_4) was determined in NaClO_4 solution, but was outside of the measurable region of the experiment, therefore the value is > 10 if any exists.^[63] Mn_2O_3 was measured in LiCl solution and the PZC was found to be 6.5.^[64] The different crystal structures of MnO_2 have separately been measured and PZCs of 6.5,^[65] 7.3-7.7,^[66] 5.3-5.9^[67,68] and < 2.5 (if any)^[66] were found for α -, β -, γ - and R- MnO_2 respectively. Additionally, points of zero charge for manganese oxide minerals can be found in literature: Acidic Birnessite,^[69] Cryptomelane,^[69] alkaline Birnessite,^[69] Todorokite^[69] and Manganite^[63] are reported to have PZC values of 1.78, 2.15, 3.35, 3.50 and 7.4 respectively. *Marek Kosmulski*^[70] made a huge effort of compiling PZC and IEP values and averaged PZC values for MnO_2 samples. An average over 13 commercial MnO_2 samples gave a PZC of 5.3 ± 1.16 , 21 synthetic MnO_2 samples averaged to a PZC of 4.9 ± 1.28 and 4 natural MnO_2 samples gave an average PZC of 5.5 ± 1.01 . *Kosmulski* also addressed the reason for the largely differing PZC values of manganese oxides. In his comparison he found that the cation of the electrolyte (which is generally viewed as inert) has a huge influence on the measured PZC of up to 2 pH units.^[71] Further, no clear trend for the influence of the electrolyte and the crystalline modification could be found for MnO_x materials, though the oxidation state of the manganese is often discussed to influence the PZC.^[70]

Kosmulski also compiled the isoelectric points of different manganese oxides and minerals:^[70] Synthetic MnO was found to have an IEP of 5.5, synthetic Hausmannite of 5.7 and Bixbyite of 4.7. Synthetic combinations of those compounds exhibited IEPs of 5 for the mixture of $\text{MnO}_2 + \text{MnO}$ and a value of 6 for the combined oxides $\text{Mn}_2\text{O}_3 + \text{Mn}_3\text{O}_4$. The minerals Groutite (MnOOH) and two different species Manganite (MnOOH) were found to have isoelectric points of 9.6, 6.3 and 8.5 respectively.

1.3 Scientific objective of this work

Great efforts have been made to gain a better general understanding of the manifold Mn oxide structures and phases. Nevertheless, there are still ongoing discussions and wide ranges of sometimes diverging datasets. In this context two questions need to be addressed, the first one of which is concerned with how to investigate and analyze the phase of a MnO_x sample with an unknown composition and to identify the oxidation states of the individual phases.

At first glance this problem might seem trivial, since a multitude of methods are available which give the desired information. Unfortunately, most are spectroscopic methods and might be of inadequate accuracy, because MnO_x is well known to easily transform under high-energy radiation.^[72–75] Furthermore, another aim is finding a characterization method which also works on amorphous samples not analyzable by X-ray powder diffraction (PXRD), since materials applied in catalysis are often of flexible structure and not 100% crystalline. Therefore, a chemical method is needed which is not subject to irradiation damage. The method of choice here is temperature programmed oxidation or reduction (TPO/TPR). In addition, low energy spectroscopy such as Raman will be used to gain phase information on MnO_x to complement the other techniques. By choosing the right parameters for the techniques described above a method should be developed which is applicable to all bulk MnO_x samples.

The second aim of this work is elucidating the intrinsic catalytic activity of the thermodynamically stable manganese oxides (i.e. MnO Manganosite, Mn_3O_4 Hausmannite, $\alpha\text{-Mn}_2\text{O}_3$ Bixbyite and $\beta\text{-MnO}_2$ Pyrolusite) in oxidation reactions. To further this goal, the selected samples will be applied in the oxidation of CO and the partial oxidation of 2-propanol including a temperature ramp for activity sequences and the determination of apparent activation energies and reaction orders. These studies aim to deepen the understanding of bulk MnO_x in oxidation catalysis and give insight into its redox behavior. It is the aim of the study to answer the question whether the redox couple Mn(II)/Mn(III) or the redox couple Mn(III)/Mn(IV) is responsible for the activity in oxidation catalysis.

2. Methods and techniques

2.1 Vibrational spectroscopy

Molecules possess distinct rotational and vibrational energy levels. The transition between such levels needs energy in the order of a few meV and can thus be measured by infrared (IR) and Raman spectroscopy to identify the structure and binding situation in materials.

The model of the harmonic oscillator can be thought of as a first approximation of the potential energy for a diatomic molecule:^[76]

$$V(r) = \frac{1}{2}k(r - r_{eq})^2 \quad (1)$$

Herein $V(r)$ is the potential energy of the molecule, k is the force constant of the vibrating bond, r is the distance between the vibrating atoms and r_{eq} is the equilibrium distance of the two atoms. The energy levels for this model are equidistant and can be described as

$$E_n = (n + \frac{1}{2})h\nu \quad (2)$$

where E_n is the energy of the individual vibrational level, n is an integer, h is Planck's constant and ν is the frequency of the vibration. The frequency can be calculated from the force constant k and the reduced mass μ of the molecule:

$$\nu = \frac{1}{2\pi} \sqrt{\frac{k}{\mu}} \quad (3)$$

This model includes the fact that the frequency of the vibration increases with higher bond strength and decreasing mass of the vibrating atoms.

Exclusively transitions of $\Delta n = \pm 1$ are allowed for the harmonic model, which denies the possibility of vibrational overtones. An overtone is the absorption of light at integral multiples of the fundamental frequency. Furthermore, the equidistance of energy levels is only a good approximation for the first few vibrational levels. The Morse potential is a more realistic approximation. It allows overtones and the dissociation of the molecule. The potential is described by the equation

2. Methods and techniques

$$V(r) = D(1 - e^{-a(r-r_{eq})})^2 \quad (4)$$

where D is the dissociation energy of the vibrating bond and a is a parameter controlling the steepness of the potential well. The potential energy curves of both models can be seen in Figure 5.

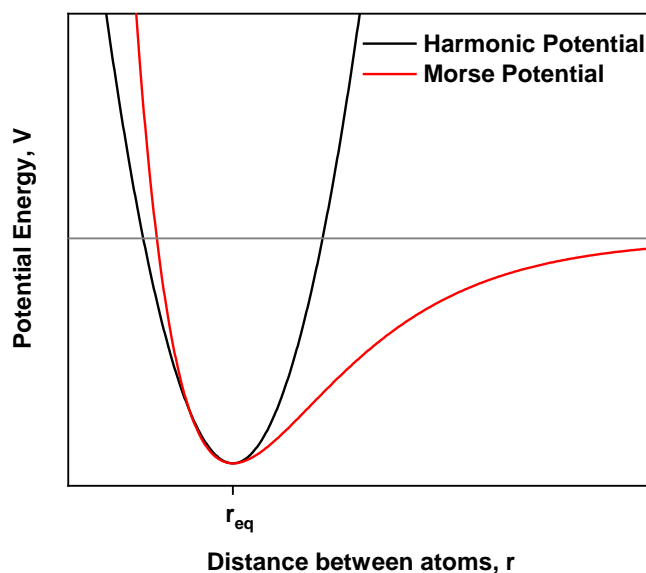


Figure 5: Potential energy V for a diatomic molecule over the atom distance r calculated for the models of the harmonic oscillator and the Morse potential.

The number of vibrations a molecule possesses is an important factor for vibrational spectroscopy. The number of degrees of freedom a molecule with N atoms possesses is equal to $3N$.^[76] Thereof, three are translational and for non-linear molecules another three are rotational degrees of freedom. For a linear molecule the potential energy does not change when rotated around the main axis, thus only two rotational degrees of freedom can be distinguished. Hence, $3N - 6$ degrees of freedom ($3N - 5$ for linear molecules) can be attributed to the fundamental vibrations of the molecule.

Four types of vibrations are distinguished in vibrational spectroscopy: Stretching vibrations (symbol ν), which change the length of a bond, bending vibrations in one plane (symbol δ), which change the bond angle without changing the bond length, bending vibrations out of the plane (symbol γ), which are defined by one atom

2. Methods and techniques

oscillating through a plane spanned by at least three other atoms and torsion vibrations (symbol τ), which change the angle between two planes through atoms.^[76] In general, the frequencies follow the order $\nu > \delta > \gamma > \tau$ and are divided into symmetric and asymmetric vibrations. Figure 6 shows the most common fundamental vibrations.

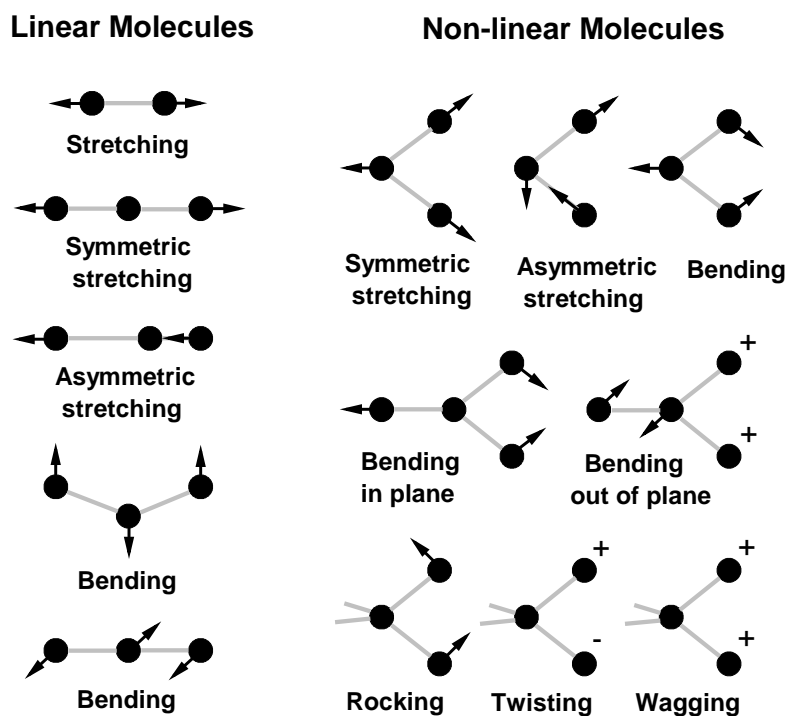


Figure 6: Commonly observed fundamental vibrations of a molecule. adapted from [77]

Even though the vibrational transitions of a molecule are in the region of IR and Raman spectroscopy the corresponding vibrational bands are not necessarily visible. The absorption of an infrared photon can only be observed in IR spectroscopy if the dipole moment of the molecule changes during the vibration. On the other hand, vibrations need to feature a change of polarizability to be detectable by Raman spectroscopy, which is based on the inelastic scattering of photons. The two methods are mostly complementary and vibrations that are not detectable in IR spectroscopy can often be seen in Raman spectra and vice versa.

The different absorption behavior in these two techniques is of fundamental character. In infrared spectroscopy the molecules absorb the emitted photons directly which leads to an excitation of a vibrational state in the molecule making this a one-

2. Methods and techniques

photon event. On the other hand, Raman spectroscopy features a scattering of the emitted photons by the molecule, which makes this process a two-photon event. The scattering events are differentiated into elastic scattering (Rayleigh scattering) and inelastic scattering (Raman scattering). The different absorption and scattering events for Raman and IR spectroscopy are illustrated in Figure 7.

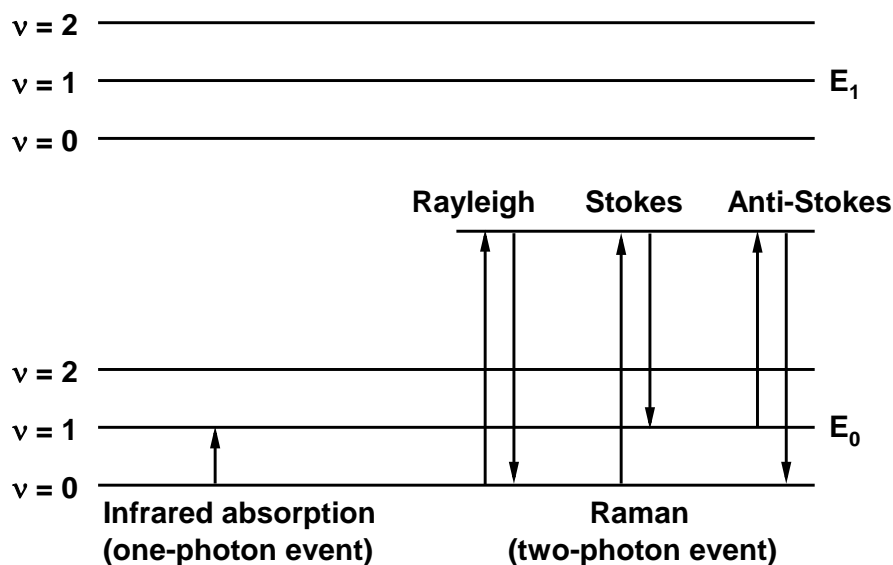


Figure 7: Illustration of the absorption and scattering events in IR and Raman spectroscopy. adapted from [76]

The processes depicted in Figure 7 for the Raman spectroscopy assume a molecule in the electronic and vibrational ground state. This molecule is excited by a photon and raised to a “virtual state” which is not a true energy state of the molecule but induced by the polarization of the molecule. Afterwards, it can either drop back to the ground state and emit the same amount of energy it absorbed (elastic Rayleigh scattering) or it can drop to an excited vibrational state emitting a photon of smaller energy (inelastic Raman scattering). This phenomenon is called a Stokes shift and happens roughly every 10^6 photons at moderate temperatures.^[77] An analogous process is possible when molecules are excited from vibrational states above the ground state. If it relaxes to the vibrational ground state after the scattering process, the resulting photon will be of higher energy than the emitted photons. This process is called an Anti-Stokes shift and is lower in intensity than the Stokes shift at

2. Methods and techniques

moderate temperatures, due to the lower population of excited levels. Figure 8 shows a schematic Raman spectrum including Stokes, Anti-Stokes and Rayleigh lines.

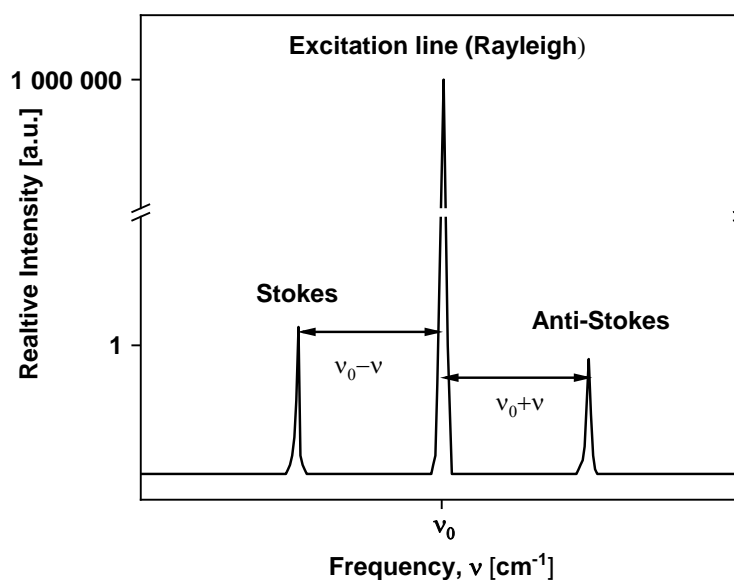


Figure 8: Schematic plot of a Raman spectrum depicting Stokes, Anti-Stokes and Rayleigh lines and indicating relative intensities. adapted from [76]

Relaxation of a molecule can lead to the observation of fluorescence. This effect can have an intensity up to four orders of magnitude higher than regular Raman bands and thus completely overlap the signals. Fluorescence effects might originate from the sample itself, but it is also possible that unwanted impurities in the sample are responsible for the fluorescence and make the measurement impossible.^[77]

Since the irradiation energy can vary in Raman spectroscopy, because it is not tailored to the absorption of a molecule as it is in IR spectroscopy, a broad range of possible laser wavelengths can be used. Therefore, the sample can be irradiated with wavelengths from the IR to the UV region. The use of different lasers sets varying requirements for the set-up but also features a multitude of benefits. UV Raman can be used to prevent the influence of fluorescence, because the spectrum is acquired in the UV region, which is a different spectral window than the fluorescence region.^[77] Furthermore, the temperature range of the measurement is nearly unlimited, because UV light is emitted only at extremely high temperatures from the black body radiation. On the downside, the spectral resolution of UV Raman

2. Methods and techniques

is quite low, with a good spatial resolution.^[77] The commonly used CCD (charge-coupled device) detectors cannot be used for this measuring technique, since they are not sensitive towards UV photons. Thus, a special coating which converts UV photons into visible light photons is required for the set-up and all windows must be made of quartz to ensure the absence of photon absorption by the set-up.^[77] Another problem in UV Raman is sample stability. UV light has a high energy content and irradiation damage of the sample is more of an issue than for lower energy radiation. Another type of Raman spectroscopy, which is the most commonly applied technique, utilizes radiation in the visible light region. For this method there are no special set-up requirements and black body radiation starts to interfere only at temperatures around 800-900 °C. The degradation of the sample is generally less problematic than with the highly energetic UV light.

Near infrared Raman spectroscopy is commonly measured at a wavelength of around 780 nm and is an intermediate between visible light Raman and Fourier transformed (FT) Raman in the IR region. This type of measurement is still able to utilize the standard set-up without any modifications, but might be able to prevent beam damage to the sample, while yielding good Raman intensities at minimized fluorescence.^[77]

FT-Raman is the fastest Raman technique and features the highest spectral resolution at the lowest spatial resolution. This method has the lowest signal intensity but is ideal for fast sample scanning. To successfully apply this technique, the set-up needs to be adjusted for IR radiation and the temperature of the sample cannot be above 150 °C, due to the strong black body radiation. Furthermore, due to the strong absorption of water in the IR region it is a hindrance for these measurements and samples often need to be dried before measurement.

2.2 Catalytical CO and 2-propanol oxidation

2.2.1 Introduction to catalysis

Chemical reactions are limited by thermodynamics and kinetics. The thermodynamics determine whether a given reaction can occur or not and there is no way to drive a thermal reaction if the thermodynamics are not feasible. The kinetics of a reaction on the other hand do not have any influence on the equilibrium state and govern solely the speed of the process. Several substances are stable in our atmosphere, which contains O_2 having a very high oxidation potential, although thermodynamics would predict a high energy gain by combustion and thus a reaction. One such example is methane which is stable under ambient conditions although it is known for the high heat of combustion which can be gained from it. Thermodynamics predict a reaction equilibrium where methane is fully converted to CO_2 and H_2O . The stability of this molecule is governed by kinetics, since the combustion under ambient conditions is kinetically hindered and thus so slow that it effectively does not occur. This phenomenon is in no way an equilibrium state, since thermodynamics emphasize a total combustion. The factor which is preventing a reaction in this case is a high kinetic barrier which needs to be overcome for the reaction to occur. The same principles apply to industrial applications where chemical reactions are often driven under conditions of continuous flow and thus the rate of reaction influences the degree of conversion X of the educts. It is of importance to point out again that obtaining higher conversions does not stem from a difference in the equilibrium state of the reaction, but solely from higher reaction rates making this a kinetical phenomenon.

Kinetics are governed by the changing total energies of one or more molecules which transition in their given geometry. Thus, if two molecules are to react to reach a thermodynamically more stable form, in most cases they must first transition through a less stable state by adjusting their geometry. This state is called the transition state and the energetic difference between the initial state and the transition state is called a kinetic barrier or, for the highest barrier in a reaction sequence, the activation energy of the reaction (this process is visualized in Figure 9). It is the minimal energy

2. Methods and techniques

amount a given molecule or molecule conformation has to procure to overcome the barrier or be “activated”. This activation energy E_A is dependent on the geometry of the transition state and can be lowered by offering the molecule a reaction site, where it can adjust to the new conformation in a less energy consuming way. This is the working principle of a catalyst, which offers an alternative transformation route to form the same products from given reactants but features lower kinetic barriers overall. A possible scenario which differentiates between the catalyzed and uncatalyzed routes is outlined in Figure 9.

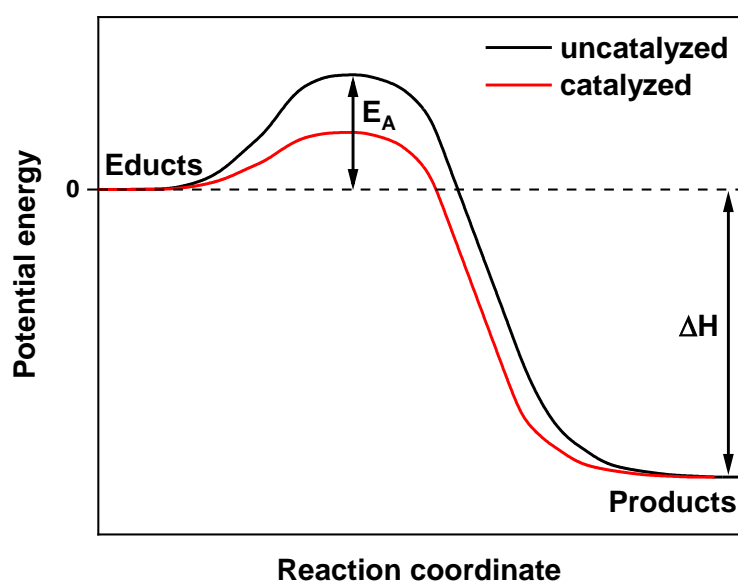


Figure 9: Potential energy for an uncatalyzed (black) and catalyzed (red) chemical reaction leading from reactants to products. Additionally, the activation energy E_A and the reaction enthalpy ΔH are illustrated.^{adapted from}

[78]

Since a catalyst offers lower kinetic barriers for a chemical reaction pathway, it accelerates the rate of reaction and therefore increases the conversion under continuous flow conditions. Again, no change of the reaction equilibrium is induced by the introduction of a catalyst, since only the reaction kinetics have been altered. Reactions which are severely limited by equilibrium conditions (e.g. ammonia synthesis in the Haber-Bosch process) are still limited by the reaction conditions which determine equilibrium conversion and even the best catalyst will only reach this degree of conversion no matter how fast the reaction rate may be. Nevertheless, a catalyst may have an additional purpose apart from increasing the rate of

2. Methods and techniques

reaction. In cases with multiple possible reaction products it may have a directing influence on the reaction network. The degree of conversion of reactants towards a specific product is called the selectivity S of this process. If a clever designed catalyst decreases only the kinetic barriers towards the desired product and does not influence the barriers towards the undesired side product(s) an increase in selectivity towards the desired product is the consequence. Thus, the second task of a catalyst in a chemical reaction pathway is influencing the selectivities towards certain products.

Since the activation energy of a given reaction is a direct indicator of the performance of a catalyst a method for quantification is needed. The Arrhenius equation given by

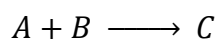
$$k = A e^{-\frac{E_A}{RT}} \quad (5)$$

where k is the rate constant, A is the pre-exponential factor, R is the universal gas constant and T is the temperature can be used to calculate the activation energy E_A . When equation (5) is linearized by the natural logarithm the form

$$\ln(k) = \ln(A) - \frac{E_A}{RT} \quad (6)$$

is obtained. For a given sequence of reactions, performed at differing temperatures, the reaction rate constants can be used to determine the activation energy. To this end $\frac{1}{T}$ has to be plotted against $\ln(k)$ and E_A can be determined from the slope of the linear regression.

Another interesting parameter that can be influenced by a catalyst is the reaction order of the reactants. If we consider a reaction of the form:



the rate of reaction r is given by the rate law:

$$r = \frac{d[C]}{dt} = k [A]^a [B]^b \quad (7)$$

where $[A]$, $[B]$ and $[C]$ are the concentrations of the individual species and a and b are the individual reaction orders of reactants A and B, respectively. The reaction

2. Methods and techniques

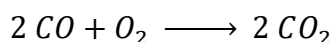
orders a and b are integral values over the whole reaction network and can thus take any form which often means non-integer values. Only if the rate of reaction is determined for an elementary step reaction orders will take whole integer values. Since a catalyst influences the reaction pathway of a chemical reaction it often also influences the reaction order. This can help to identify the mechanism of a reaction and reveal the influence of the different reactants. The most common method to experimentally determine reaction orders of a given catalyzed reaction under steady state conditions in continuous flow experiments considers equation (7) in a rearranged form:

$$\log(r) = \log(k) + a \log([A]) + b \log([B]) \quad (8)$$

Thus, if only the concentration of one reactant is varied at a time and the concentration of the other reactants is high enough to be considered constant, a series of experiments can be conducted to receive a $\log(r)$ vs $\log([A])$ plot. Herein, the reaction order a can be obtained from the slope of the plot. This way the influence of each reactant can be investigated individually until all reaction orders have been determined.

2.2.2 MnO_x in CO and 2-propanol oxidation

CO oxidation is one of the most basic oxidation probe reactions in catalysis and features the total combustion of CO to CO₂ as follows:

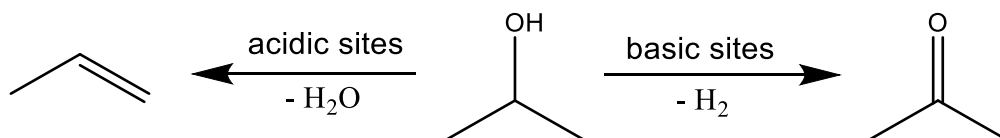


This reaction is commonly used to investigate the general oxidation behavior of a catalyst and gain insight into the oxygen activation of the material.

The 2-propanol oxidation on the other hand features multiple reaction pathways and selectivity plays a crucial role in this process. The 2-propanol can be dehydrated on acidic sites to yield propylene or dehydrogenated on basic sites to yield acetone. It should be noted, that propylene formation has been observed on strongly basic sites as well, but the mechanism of this transition has not been clarified yet.^[79] Another

2. Methods and techniques

possible reaction route is the direct oxidation of the reactant by oxygen. In this case acetone may be formed by direct oxidation or from oxidation of propylene previously formed in an acid-base reaction.

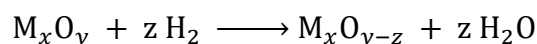


Focusing on manganese oxide no agreement on the reactivity trends can be found. Most studies focus on one specific oxide and compare different phases of the same oxidation state.^[80–84] MnO₂ is the most commonly investigated sample found in literature and a lot of effort has been made to find the most active phase and preparation method for this material. However, only few comparative studies in CO and alcohol oxidation for different oxidation states of MnO_x can be found which allow a comparison of different species due to the same measurement conditions.^[85–87] Surprisingly all of these comparative studies indicate a higher activity of Mn₂O₃ than MnO₂ for the oxidation of CO and alcohols. In the field of water oxidation on the other hand, a few more comparative studies can be found which might give insights into the redox activity of these materials, although the actual thermal catalysis constitutes of a lot more aspects than only the redox behavior. *Stoerzinger et al.* made quite an effort to normalize and compare electrochemical activities of different systems.^[88] Again the presence of Mn(III) seems crucial for a high activity in the oxidation of water. The highest activities were shown for systems which contained both Mn(III) and Mn(IV) species, but pure Mn(IV) compounds featured lower activities.^[88] Thus, a direct comparison of the stable oxide phases to answer the question which redox couple (Mn(II)/Mn(III) or Mn(III)/Mn(IV)) drives manganese oxide catalysis has still not been accomplished.

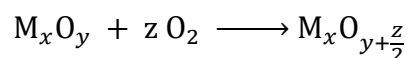
2.3 Temperature programmed oxidation/reduction

Temperature programmed reactions have been applied in catalysis for the characterization of material for roughly 40 years now. The first report on TPR in literature was made by *Robertson et al.* in 1975.^[89] Thereafter, the temperature programmed techniques, especially the TPR method, received much attention and rapidly grew to a well-established characterization method. Temperature programmed reactions are by no means limited to metals and oxides and can be used for the analysis of a variety of compounds. Due to the special interest in metal oxides in catalysis and the scope of this work, this chapter will deal exclusively with the oxidation and reduction of oxides and pure metals.

TPR can be conducted with a multitude of reaction gases although hydrogen is the most commonly used reducing agent. The general reaction scheme in a temperature programmed reduction of metal oxides with hydrogen has the form:



The oxide is reduced with hydrogen to yield either a lower valent oxide ($z < y$) or the metal ($z = y$) and water. Similar considerations can be done for the TPO which does not commonly feature as many different oxidation reagents. The temperature programmed oxidation is mostly performed with oxygen and the reaction has the following form:



In this case no byproduct is formed by the transition of a metal ($y = 0$) or lower valent oxide ($y > 0$) to an oxide with higher oxidation state.

The next section will elucidate the thermodynamic and kinetic aspects of temperature programmed reactions. Since TPR is the more commonly used method and the initial development of the technique was aimed at the reduction reaction the explanations and calculations will be done for this type of reaction. Nevertheless, the same considerations can be applied analogously to the TPO.

2. Methods and techniques

The thermodynamics of the reduction are governed by the equation^[90]

$$\Delta G = \Delta G_0 + RT \log\left(\frac{P_{H_2O}}{P_{H_2}}\right) \quad (9)$$

where ΔG is the free energy, ΔG_0 is the standard free energy, R is the universal gas constant, T is the temperature of the system and P is the partial pressure of the reaction gases. The reduction of the investigated sample will only take place if $\Delta G < 0$ which means that oxides with a negative standard free energy will readily react, but also oxides featuring a positive standard free energy can be driven to reaction if the second term of equation (9) compensates for the positive ΔG_0 . This is not uncommon, since TPR is performed under flow conditions which continuously remove the water from the system and lower P_{H_2O} significantly. Thus, the logarithmic term will be strongly negative and even the oxides of vanadium, tin and chromium with ΔG_0 values of 45, 50 and 100 kJ/mol, respectively, have been reported to react under TPR conditions.^[90]

For the kinetic considerations two different models are commonly used to describe the growth process of the metallic phase on the oxide particle: The contracting sphere model and the nucleation model.^[90,91]

In the contracting sphere model, the reduction takes place on the surface of the particle and the reaction front continuously closes in on the core. Thus, the reaction rate is limited by available surface area and decreases over time due to the lower surface area of the shrinking particle. Figure 10 shows the reaction sequence taking place in the contracting sphere model and depicts the radii r_0 and r_1 which are the initial and current oxide particle radius, respectively. To calculate a degree of reduction α , first the fractional thickness f of the reduced metal layer has to be defined as:

$$f = \frac{r_0 - r_1}{r_0} \quad (10)$$

The degree of reduction α can thus be determined by the ratio of the mass m and the initial mass m_0 which in turn is dependent on the volume and can be expressed as:

$$\alpha = \frac{m}{m_0} = 1 - (1 - f)^3 \quad (11)$$

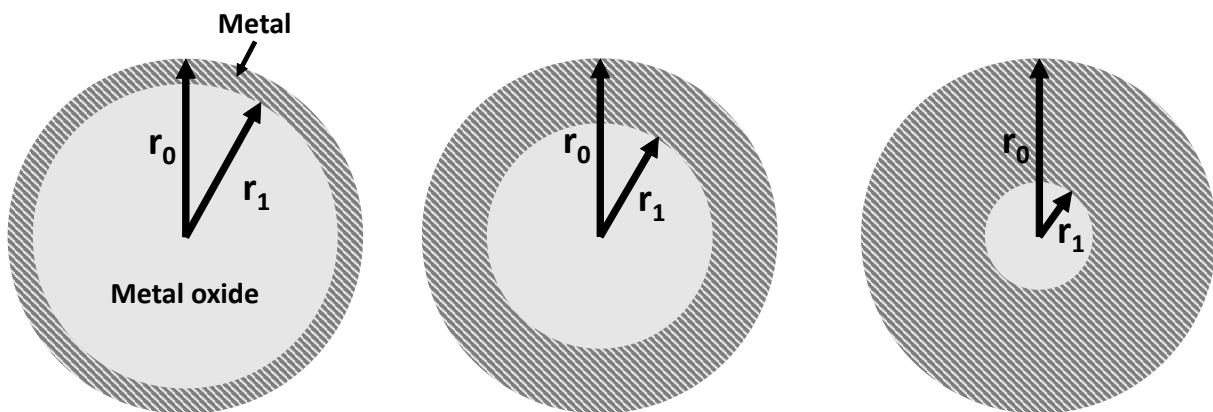


Figure 10: Sequence of steps in the reduction (left to right) of a metal oxide to metal according to the contracting sphere model. The inner grey space represents the initial oxide phase and the shade area represents the growing metal phase during the reduction process. r_0 is the initial radius of the metal oxide and r_1 is the current radius of the oxide particle.

By applying equation (11), the progression of α over time can be calculated for a constant rate of reduction (constant decrease of r_1 over time) the results of which can be seen in Figure 11.

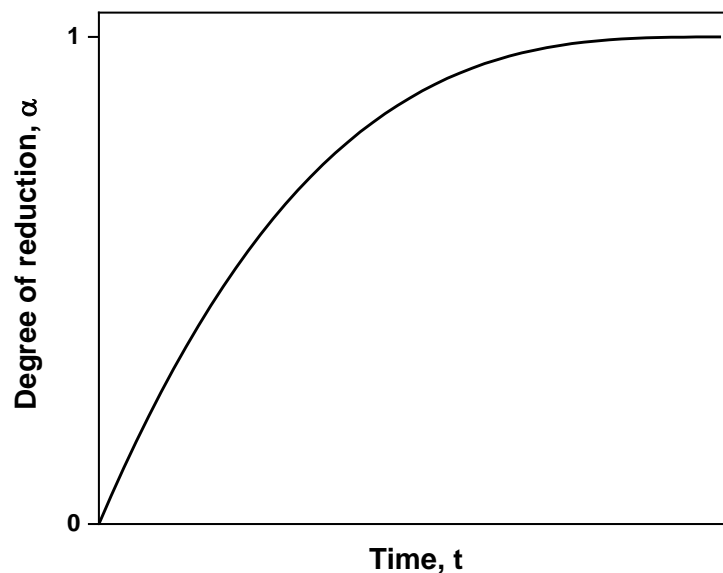


Figure 11: Degree of reduction α over time for the contracting sphere model.

The nucleation model on the other hand assumes an induction period of the time t_1 in which the reduction starts to take place and small nuclei of solid metal are formed on the surface of the metal oxide particle. Thereafter, these nuclei grow at their surface

2. Methods and techniques

which is steadily increasing. The rate of reduction for this model increases over time, until it reaches a state in which the different nuclei touch each other. At this point, a decrease of reduction rate can be seen similar to the contracting sphere mechanism. A sequence of steps in the reduction for the nucleation mechanism is depicted in Figure 12.

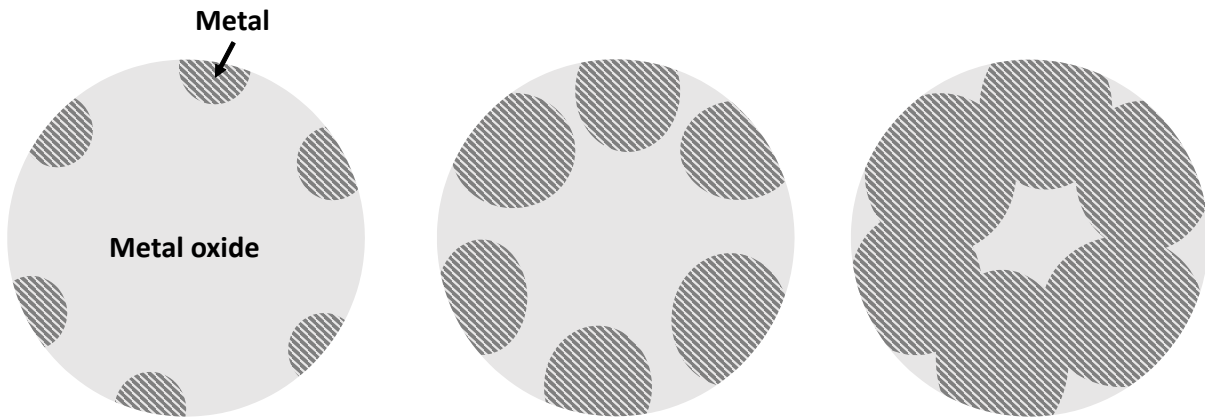


Figure 12: Sequence of steps in the reduction (left to right) of a metal oxide to metal according to the nucleation model. The inner grey space represents the initial oxide phase and the shade area represents the growing metal phase during the reduction process.

For the mathematical description of the degree of reduction α over time t for the nucleation model three different sections have to be distinguished. The first phase is the induction period up to the time t_1 where no reduction takes place aside from the nucleation (leaving $\alpha \approx 0$). The second phase is characterized by the intermediate growth of the nuclei, leading to an increase in the reduction rate. In the last section the nuclei overlap, and the rate of reduction thus decreases analogous to the previously discussed contracting sphere model.

The second section can be described mathematically,^[90] if we consider first the proportionality of the volume of a nucleus V :

$$V \propto (t - t_1)^p \quad (12)$$

Herein, t is the time, t_1 the length of the induction period and p is the dimension of the growing nucleus. Further, the formation rate of nuclei has also to be considered:

2. Methods and techniques

$$\frac{dG}{dt} \propto (t - t_1)^q \quad (13)$$

where G is the number of nuclei formed and q is a number related to the nucleation mechanism (-1 for instantaneous nucleation, 0 for constant rate nucleation and an integer n for power law nucleation). Taking these considerations into account it is possible to find an expression for the total volume of reduced species $V(t)$ at time t .

$$V(t) = \int_{t_1}^t \frac{dG}{dt} V dt = C(t - t_1)^{q+p+1} \quad (14)$$

where C is a constant accounting for the proportionality factors of equations (12) and (13). Thus, the degree of reduction can be calculated from:

$$\alpha = \frac{V(t)}{V_{final}} = \frac{C}{V_{final}} (t - t_1)^{q+p+1} \quad (15)$$

Now equation (15) is giving a mathematical term to calculate α over time for the nuclei growth period. The complete behavior of the degree of reduction with time is illustrated in Figure 13 and can be described as a S-shaped curve.

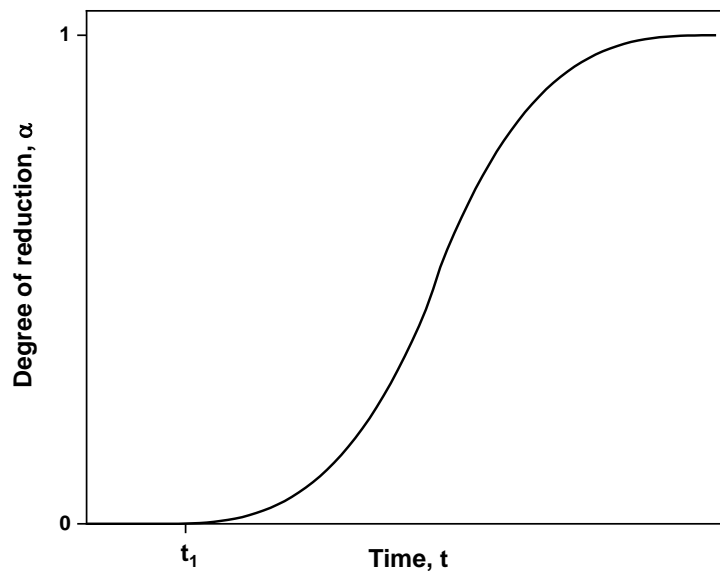


Figure 13: Degree of reduction α over time for the nucleation model.

Another important aspect of TPR and TPO measurements is the choice of parameters. Already in the early years of TPR research, a lot of groups have studied

2. Methods and techniques

the influence of the measurement parameters on the curve shape and peak resolution.^[90,92–94]

The first to systematically analyze the choice of parameters were *Monti and Baiker*^[94] who investigated the amount of reducible species S , the initial hydrogen concentration c_0 in the stream and the total volume flow \dot{V} in a common range of heating rates of $\beta = 6 - 18 \text{ K/min}$.

First, a general description of the kinetics of the process is given by:^[94]

$$\frac{dS}{dt} = -kS^q \bar{c}^m \quad (16)$$

where k is the rate constant of the reduction, \bar{c} is the mean hydrogen concentration between reactor in- and outlet and q and m are reaction orders. Furthermore, the hydrogen mass balance is given by:

$$\dot{V}c_0 = \dot{V}c + kS^q \bar{c}^m \quad (17)$$

where c is the current concentration of hydrogen at the reactor outlet. Thus, the initial amount of hydrogen must be equal to the resulting hydrogen amount plus the amount consumed by reaction.

Additionally, a constant heating rate β and the Arrhenius law have to be taken into account:

$$\frac{dT}{dt} = \beta \quad (18)$$

$$k = k_0 e^{-\frac{E_A}{RT}} \quad (19)$$

A correlation between the reaction parameters \dot{V} , c_0 , β and S and the kinetic parameters k_0 and E_A can be obtained by combining equations (16)-(19):^[94]

$$\frac{dS}{dT} = -\frac{2c_0\dot{V}}{\beta} \left(\frac{1}{1 + \frac{2\dot{V}}{Sk_0 e^{-\frac{E_A}{RT}}}} \right) \quad (20)$$

Maxima in the rate of reduction can be determined by calculating:

2. Methods and techniques

$$\frac{d}{dT} \left(\frac{dS}{dT} \right) = 0 \quad (21)$$

If first order kinetics are assumed regarding the hydrogen and the solid ($q = m = 1$) it is possible to obtain an expression for the determination of the kinetic parameters by combining equations (16) and (21):^[94]

$$\frac{E_A}{RT_M^2} = \frac{k_0}{\beta} \bar{c}_M e^{-\frac{E_A}{RT}} \quad (22)$$

The index M indicates T and \bar{c} values at the peak maximum as was determined by equation (21). For an easier application equation (22) is commonly written as:

$$\ln \frac{T_M^2 \bar{c}_M}{\beta} = \frac{E_A}{RT_M} + \ln \frac{E_A}{Rk_0} \quad (23)$$

This mathematical form opens the opportunity to measure a series of TPRs at varying heating rates β and plot the results as $\ln \frac{T_M^2}{\beta}$ vs $\frac{1}{T_M}$. For such a plot, E_A can be calculated from the slope and k_0 from the intercept with the y-axis (see Figure 14).

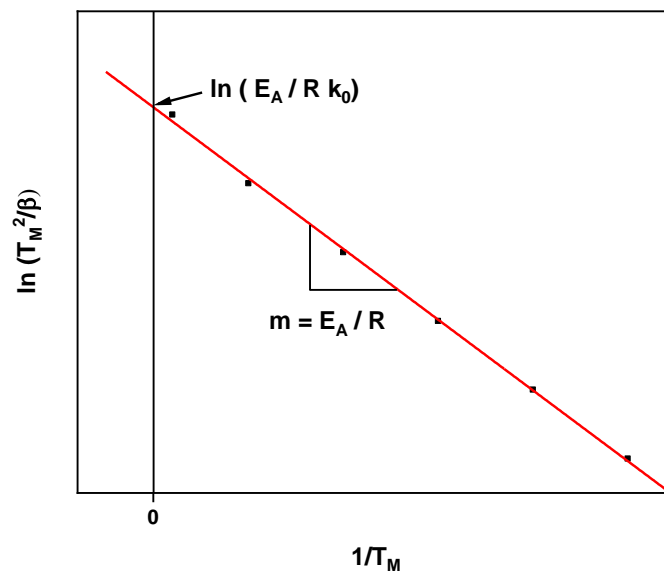


Figure 14: Exemplary $\ln(T_M^2/\beta)$ vs $1/T_M$ plot for the determination of E_A from the slope m and k_0 from the intercept with the y-axis.

Furthermore, *Monti and Baiker* showed that a good resolution and sharp peak shapes are needed to obtain kinetic parameters with low errors. Therefore, they

2. Methods and techniques

evaluated the influence of the chosen measurement parameters in a fixed interval of heating rates (6-18 K/min). They concluded that the hydrogen consumption at the TPR peak maximum should not exceed 66% of the initial hydrogen amount in the feed gas and not fall short of 10%. To this end, they introduced the parameter K .^[94]

$$K = \frac{S_0}{\dot{V}c_0} \quad (24)$$

For the given limitations K should be kept in the interval $55 \text{ s} < K < 140 \text{ s}$ to obtain best results. However, for this study nickel oxide was used which features an one-step reduction and thus no peak differentiation had to be taken into account.^[94] Furthermore, the limitations in β had been chosen rather arbitrary and the present model did not consider higher or lower heating rates.

At this point *Malet and Caballero* reevaluated the criteria of *Monti and Baiker* to conclude that the limitations of the maximal hydrogen consumption were well chosen (consumption $\leq 0.66 c_0$).^[93] But contrarily to the previous study, *Malet et al.* found two parameters that determined the peak resolution and also the peak distinction of multiple reduction events (this study was conducted on the reduction of CuO which features a multistep reduction). The first parameter P which was found to be critical to the TPR peak shapes is very similar to the parameter K proposed by *Monti et al.*:^[93]

$$P = \beta K = \frac{\beta S_0}{\dot{V}c_0} \quad (25)$$

The inclusion of β into the parameter P leads to a removal of the fixed interval of heating rates which was considered beforehand and gives P the dimension of temperature [K]. The second important parameter was $\frac{\beta}{c_0}$ which had to be considered individually. Looking at these two parameters, *Malet and Caballero* computed a multitude of TPR spectra and confirmed the calculations with experiments. They concluded that P and $\frac{\beta}{c_0}$ should be kept as small as possible.^[93] For values $P > 20$ a loss of individual reduction peaks in the TPR of CuO was demonstrated. Furthermore, *Malet et al.* found smaller error margins in the determination of kinetic parameters E_A and k_0 for the $T_M\text{-}\beta$ analysis described above, if P was kept constant over the TPR series measured.^[93]

2. Methods and techniques

Thus, for a good peak differentiation and a sharp curve shape of the TPR the heating rate β and the amount of reducible species S_0 should be as low as possible and the flow of hydrogen over the sample should be high. Nevertheless, pressure build-up in the reactor (limiting high flow rates), the material of the set-up (possibly limiting the hydrogen content due to stability issues) and the detection limit of the detector (limiting the amount of reducible species and the heating rate) should be considered as well for optimal results.

3. Experimental

3.1 Sample supply

The high purity reference manganese oxides have all been purchased in the highest available purity as follows: MnO 99.99% from Alfa Aesar, Mn₃O₄ 97% from Sigma-Aldrich, Mn₂O₃ 99.99% from Sigma-Aldrich and MnO₂ 99.995% from Strem Chemicals.

The twelve bigger batches of manganese oxides used in the catalytic section of this work have been purchased from different companies in the highest purity offered for batches of ≥ 100 g sample. Purities and suppliers were as follows:

MnO: 99% from Sigma-Aldrich, 99% from Alfa Aesar and 99% from chemPUR

Mn₃O₄: twice 97% from abcr and 97% from Sigma-Aldrich

α -Mn₂O₃: 99.9% from chemPUR, 99% from abcr and 99% from Sigma-Aldrich

β -MnO₂: 89% from Merck, 99.9% from chemPUR and 99.9% from Alfa Aesar

3.2 Characterization and methods

3.2.1 Raman spectroscopy

Raman spectroscopy measurements have been conducted on a DXR Raman Microscope from Thermo Scientific with two different laser sources (532 and 780 nm). Measurements with the green 532 nm laser have been taken at a power of 0.1 mW, whereas the measurements with the red 780 nm laser have been taken at a power of 0.5 mW for the MnO and Mn₃O₄ sample, at a power of 4 mW for the Mn₂O₃ sample and at a power of 10 mW for the MnO₂ sample.

3. Experimental

3.2.2 Temperature programmed oxidation and reduction

The temperature programmed reactions have been measured in a fully automated fixed bed flow set-up equipped with a GAM400 quadrupole mass spectrometer from InProcess Instruments for fast gas analysis. The set-up is fully stainless steel lined and operated with six-port Valco valves for fast and dead-volume free switching and mixing of the gas lines. All gas lines are heated to 120 °C to prevent strong readsorption of gases on the tubing walls. All experiments were conducted in a quartz reactor and heating was provided by a ceramic oven from HTM Reetz GmbH. The temperature was measured in the sample bed inside the reactor with a type K thermocouple (chromel/alumel) to assure the correct temperature. Samples have been fixed between quartz wool plugs and diluted with inert SiC with a particle size of 300 µm to prevent pressure hold-up in the reactor. The purity of the gases which were used in this study was 99.999% for the He supply and 99.995% O₂ in 99.997% He for the oxygen supply. Typically, 100 mg of sample have been weighted out and initially dispersed in 400 mg of SiC. In later experiments, only minimal amounts of SiC have been used around the sample bed, to prevent particle extraction from the reactor.

3.2.3 CO and 2-propanol oxidation

CO oxidation has been measured in the same fixed-bed flow system described in section 3.2.2. Samples have been fixed between quartz wool plugs. The purity of the gases which were used in this study was 99.9999% for the He supply, 99.995% O₂ in 99.999% He for the oxygen supply and 99.995% CO in 99.9999% He. Typically, 50 mg of sample have been used for one experiment.

2-propanol oxidation was performed at atmospheric pressure in a feed composed of 49 mL He and 1 mL O₂. The feed was passed through a saturator at 5 °C to achieve a concentration of around 1.5 vol.-% 2-propanol. A laboratory quartz U-tube fixed bed reactor (4 mm inner diameter, 6 mm outer diameter, 26 cm length) was used, which contained 50 mg of the catalyst. Gas analysis was performed by online gas

3. Experimental

chromatography (GC 6890A, Agilent) equipped with two channels. A combination of two capillary columns (GS-Carbonplot and Plot Mole Sieve 5A) in connection with a thermal conductivity detector (TCD) was used to analyze the permanent gases CO₂, O₂, N₂ and CO. A combination of two capillary columns (HP-FFAP and HP Plot Q) connected to a flame ionization detector (FID) was applied to analyze alkanes, olefins and oxygenates.

3.2.4 Powder X-ray diffraction

Powder X-ray diffraction has been measured on a PANalytical X'Pert PRO MPD instrument with a Cu X-ray tube operated at 40 mA and 40 kV and a goniometer radius of 240 mm. A silicon 'zero background sample holder' was mounted on a sample spinner stage. Intensities were recorded by the position sensitive X'celerator detector with active length of 2.122°. The step size was 0.05° and integration time varied between samples from 100 s/step to 200 s/step. The scan range was between 5 and 80° 2 θ . On the incident beam side, a Soller slit of 0.04 rad, a divergence slit of 1/4°, an anti-scatter slit of 1/2° and a mask of 15 mm were used. For selected measurements a diffracted beam graphite monochromator was utilized. When the monochromator was used, there were no additional slits or masks. Otherwise, divergence slit of 1/4° and Soller slit of 0.04 rad were used together with a Ni-foil filter to reduce the intensity of Cu K-beta X-rays.

The X-ray diffraction (XRD) measurements used for Rietveld analysis were performed in Bragg-Brentano geometry on a Bruker AXS D8 Advance II theta/theta diffractometer, using Ni filtered Cu K α_{1+2} radiation and a position sensitive energy dispersive LynxEye silicon strip detector. The sample powder was filled into the recess of a cup-shaped sample holder, the surface of the powder bed being level with the sample holder edge (front loading).

Phase identification was performed using DIFFRAC.SUITE EVA (Bruker AXS, 2010-2018) in combination with the PDF-4+ database (ICDD, 2018). XRD Data were then evaluated by whole powder pattern fitting according to the Rietveld method as

3. Experimental

implemented in the TOPAS software (version 5, Bruker AXS, 1999-2014). The crystal structures used for the Rietveld fits were obtained from the ICSD Web database (FIZ Karlsruhe).

3.2.5 N₂ and krypton physisorption experiments

For one measurement 100 to 300 mg sample was weighed into a quartz tube. The exact amount is dependent on the volume and available surface area of the sample, since a minimum of 30 cm²/g is needed for the measurement. The sample was thereafter heated to 140 °C under vacuum for 24 h. The pretreated sample tube was than filled with a quartz rod to minimize dead volume and built into the apparatus from *Quantachrome Instruments*. For the N₂ and krypton physisorption experiments a Quantachrome Nova and Quantachrome Autosorb iQ apparatus has been used, respectively. The physisorption measurements which are evaluated following the BET procedure are conducted between 0.05 and 0.3 p/p₀ according to DIN standard. The calculation of the specific surface area is conducted by the Quantachrome NovaWin and Quantachrome ASiQwin software for the N₂ and krypton physisorption experiments, respectively.

4. Phase identification of Mn oxides

4.1 Characterization of the high purity Mn oxides

In the first part of this work, it was the aim to identify a combination of analytical techniques for the distinction between different MnO_x phases. Thus, samples of highest chemical and phase purity are needed. To this end, bulk samples with the highest purity commercially available have been used as reference materials in this investigation. All samples feature a nominal purity of $\geq 99.99\%$ except for Mn_3O_4 which was available in 97% purity only. To make sure no other crystalline impurities were present, XRD measurements have been taken of all samples, shown in Figure 15. The measured diffraction patterns perfectly match the literature references and the reflexes are very sharp, indicating a high crystallinity, large crystallites and a phase pure-sample.

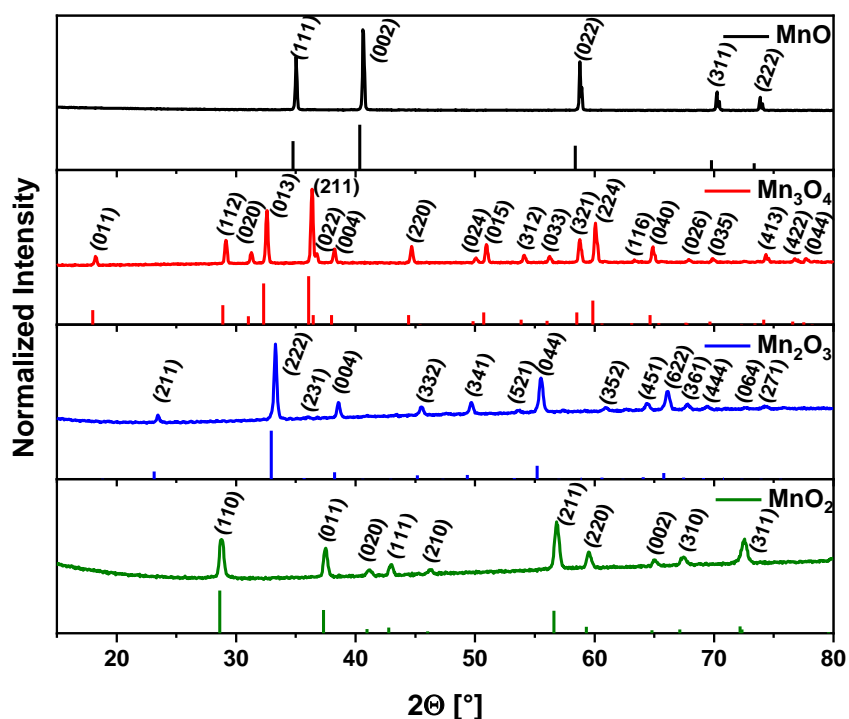


Figure 15: Measured XRD data and reference line spectra for all manganese oxide samples. Additionally, Laue indices are given for all individual reflexes.

4. Phase identification of Mn oxides

To further investigate the phase purity of the samples a Rietveld refinement has been calculated from the XRD data (given in Figure 16). All reference patterns used in the calculation have been taken from the international crystal structure database (ICSD) and a perfect fit could be found between the investigated and reference samples. Thus, the results of the analysis indicate a purity of 100% for all samples.

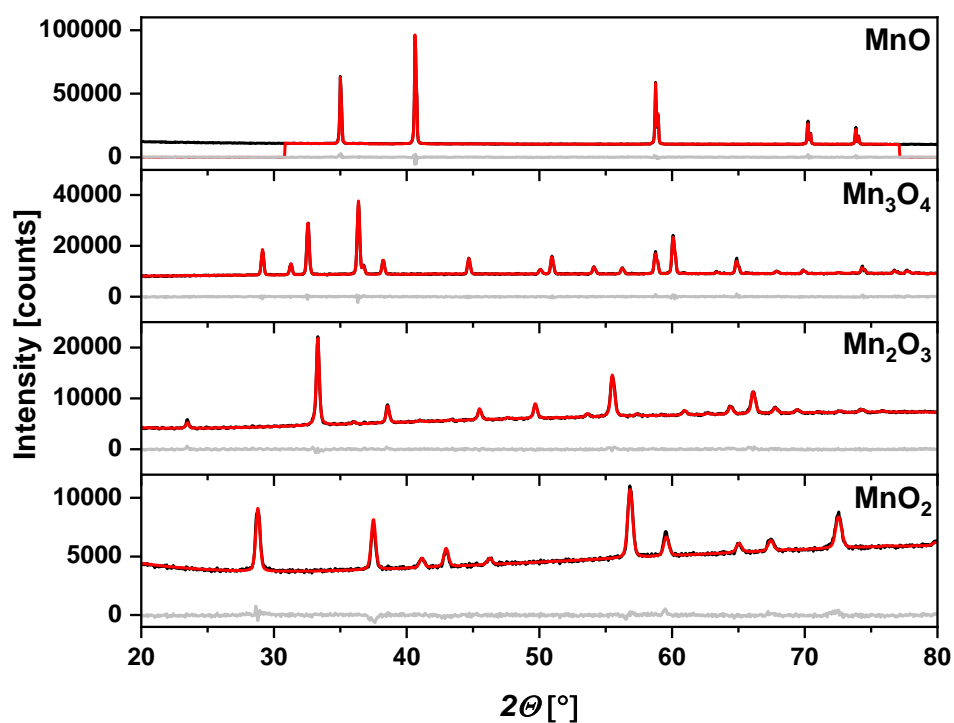


Figure 16: Rietveld refinement of all investigated samples depicting the measured XRD pattern (black), the fitted data (red) and the difference between those two (grey).

For further insights into the samples, N₂ physisorption has been measured and the BET specific surface area S_{BET} determined (Table 1). All materials exhibit a very small surface area below 1 m²/g which again indicates big particles for all samples.

Table 1: Specific surface area measured by N₂ BET for all high purity samples.

	MnO	Mn ₃ O ₄	Mn ₂ O ₃	MnO ₂
S_{BET, N_2} [m ² /g]	0.65	0.65	0.43	0.13

4.2 Temperature programmed oxidation

4.2.1 Parameter variation

To gain a good peak differentiation in the TPO experiment the limits of the used set-up have been tested first. To this end, MnO has been chosen as sample, because it exhibits the highest oxygen uptake capabilities. Following the advice of *Malet and Caballero*^[93] the parameter P given in equation (25) was minimized as far as the set-up restrictions allowed. Thus, the influence of a high and low heating rate β was investigated (compare Figure 17). A better peak differentiation is visible for the lower heating rate of 2 K/min than for the faster heating of 10 K/min, and the integration results indicate different transitions (compare Table 2). It needs to be noted, that the comparison of the peak integrals in the temperature domain in Figure 17 is not feasible. Thus, an additional plot was added showing the comparison of the two measurements in the time domain to increase comparability of the integration areas.

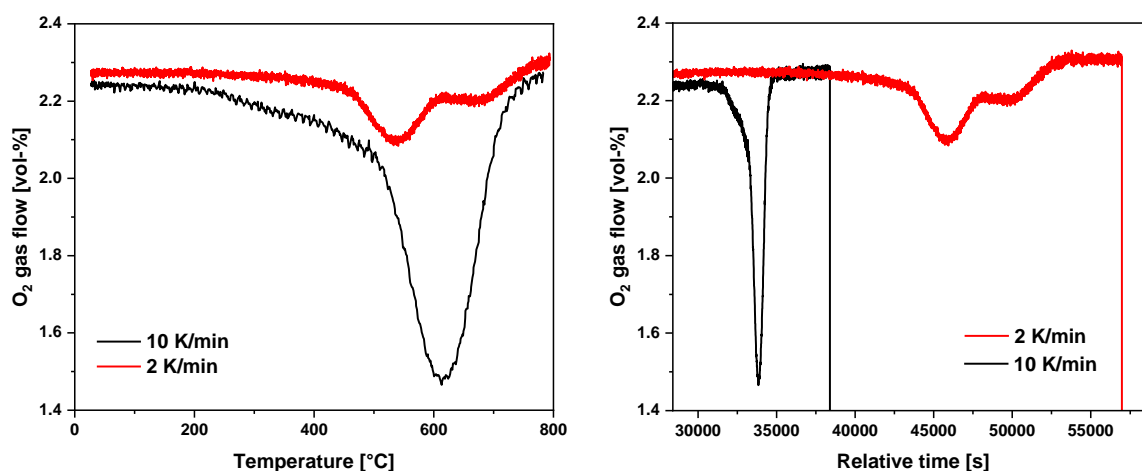


Figure 17: TPO profiles of MnO for heating rates of 2 and 10 K/min in the temperature domain (left) and the time domain (right).

The second parameter to be varied was the concentration of oxygen. Unfortunately, following equation (25) suggests a high oxygen concentration in the inlet of the reactor which on the other hand is detrimental for the analytics of the set-up. The secondary electron multiplier (SEM) of the mass spectrometer was damaged in the

4. Phase identification of Mn oxides

initial phase of the parameter testing, when high concentrations of O₂ were supplied to the reactor and induced high noise in the measurements (compare the signal to noise ratios in chapters 4.1 and 4.2). Thus, an O₂ concentration as low as possible was sought to protect the new SEM which was switched out after the parameter variation.

Table 2: Integration results of all experiments during the parameter variation tested on MnO.

Results	Conditions	2 K/min 2 vol-% O ₂	10 K/min 2 vol-% O ₂	2 K/min 1 vol-% O ₂	2 K/min 2 vol-% O ₂	2K/min 5 vol-% O ₂
	Integration result [mmol O ₂]		0.403	0.258	0.353	0.403
Sample amount [mg]		99.5	100.9	100.9	99.5	100.5
Sample amount [mmol]		1.403	1.422	1.422	1.403	1.417
Stoichiometry after reaction		MnO _{1.56}	MnO _{1.36}	MnO _{1.50}	MnO _{1.56}	MnO _{1.51}

Three different concentrations (i.e. 1%, 2% and 5%) have been used for comparison and roughly the same signal to noise ratios were obtained in all cases (compare Figure 18). Furthermore, the work of *Monti et al.*^[94] suggests keeping the total reactant gas uptake at the peak maximum (roughly 0.18 vol-% of O₂) between 10% and 66% of the initial inlet concentration. For these reasons, a concentration of 1 vol-% oxygen in the feed was chosen for further experiments.

During the initial testing a transformation of the MnO_x sample phase was discovered during pressing and sieving, due to the pressure applied. Since this work is aimed at method development and phase analysis, an undeterminable change of phase prior to the experiments could not be tolerated. Therefore, pressing and sieving has been omitted and the samples were used as received. For this reason, the particle size could not be optimized regarding the pressure drop in the reactor. The flow rate \dot{V} , which should have been chosen as high as possible to minimize P , had to be fixed at 50 mL/min to prevent the sample from being pushed out of the reactor tube. Fortunately, all samples were of high crystallinity and featured large crystallite sizes which inhibited huge pressure build-ups in the reactor. As an alternative, a dilution of

4. Phase identification of Mn oxides

the samples with inert SiC was tested to reduce pressure in the reactor, but was later deemed unnecessary, since better signal to noise ratios could be obtained without the SiC at the same conditions.

The last parameter influencing P is the amount of oxidizable species which should be chosen as low as possible. Unfortunately, the initial amount of 100 mg sample could not be lowered without losing most signal intensity.

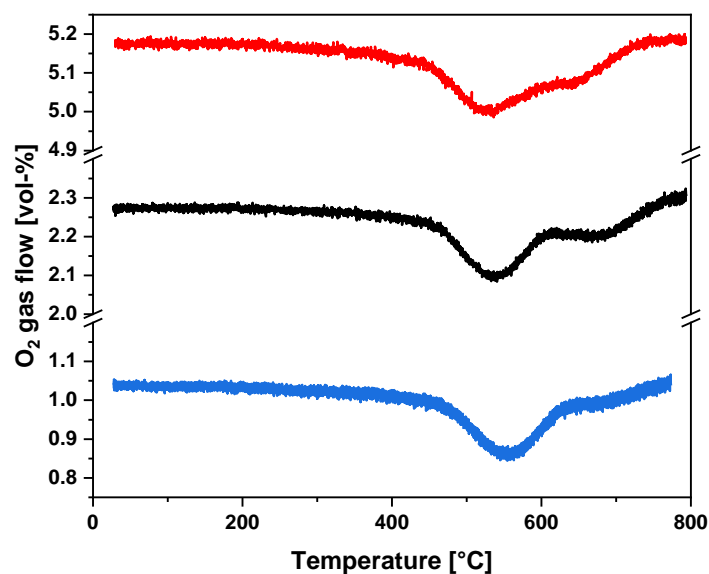


Figure 18: TPO profiles of MnO at a heating rate of 2 K/min with an initial oxygen concentration of 1, 2 and 5 vol-%.

4.2.2 TPO of high purity Mn oxides

To gain insight into the limitations of the TPO technique and for a possible differentiation of the oxidation states of oxidic Mn samples, the thermodynamically most stable binary oxide phases of manganese have been used as reference materials in the highest available purity: MnO (Manganosite), Mn₃O₄ (Hausmannite), α-Mn₂O₃ (Bixbyite) and β-MnO₂ (Pyrolusite).

Applying the previously determined parameters, TPO data of MnO was recorded. The results are illustrated in Figure 19. The exact numerical values of the integration and the calculated stoichiometries of all experiments are given in Table 3. The TPO of MnO exhibits two different redox processes: First, around 550 °C the sample takes up oxygen from the feed and is oxidized from pure MnO to Mn₂O₃. This process is a standard oxidation reaction which is expected for a TPO experiment. Around 800 °C on the other hand a liberation of oxygen from the sample can be observed which is added to the inlet concentration of roughly 1.07 vol-% oxygen and is thus giving rise to a positive peak. This reaction is a thermal reduction even though slightly oxidizing conditions are applied during the experiment.

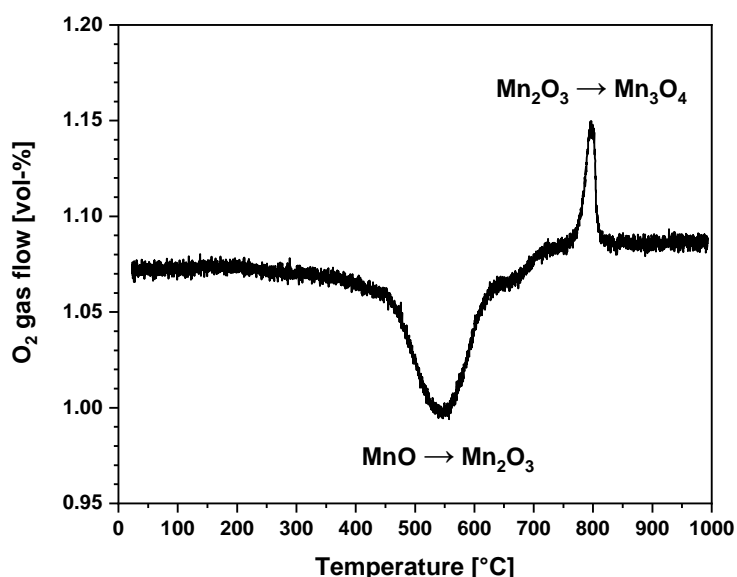
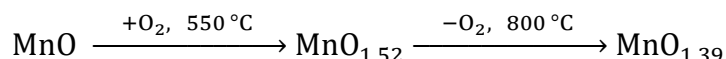


Figure 19: TPO data of MnO and the chemical transitions during the reaction.

4. Phase identification of Mn oxides

Looking at the exact stoichiometric calculation of the whole reaction pathway yields:



The results indicate a very good fit for the first transition of MnO to Mn₂O₃, but the calculated stoichiometry for the second transition is a bit off the expected MnO_{1.33} for the Mn₃O₄ phase. This might be due to inaccuracies in the baseline subtraction during integration, since a slight baseline drift is visible in the data, but an exact extrapolation is not possible due to the slight overlap of the two signals.

To gain additional insights, the experiment has been stopped at 700 °C and the received sample was measured in XRD to gain information on the present phase at this stage. The same has been done with the sample after TPO at 1000 °C. Both XRD patterns are shown with the respective reference patterns of α-Mn₂O₃ and Mn₃O₄ Hausmannite in Figure 20. The investigated samples match the references which indicates a phase pure transition of MnO first to α-Mn₂O₃ and afterwards to Mn₃O₄ given by:

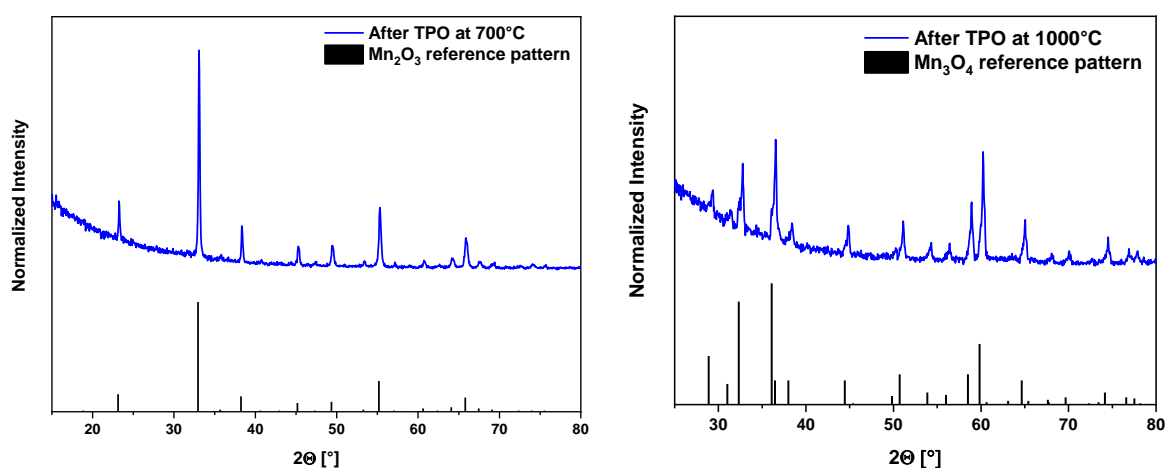
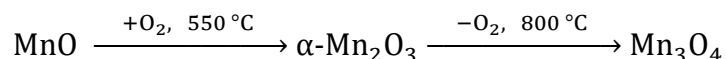


Figure 20: Left: XRD pattern of the sample formed from MnO in the TPO experiment stopped at 700 °C and a reference line pattern of α-Mn₂O₃. Right: XRD pattern of the sample formed from MnO at the end of the TPO experiment at 1000 °C and a reference line pattern of Mn₃O₄.

4. Phase identification of Mn oxides

The TPO data obtained from Mn_3O_4 is shown in Figure 21. This sample does not exhibit any feature which means it is not undergoing any redox reaction at the given conditions up to 1000 °C. Thus, Mn_3O_4 is stable over the whole TPO procedure and a “blind” sample to this technique. Therefore, a complementary technique is needed to fully investigate a bulk MnO_x sample of unknown composition, since only a mismatch of stoichiometries or the absence of features indicate the Hausmannite phase.

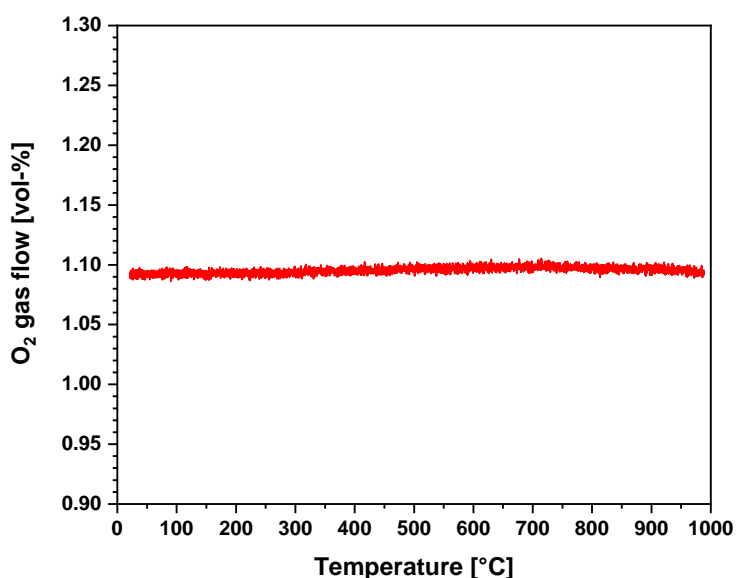
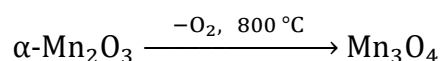


Figure 21: TPO data of Mn_3O_4 .

The TPO of the high purity $\alpha\text{-Mn}_2\text{O}_3$ matches the previous findings perfectly (compare Figure 22 and Table 3). Only the high temperature (800 °C) thermal reduction can be found, which was also present in the MnO sample. Looking at the exact stoichiometry of this transition yields $\text{MnO}_{1.33}$ after reaction which is a perfect fit for the Hausmannite phase and the reaction is given by:



This indicates again that for the chosen conditions a deconvolution of the individual redox transitions is possible, allowing for a quantitative analysis of the initial composition of a sample as long as it is pure MnO_x or the MnO_x content in the sample is known.

4. Phase identification of Mn oxides

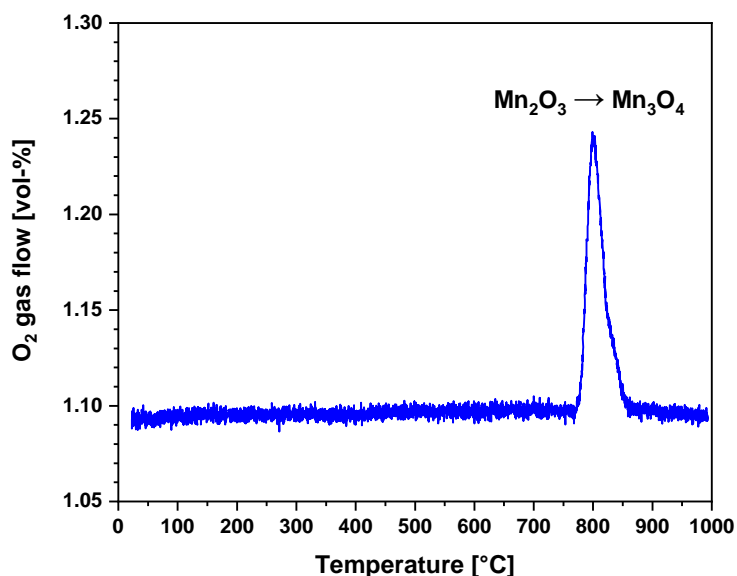


Figure 22: TPO data of α -Mn₂O₃ and the chemical transition during the reaction.

The TPO of the last thermodynamically stable manganese oxide phase, β -MnO₂, can be seen in Figure 23. This last sample in the investigated series matches again the previous insights and features two distinct transitions, the first one at roughly 550 °C and the second around 800 °C. Both events show an oxygen liberation from the sample, identifying them as thermal reductions. The calculated stoichiometries after the two reduction reactions fit the expected transitions nicely with MnO_{1.50} and MnO_{1.34} respectively. Thus, the reaction pathway can be described as:

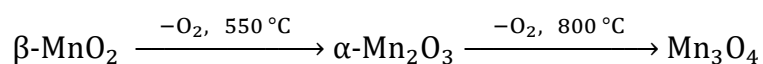


Figure 24 gives a comprehensive picture of all MnO_x samples. Taking the findings of all high purity, thermodynamically stable Mn oxides into account a clear distinction between the low temperature and the high temperature feature can be drawn. MnO and MnO₂ are first transformed into the stable α -Mn₂O₃ at 550°C, whereas Mn₂O₃ and Mn₃O₄, which are more stable at high temperatures, do not undergo any changes. Afterwards, at 800 °C all samples are completely transformed into the thermodynamically most stable Mn₃O₄ Hausmannite phase.

4. Phase identification of Mn oxides

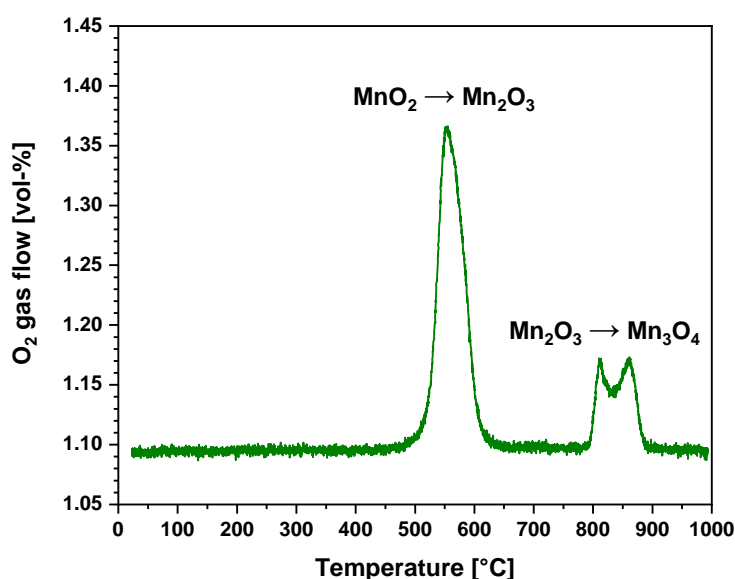
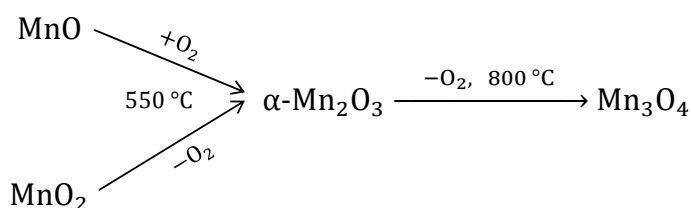


Figure 23: TPO data of β -MnO₂ and the chemical transitions during the reaction.

The complete reaction network can be illustrated as:



Since the TPO presented here is a thermodynamically driven experiment and all samples used for this investigation represented the thermodynamically most stable phases of their respective oxidation state it is to be expected that the same transitions will be visible for other MnO_x phases and amorphous samples. This means that first all Mn²⁺ (except for the stable Mn²⁺ in the Hausmannite phase) and Mn⁴⁺ is converted to Mn³⁺ in the α -Mn₂O₃ phase and can be quantified. Thereafter, all α -Mn₂O₃ is converted to Mn₃O₄ which allows quantification of the integral amount of Mn³⁺ (the amount formed during reaction and the amount initially present in the material).

Under the assumption that the sample consists of only MnO_x or the amount of other species in the sample is known and can be subtracted (e.g. MnO_x on a known amount of support) it is possible to quantify the amount of Mn₃O₄ initially present in the sample by subtracting all reacted species so only the amount of “TPO inert” Mn₃O₄ is left.

4. Phase identification of Mn oxides

Table 3: Numerical values used in the calculation of TPO stoichiometries for the high purity samples.

Results	Sample	MnO	Mn ₃ O ₄	Mn ₂ O ₃	MnO ₂
	Integration 1. peak [mmol O ₂] ^a		0.361	No	-
Integration 2. peak [mmol O ₂] ^a		-0.094	reaction	-0.107	-0.092
Sample amount [mg]		98.3	101.3	100.9	101.8
Sample amount [mmol]		1.386	0.443	0.639	1.171
Stoichiometry after 1. event		MnO _{1.52}	Mn ₃ O ₄	Mn ₂ O ₃	MnO _{1.50}
Stoichiometry after 2. event		MnO _{1.39}	Mn ₃ O ₄	MnO _{1.33}	MnO _{1.34}

^a Negative values indicate an oxygen liberation by the sample; positive values indicate a consumption of oxygen by the sample.

Thus, investigation of MnO_x samples by means of temperature programmed oxidation can yield significant insights into their oxidation state and phase composition.

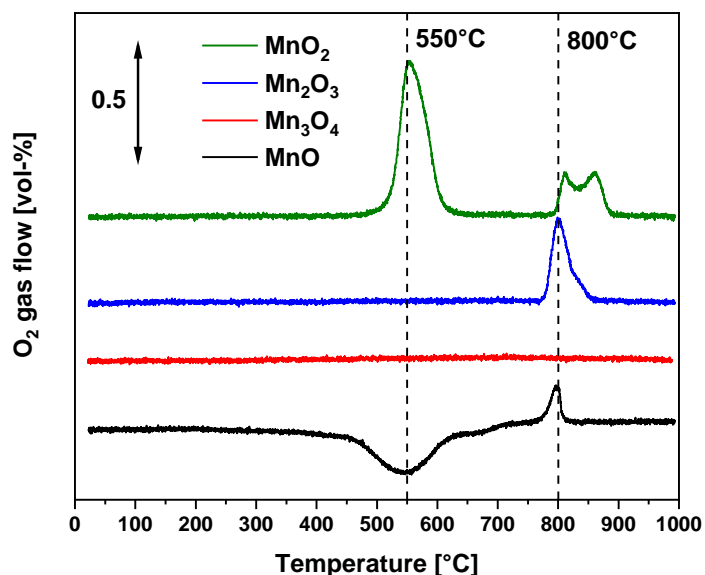


Figure 24: TPO data of all high purity MnO_x samples. The temperature regimes of the main transitions are indicated at 550 °C and 800 °C. The Y-axis was offset for better visibility. The baseline concentration was 1.1 vol-% of O₂.

4. Phase identification of Mn oxides

4.2.3 Investigation of MnO_x samples of unknown composition

As a proof of principle three samples of unknown composition have been investigated which were prepared by a precipitation of Mn(II) and Mn(III) acetate and calcined at differing temperatures in synthetic air afterwards. These samples have been provided by *Stefanie Becker* from the group of *Prof. Dr. Malte Behrens* including XRD data for additional insights into the sample compositions.

The first sample investigated was calcined at the highest temperature of 800 °C after synthesis and the XRD pattern exhibits a perfect match with the reference pattern of α -Mn₂O₃ (compare Figure 25).

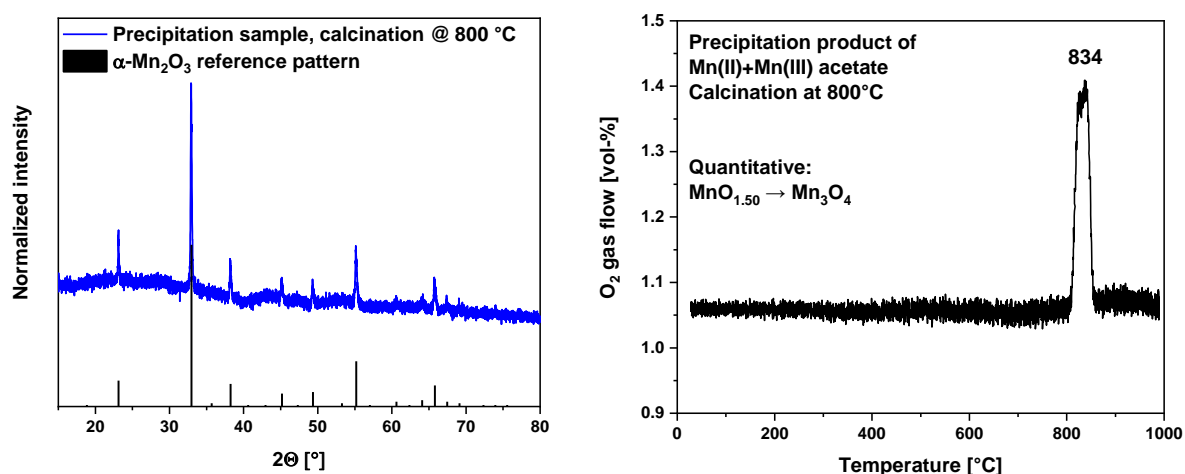


Figure 25: Left: Measured XRD pattern of the unknown precipitated sample calcined at 800 °C and a reference line pattern of α -Mn₂O₃. Right: TPO measurement of the same sample highlighting the peak temperatures and giving the calculated quantification of the reaction.

Using the previously described method for calculating the initial composition of the material a perfect agreement can be found with the results of the XRD measurement. The TPO experiment suggests an initial composition of Mn₂O₃ and confirms the phase analysis results of the XRD.

The same findings can be achieved for the sample which was calcined at 600 °C although the signal to noise ratio of the XRD is higher in this case indicating a lower degree of crystallinity. However, since the TPO is not reliant on the crystallinity of the sample the amorphous portion of the investigated material is just as identifiable as

4. Phase identification of Mn oxides

crystalline amounts and the quantification matches again an initial phase composition of Mn_2O_3 (compare Figure 26).

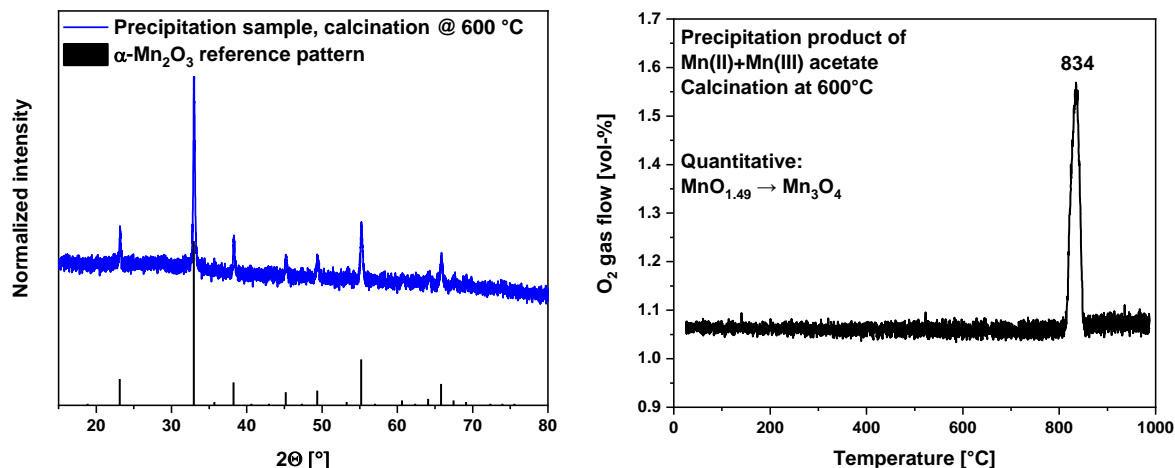
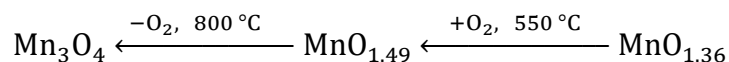


Figure 26: Left: Measured XRD pattern of the unknown precipitated sample calcined at 600 °C and a reference line pattern of $\alpha\text{-Mn}_2\text{O}_3$. Right: TPO measurement of the same sample highlighting the peak temperatures and giving the calculated quantification of the reaction.

The last sample of the series is the precipitation product which has not been calcined at all and was investigated as received. The XRD pattern shows very broad reflexes and a low signal to noise ratio which indicates the presence of high amounts of amorphous material. Nevertheless, the crystalline portion of the sample which is visible in the XRD pattern matches the Mn_3O_4 Hausmannite phase and indicates it as the only one present in the sample. Thus, no features should be expected in the TPO experiment at all, but two events confirm the presence of Mn^{2+} and Mn^{3+} in the sample which are not bound in the Hausmannite phase. Assuming the sample was pure MnO_x and thus consists of 100% Hausmannite after the TPO experiment, the exact stoichiometry of the present transition can be calculated back as:



The initial composition of the sample has approximately the stoichiometry of Mn_3O_4 . Nevertheless, the TPO technique can quantify the amount of Mn^{2+} and Mn^{3+} not bound in the Hausmannite phase.

4. Phase identification of Mn oxides

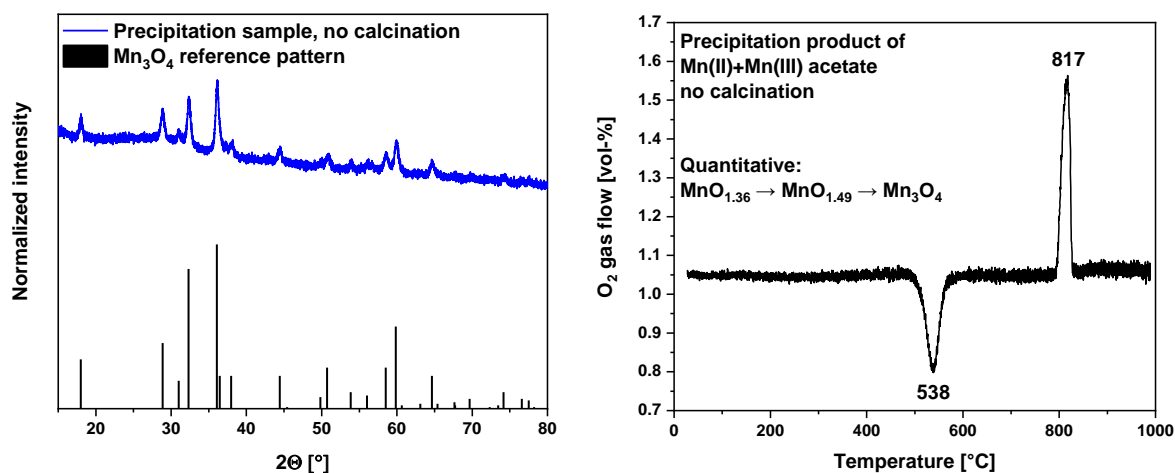


Figure 27: Left: Measured XRD pattern of the unknown precipitation sample without calcination and a reference line pattern of Mn₃O₄. Right: TPO measurement of the same sample highlighting the peak temperatures and giving the calculated quantification of the reaction.

Furthermore, a complete deconvolution of the sample composition is possible by utilizing only the data obtained from the TPO. Detailed numerical values for this calculation can be taken from Table 4. The initially unknown MnO_x sample consisted of only 4.4 wt-% crystalline Mn₃O₄ in the Hausmannite phase which gave rise to the XRD pattern of the sample. 12.6 wt-% of the material are amorphous Mn²⁺ oxides (calculated as MnO) and the remaining 83.0 wt-% are Mn³⁺ species (calculated as Mn₂O₃).

In conclusion, the TPO was shown to be applicable for the investigation of unknown samples which elude the investigation by XRD due to being fully or partially amorphous. Assuming a pure MnO_x sample or a known amount of MnO_x in an otherwise inert sample raises the opportunity to completely deconvolute the initial composition of the oxide and quantify the amount of all oxidation states present. If other complementary techniques are used to quantify the amounts of Mn₃O₄, it is not necessary to make any initial assumptions and a complete deconvolution of the composition is always possible.

4. Phase identification of Mn oxides

Table 4: Numerical data used in the calculation of the initial composition of the non-calcined precipitation sample.

	Precipitation sample no calcination
Integration 1. peak [mmol O ₂] ^a	0.0423
Integration 2. peak [mmol O ₂] ^a	-0.1066
Initial sample weight [mg]	102.1
Calculated sample weight after TPO [mg]	100.0
Calculated Mn ₃ O ₄ amount after TPO [mmol]	0.4372
Stoichiometry after 1. event	MnO _{1.52}
Stoichiometry after 2. event	MnO _{1.39}
Sample amount reacted during TPO [mmol]	0.4264
Mn ³⁺ amount reacted during TPO [mmol]	1.2792
Initial amount of Mn ₃ O ₄	0.0192 mmol or 4.4 wt-%
Mn ²⁺ amount reacted during TPO	0.1692 mmol or 12.6 wt-%
Initial Mn ³⁺ amount reacted during TPO	1.11 mmol or 83.0 wt-%

^a Negative values indicate an oxygen liberation by the sample; positive values indicate a consumption of oxygen by the sample.

4.3 Temperature programmed reduction

To gain more insight into the redox behavior of the high purity MnO_x samples temperature programmed reduction experiments have been conducted on the materials. The parameters employed for the TPO have been kept except for the amount of reaction gas, which was nearly doubled to 1.8 vol-% of H_2 . This was done to compensate for the higher peak consumptions during the TPR experiments which reached up to 0.8 vol-% of H_2 and should be kept between 10% and 66% of the concentration of the inlet flow. P values have been calculated for the chosen parameters using equation (25) and depending on the sample used (the amount of reducible species varies at constant sample weight) P ranges from 0.2 to 0.7 K. These values are very small and fulfill the condition $P < 20 K$ which was the predicted limit of *Malet and Caballero* for good peak resolution and differentiation.^[93] The measured TPR data has been compiled in Figure 28 and the exact numerical values used in the calculation of the stoichiometry after the TPR experiment are given in Table 5.

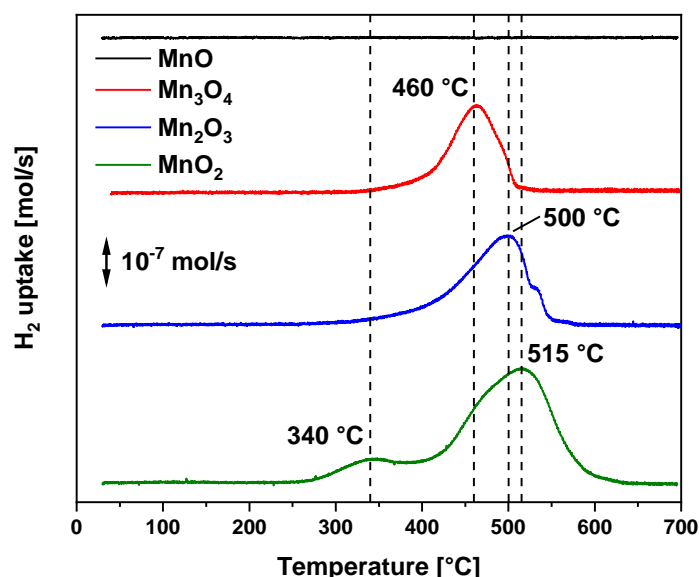


Figure 28: TPR data of all high purity MnO_x samples. The temperature regimes of the main transitions are indicated with dashed lines. The Y-axis was offset for better visibility.

4. Phase identification of Mn oxides

Table 5: Numerical values used in the calculation of TPR stoichiometries for the high purity samples.

Sample	MnO	Mn ₃ O ₄	Mn ₂ O ₃	MnO ₂
Results				
Peak integration [mmol H ₂]	No reaction	0.422	0.614	1.110
Sample amount [mg]	100.3	99.4	102.1	99.1
Sample amount [mmol]	1.414	0.434	0.647	1.140
Stoichiometry after reaction	MnO	MnO _{1.01}	MnO _{1.03}	MnO _{1.03}

The MnO sample exhibits no reaction under reductive conditions, which was to be expected since a further reduction to metallic Mn has earlier been reported above 1200 °C.^[43,46]

Mn₃O₄ on the other hand can be reduced in hydrogen and is giving rise to one asymmetric peak at 460 °C in the TPR experiment which indicates first order kinetics for the reduction of Mn₃O₄. Integration of the peak area reveals a quantitative reduction to MnO, which makes the TPR a complementary technique to the TPO enabling the quantification of the amount of Mn₃O₄ in the sample.

Mn₂O₃ is quantitatively reduced to MnO as well and the main reduction event centered around 500 °C is again an asymmetric transition indicating first order reduction kinetics, although a very small shoulder at very high temperatures can be seen which cannot be attributed to any other MnO_x bulk transition.

The last high purity sample investigated clearly show different regimes of reduction. First, at roughly 340 °C MnO₂ is slightly reduced, but the initial reduction event is not finished at a heating speed of 2 K/min before the main reduction takes place with a peak temperature of 515 °C transforming the whole sample into MnO. The general peak shape of the main reduction event seems to be asymmetric again, although at 500 °C an underlying signal can be assumed giving rise to a slight shoulder. Taking the multitude of visible features into account, the sample seems to transition into different phases at differing temperatures, but the processes are so slow that the reduction to another phase starts before the initial transition is completed.

4. Phase identification of Mn oxides

In conclusion, the TPR exhibits some fine structure as well, but the individual events cannot be completely deconvoluted to quantify each individual reduction step of the samples. Nevertheless, the integral hydrogen consumption during the TPR experiment can be quantified and all high purity samples are fully transformed to the MnO phase. These insights can help to again quantify the molar amount of MnO_x in samples of unknown composition and quantify any amounts of Mn₃O₄ of the Hausmannite phase in a sample. Thus, the TPO and TPR can be used in combination to fully understand sample compositions.

4.4 Raman spectroscopy of the high purity samples

To be able to identify the different samples based on their internal molecular bonds, Raman spectroscopy was conducted on the four manganese oxide samples for an understanding of the vibrational modes. Two different laser wavelengths (green 532 nm and red 780 nm) have been employed for this study. Only few groups report Raman spectra of pure manganese oxides and a lot of these results are not in agreement with each other. Thus, this referencing study of MnO_x Raman spectra is still highly relevant and fits right into the controversial discussion. Table 6 lists all Raman bands, the respective references and assignments made for the different signals discussed in this section.

The spectrum of MnO (shown in Figure 29) features four peaks regardless of the laser wavelength used, but signal intensity is higher for the 532 nm laser. Four bands are visible featuring a broad peak in the region of 1080-1000 cm⁻¹, a sharp one at 650 cm⁻¹, another broadened feature centered around 560 cm⁻¹ and a weak signal at 310 cm⁻¹. *Kapteijin et al.* found the same peak distribution,^[95] whereas other references did not include all of the features observed in this work. The three most intense signals have also been found by the group of *Mironova-Ulamane*^[96] and by *Chou and Fan*^[97]. Further agreement can be found with *Julien et al.*^[98] who reported broad bands around 654 cm⁻¹ and 531 cm⁻¹ and a weak band at 591 cm⁻¹, but also a weak signal at 250 cm⁻¹ which has not been observed by any other group. Thus, it is likely that the feature at 250 cm⁻¹ is not related to MnO and will not be discussed in more detail. *Strohmeier and Hercules* found only one broad signal for MnO at 600-450 cm⁻¹.^[99]

Some agreement can be found on the attribution of the peak at 650 cm⁻¹ to Mn₃O₄, which was formed during the acquisition of the spectra.^[96,97] Mn₃O₄ is the most Raman active manganese oxide (roughly 10 times higher intensities than the other investigated samples) and the feature at 650 cm⁻¹ is the most intense one, which explains a detection of Mn₃O₄ even in trace amounts. These findings agree with the observed peak at 310 cm⁻¹, which is also a part of the Mn₃O₄ spectrum. The signal at 531 cm⁻¹ was attributed to the stretching mode of Mn-O in the cubic cage of the Mn²⁺ cation by *Julien et al.*^[98] *Chou and Fan* on the other hand explained this broad signal

4. Phase identification of Mn oxides

as a combination of two peaks at 530 cm^{-1} and 505 cm^{-1} , which are related to magnetic excitation and two-phonon transversal optical (2TO) scattering, respectively.^[97] Furthermore, they attributed the broad signal around 1000 cm^{-1} to two-phonon longitudinal (2LO) scattering. *Mironova-Ulmane et al.* compared the presented results with the well understood Raman spectrum of NiO, which features the same crystal structure and similar lattice parameters.^[96] Based on this comparison, the peak at 530 cm^{-1} was attributed to a LO mode and the broad signal around 1050 cm^{-1} was reported to be constituting of two different peaks (TO+LO and 2LO modes). In summary, the two broad signals around 1050 and 560 cm^{-1} can be used to identify the MnO phase from the Raman spectrum.

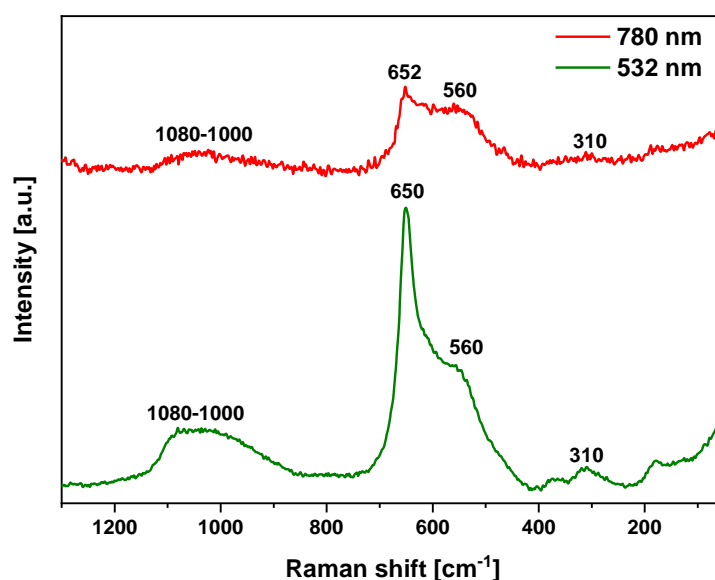


Figure 29: Raman spectrum of bulk MnO measured using a 532 nm and a 780 nm laser.

The spectra of Mn_3O_4 presented in Figure 30 both exhibit five peaks at the same positions. The intensities of the peaks at 660 and 320 cm^{-1} is higher when applying 532 nm laser radiation, whereas the rest of the visible signals are more intense with the 780 nm laser.

In this study, signals are present at 660 , 478 , 376 , 320 and 292 cm^{-1} . The same distribution was only measured once before by *Lutz et al.*^[100] No other group found the peak at 292 cm^{-1} , which could indicate a common impurity in the sample, due to the preparation method. *Lutz et al.* decomposed $\text{MnSO}_4 \cdot 4\text{ H}_2\text{O}$ to Mn_3O_4 , whereas

4. Phase identification of Mn oxides

for this study the sample was commercially purchased in 97% purity from Sigma Aldrich, but without the declaration of the preparation method or possible contaminants. Thus, the peak at 292 cm^{-1} will be attributed to an unknown impurity in the sample. The other four peaks have been previously observed by *Julien et al.*^[98] and *Buciuman et al.*^[101]. The bands at 660 , 376 and 320 cm^{-1} with the exception of the signal at 478 cm^{-1} , which has the lowest intensity of all signals, have been confirmed by an additional four groups.^[95,96,99,102] Thus, Mn_3O_4 is the only one of the present samples, where all reported Raman spectra are in agreement. This is probably owed to the high Raman activity of the material. Unfortunately, only the most intense signal has been assigned in literature up to this point. The peak at 660 cm^{-1} is characteristic for spinel type structures. It is the A_{1g} mode corresponding to the Mn-O breathing vibration of Mn^{2+} in a tetrahedral coordination.^[98,102] This signal is the most prominent feature of Mn_3O_4 and can be assigned as the characteristic feature. In addition, the signals at 376 and 320 cm^{-1} are also indicative of Mn_3O_4 .

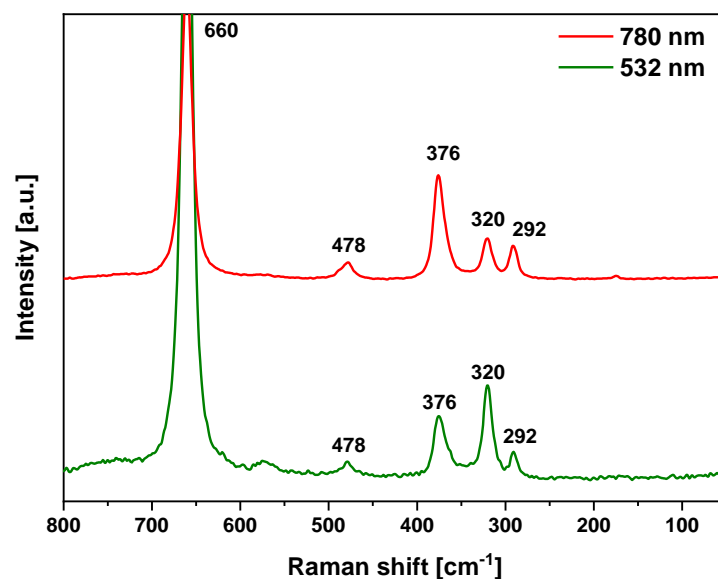


Figure 30: Raman spectrum of bulk Mn_3O_4 measured using a 532 nm and a 780 nm laser.

4. Phase identification of Mn oxides

Table 6: List of all observed Raman bands, their assignments and the respective references for all MnO_x samples.

Sample	Raman shift [cm ⁻¹]	Assignment	References
MnO	1080-1000	2LO mode by ^[97] TO+LO and 2LO by ^[96] attributed to Mn ₃ O ₄	this work, ^[95] , ^[96] , ^[97]
	650		this work, ^[95] , ^[96] , ^[97] , ^[98]
	600-450 split into:		this work, ^[95] , ^[96] , ^[97] , ^[98] , ^[99]
	591		^[98]
	560		this work, ^[95]
	531	Mn-O stretching by ^[98] 2TO mode by ^[97] LO mode by ^[96]	^[96] , ^[97] , ^[98]
	310	attributed to Mn ₃ O ₄	this work, ^[95]
	250	possible impurity	^[98]
Mn₃O₄	660	Mn-O breathing vibration	this work, ^[95] , ^[96] , ^[98] , ^[99] , ^[100] , ^[101] , ^[102]
	478		this work, ^[98] , ^[100] , ^[101]
	376		this work, ^[95] , ^[96] , ^[98] , ^[99] , ^[100] , ^[101] , ^[102]
	320		this work, ^[95] , ^[96] , ^[98] , ^[99] , ^[100] , ^[101] , ^[102]
	292	possible impurity	this work, ^[100]
α-Mn₂O₃	697		this work, ^[95] , ^[98] , ^[101]
	672		^[103]
	645		this work, ^[95] , ^[98] , ^[101]
	620		^[103]
	592		^[98]
	565		^[103]
	481		^[98]
	360-390	attributed to Mn ₃ O ₄ by ^[101]	^[101]
314	attributed to Mn ₃ O ₄ by ^[101]	this work, ^[95] , ^[98] , ^[101]	
196		this work, ^[98]	
β-MnO₂	754	Mn-O-Mn deformation	this work, ^[98]
	660	Mn-O stretching vibration	this work, ^[98] , ^[101] , ^[104] , ^[105]
	577	Mn-O-Mn deformation	this work, ^[101] , ^[104] , ^[105]
	532	Mn-O stretching vibration	this work, ^[98] , ^[101] , ^[104]
	486		^[98]
	377		^[98]
	319		^[98]

4. Phase identification of Mn oxides

The Raman data of α - Mn_2O_3 available in literature is more controversial than for the species discussed before. Spectra acquired in this study are given in Figure 31.

In the present data, four signals are visible at Raman shifts of 697, 645, 314 and 196 cm^{-1} . *Kapteijn et al.* found the same signal distribution but ended the measurement at 200 cm^{-1} . However, looking at the presented data in the publication showed a rising intensity at the end of the measurement range, which might indicate the presence of the 196 cm^{-1} feature.^[95] The group around *Julien* reported signals corresponding to the four peaks described above, but found two additional signals at 592 and 481 cm^{-1} .^[98] The results of *Buciuman et al.* are in agreement with the signals at 697, 645 and 314 cm^{-1} , but they found an additional broad band at 360-390 cm^{-1} .^[101] *White and Keramidas* on the other hand, found peaks at 672, 620 and 565 cm^{-1} exclusively.^[103] *Strohmeier and Hercules* reported α - Mn_2O_3 to have no Raman activity at all.^[99]

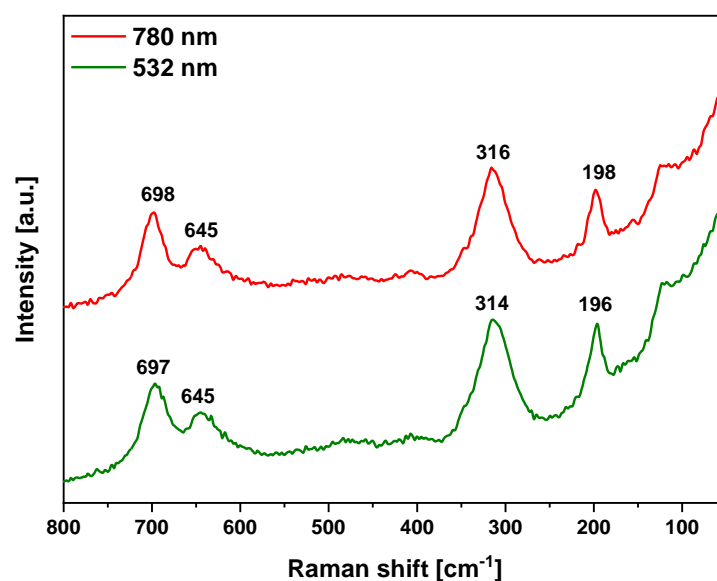


Figure 31: Raman spectrum of bulk α - Mn_2O_3 measured using a 532 nm and a 780 nm laser.

All literature reports and the present data share the two features around 697-672 and 645-620 cm^{-1} . Furthermore, except for *White and Keramidas* the feature at 314 cm^{-1} is also commonly observed. The signals at 592, 565, 481 and 390-360 cm^{-1} have all been observed only once and might be impurities of the individual measurements, but those could also be additional modes of α - Mn_2O_3 since factor-group analysis

4. Phase identification of Mn oxides

performed by *Julien et al.* predicted 22 Raman-active modes ($4A_g + 4E_g + 14F_g$).^[98] The peak at 192 cm^{-1} has previously been observed as well and can therefore be attributed to the spectrum of $\alpha\text{-Mn}_2\text{O}_3$. *Buciuman et al.* assigned the peaks at $650\text{-}640\text{ cm}^{-1}$, $390\text{-}360\text{ cm}^{-1}$ (which was only measured by them) and 310 cm^{-1} to a Mn_3O_4 formation during the measurement. This seems plausible, since Mn_3O_4 is the thermodynamically most stable Mn oxide and can be formed under atmospheric conditions if enough heat is supplied. However, the ratio of the peaks at 645 and 314 cm^{-1} are not in alignment with the spectra previously measured for Mn_3O_4 . Furthermore, the transition of $\alpha\text{-Mn}_2\text{O}_3$ to Hausmannite is only possible at temperatures above $900\text{ }^\circ\text{C}$. For the present study a laser power of 0.1 mW was employed, which makes the formation of such a high temperature on the samples surface unlikely. Therefore, the conclusion can be drawn that all signals in this work are characteristic for $\alpha\text{-Mn}_2\text{O}_3$.

The Raman spectra of $\beta\text{-MnO}_2$ (compare Figure 32) exhibit different patterns depending on the laser wavelength used for excitation. Both spectra share three features in the regions $765\text{-}754$, $667\text{-}660$ and $539\text{-}532\text{ cm}^{-1}$, but only the spectrum acquired with the 780 nm laser has an additional band at 577 cm^{-1} . All those peaks have previously been reported in literature, but never all four of them in one work. *Buciuman et al.* and *Lopez de Mishima et al.* reported signals corresponding to those at 660 , 577 and 532 cm^{-1} .^[101,104] The group around *Gosztola* reported only two peaks, which correspond to the bands at 660 and 577 cm^{-1} .^[105] *Julien et al.* found corresponding signals for the features at 754 , 660 and 532 cm^{-1} , but found additional signals at 486 , 377 and 319 cm^{-1} .^[98] Interestingly, they conducted factor-group analysis, which predicted 4 Raman-active modes ($1A_{1g}+1B_{1g}+1B_{2g}+1E_g$) and does not fit their data. The number of signals presented here on the other hand agrees with the prediction of four modes. *Kapteijn et al.* and *Strohmeier and Hercules* reported $\beta\text{-MnO}_2$ to be Raman inactive.^[95,99]

All peaks measured for this sample could previously be attributed to different types of vibrations in literature. The strong modes at 660 and 532 cm^{-1} are indicative of the Rutile-type MnO_2 structure with interstitial space consisting of narrow one-dimensional (1×1) channels. They have been attributed to the stretching vibrations of Mn-O in MnO_6 octahedra.^[98,105] The other signals at 754 and 577 cm^{-1} have been

4. Phase identification of Mn oxides

assigned to the skeletal vibrations of the material, which are deformation modes of the Mn-O-Mn chains in the MnO₂ octahedral lattice.^[98,104] Thus, all present peaks are characteristic for β -MnO₂, although the most intense and most often reported peaks are the ones at 670-660 and 540-530 cm⁻¹, if a 532 nm laser is used, which is most often applied in literature.

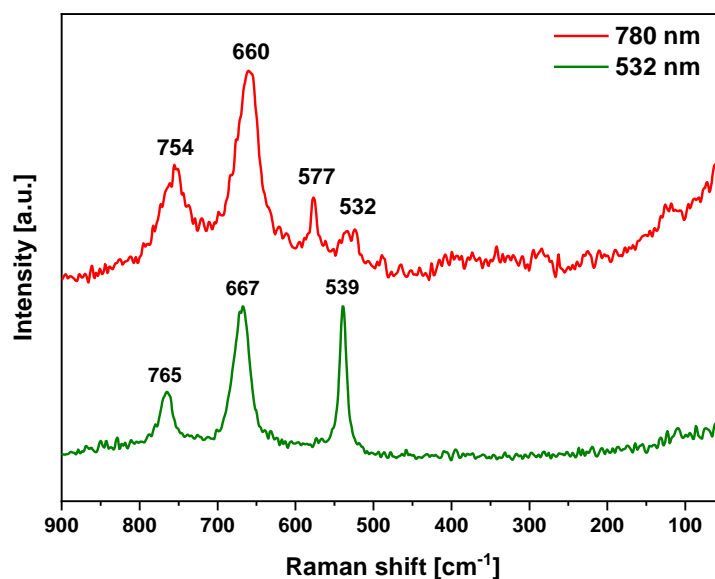


Figure 32: Raman spectrum of bulk β -MnO₂ measured using a 532 nm and a 780 nm laser.

In conclusion, Raman spectroscopy can be used to identify the composition of MnO_x samples and caution is advised when phases other than Mn₃O₄ are present, since even for the highly crystalline and most stable samples a transformation cannot be excluded. The lowest feasible laser powers should be applied while recording a spectrum to prevent sample alteration as much as possible. Figure 33 includes spectra of all high purity samples and the characteristic features which should be used for the phase identification are highlighted in red. Due to the easy distinction of Mn₃O₄ in Raman spectroscopy it is well suited for combined application with TPO experiments which identify all phases except the Hausmannite phase. Thus, combining all findings of these two methods yields a comprehensive picture of the composition of a MnO_x sample.

4. Phase identification of Mn oxides

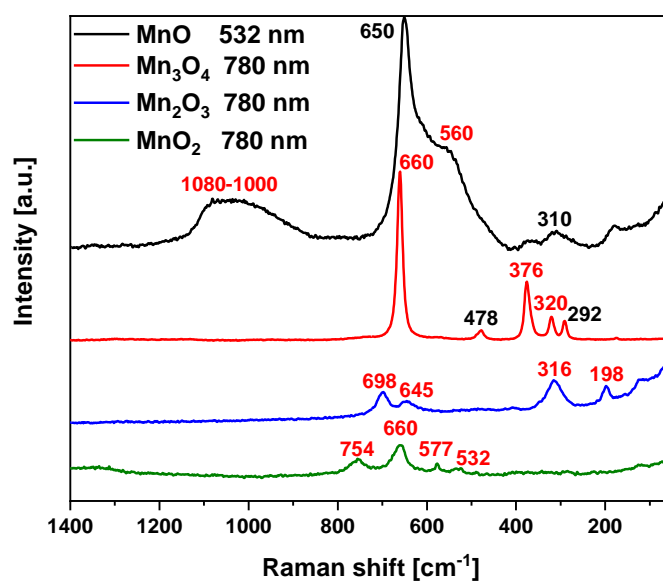


Figure 33: Raman spectra of all high purity MnO_x samples with characteristic features highlighted in red. The intensity of Mn₃O₄ has been scaled for better comparability of the data.

5. Catalysis of Mn oxides

5.1 Sample selection and characterization

For the second object of investigation, the elaboration of the behavior of the different MnO_x oxidation states in catalytic test reactions, a new batch of commercial samples had to be acquired to assure higher quantities of the same sample batch (≥ 100 g) and thus a consistent sample composition throughout all experiments conducted. Unfortunately, the samples which are available in higher quantities are of lower purity as well. For this reason, a phase analysis of the different samples by means of XRD, TPO and Raman spectroscopy has been made to check for impurities and gain further information on the samples which helps in attaining a deeper understanding of the results from catalytic benchmarking. All samples have been obtained in three different batches from different suppliers to ensure diversity.

The results of the XRD analysis of the MnO samples (Alfa Aesar, chemPUR and Sigma-Aldrich) can be seen in Figure 34. All samples exhibit a high crystallinity and no other crystalline phase than MnO is present in the samples.

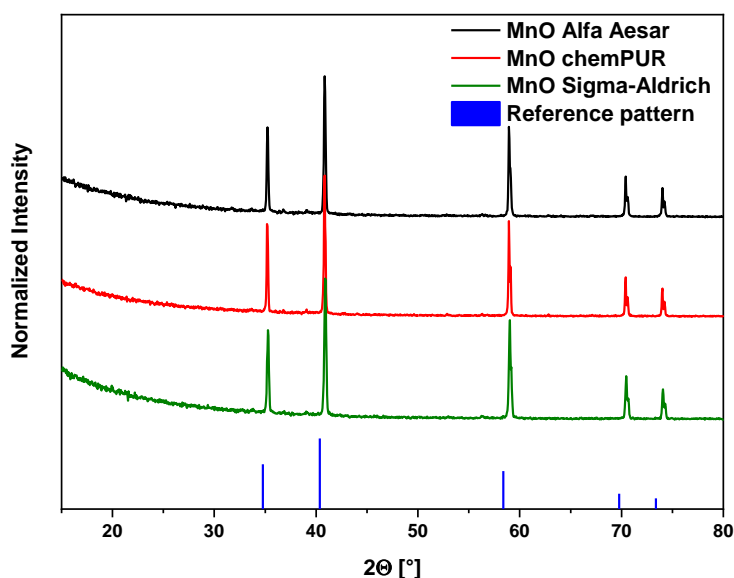


Figure 34: XRD patterns of the new sample batches of MnO and the reference line pattern of MnO.

5. Catalysis of Mn oxides

The TPO and Raman data (compare Figure 35) also do not show significant differences and match the high purity reference measurements. Thus, the MnO sample batches from all suppliers seem to be phase pure. The material from Sigma-Aldrich has been arbitrarily chosen as the sample for further studies and was further characterized and catalytically tested.

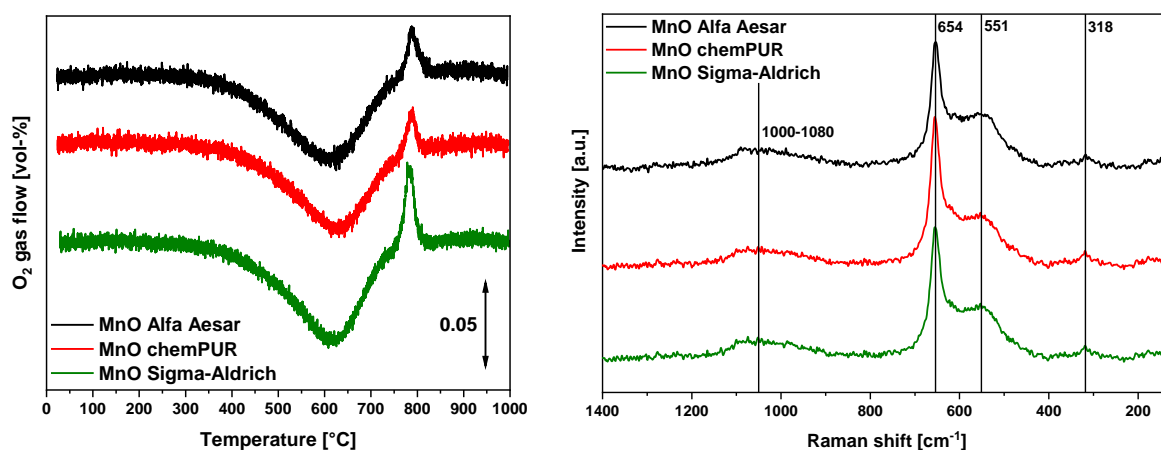


Figure 35: Left: TPO data of the new sample batches of MnO. The Y-axis was offset for better visibility. The baseline concentration was 1.1 vol-% O₂. Right: Raman spectra of the new sample batches of MnO.

As only two suppliers could be found who offered Mn₃O₄ in an acceptable purity and high quantities, one batch from Sigma-Aldrich and two different batches from abcr have been obtained instead to identify eventual differences in the sample batches. Comparing the results of the XRD analysis (shown in Figure 36), no major differences can be found, but the first batch of the abcr sample shows slightly broader reflexes than the other two samples, indicating a lower degree of crystallinity. The TPO results given in Figure 37 on the other hand reveal a significant difference between the three sample batches. The first batch from abcr exhibits huge amounts of Mn²⁺ and Mn³⁺ which are not present in the Hausmannite phase. The TPO data clearly shows impurities in the sample which are neither visible in the XRD nor in the Raman spectra and must therefore be of amorphous nature.

The other two samples exhibit a very small amount of Mn₂O₃ in the TPO indicated by the minimal high-temperature feature at 800 °C. The Raman spectra on the other hand do not differ for the presented samples and all of them show the typical Mn₃O₄ Hausmannite pattern which was discussed before. Due to the unfortunate experience

5. Catalysis of Mn oxides

with one of the abcr batches the Sigma-Aldrich sample has been chosen for further characterization and catalytic investigation.

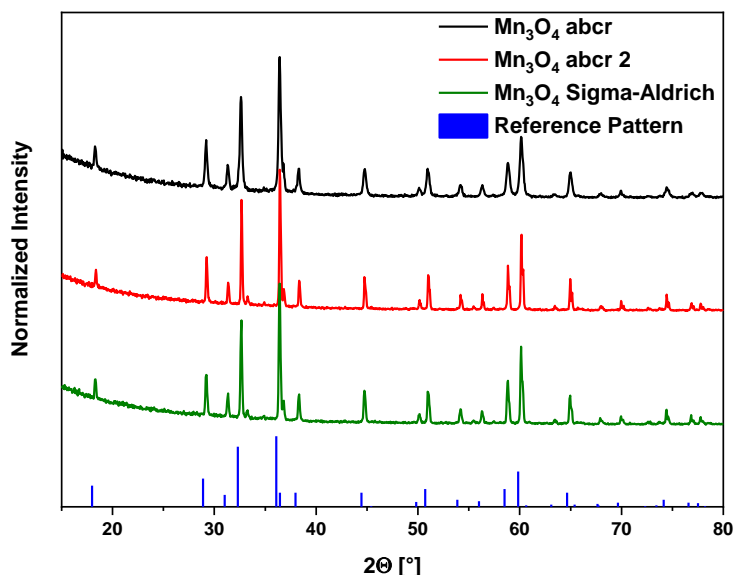


Figure 36: XRD patterns of the new sample batches of Mn₃O₄ and the reference line pattern of Mn₃O₄.

XRD analysis results of the three different batches of Mn₂O₃ (abcr, chemPUR and Sigma-Aldrich) can be seen in Figure 38. A difference can be found between the sample from abcr and the other two which on the other hand differ only slightly in reflex broadness. The Mn₂O₃ from abcr shows additional reflexes at 36.5, 44.8, 51.2 and 60.2° which cannot be found in any other sample and are also not present in the reference line spectra of Mn₂O₃ which indicates an additional crystalline impurity in the sample.

The comparison of the TPO data again yields insights into differences in the composition of the samples (Figure 39). It is apparent that all sample batches are mainly composed of Mn₂O₃ and exhibit a huge feature at 800 °C, but the abcr and Sigma-Aldrich samples also show a low-temperature thermal reduction event at 500 and 550 °C, respectively. This indicates small amounts of MnO₂ present in these two samples, whereas the chemPUR sample is free of these impurities and exhibits only the thermal reduction indicative for the Mn₂O₃ phase.

The measured Raman spectra do not include any differences and all samples show the representative spectrum of Mn₂O₃ which was also discussed previously.

5. Catalysis of Mn oxides

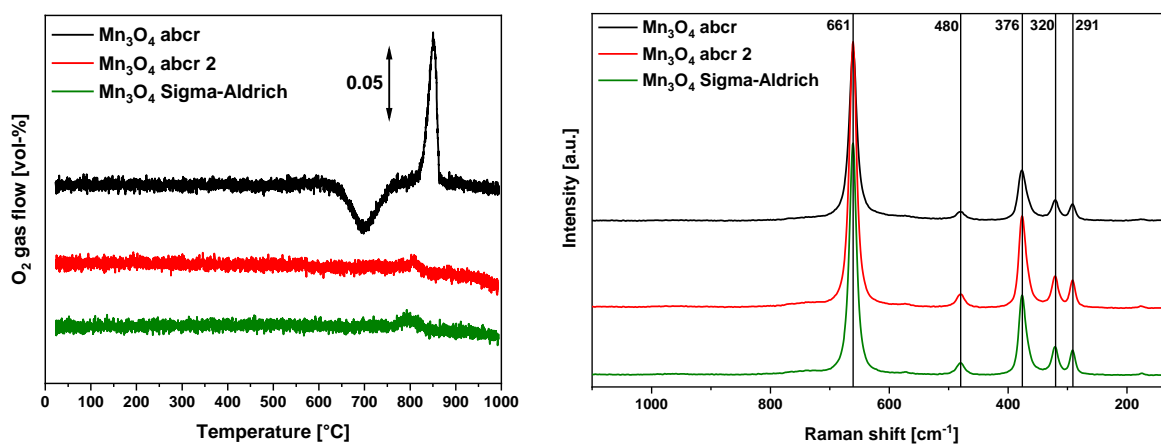


Figure 37: Left: TPO data of the new sample batches of Mn₃O₄. The Y-axis was offset for better visibility. The baseline concentration was 1.1 vol-% O₂. Right: Raman spectra of the new sample batches of Mn₃O₄.

Thus, the Mn₂O₃ from chemPUR was chosen for further characterization and catalytic testing because it did not exhibit any phase impurities in contrast to the other samples.

The XRD analysis of the three batches of MnO₂ (Alfa Aesar, chemPUR and Merck) illustrated in Figure 40 does not show any differences in the reflex positions and all samples match the reference line pattern in this regard.

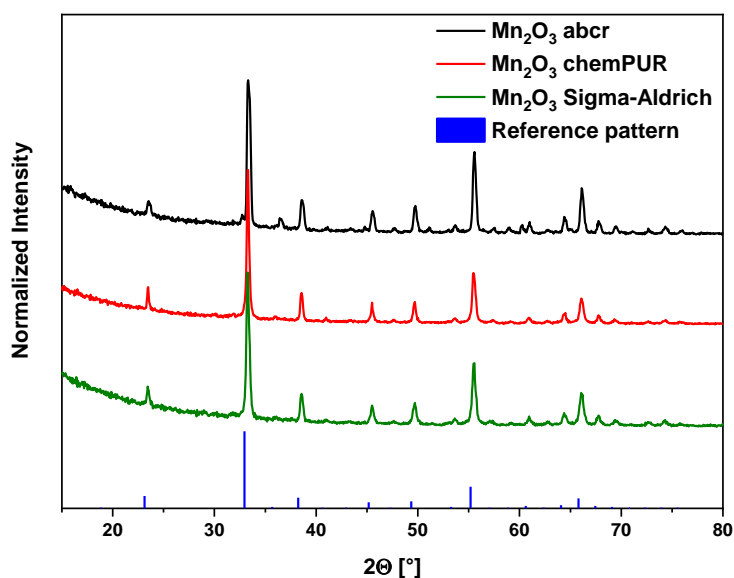


Figure 38: XRD patterns of the new sample batches of Mn₂O₃ and the reference line pattern of Mn₂O₃.

5. Catalysis of Mn oxides

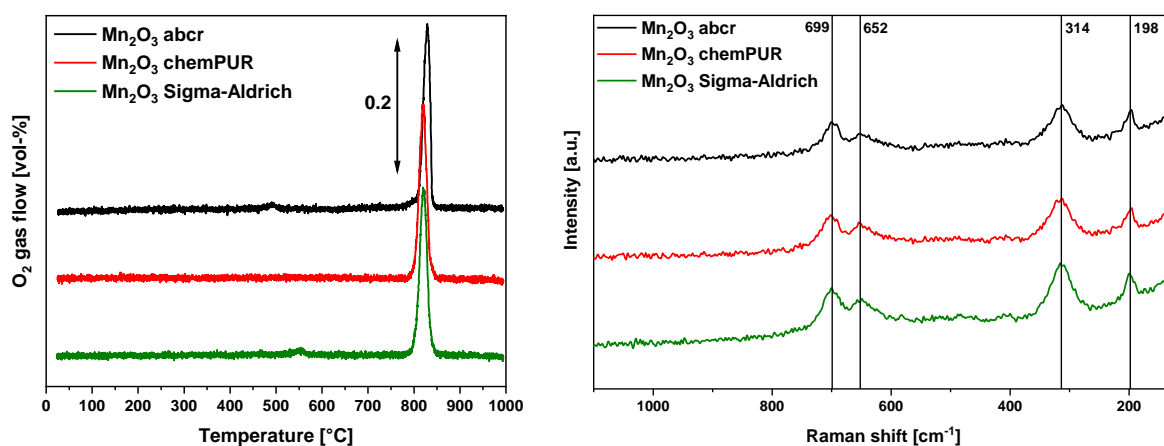


Figure 39: Left: TPO data of the new sample batches of Mn₂O₃. The Y-axis was offset for better visibility. The baseline concentration was 1.1 vol-% O₂. Right: Raman spectra of the new sample batches of Mn₂O₃.

Nevertheless, the sample from Merck does exhibit broader signals and the intensity ratios of the peaks do differ from the other samples and the reference line spectrum which indicates a different preferential order of the material.

The Merck sample shows strange behavior in the TPO experiment as well (compare Figure 41). The low temperature thermal reduction event of MnO₂ is shifted to higher temperatures by 50 °C and seems to be the overlap of two individual reduction events. Furthermore, the high temperature event is broadened and again shifted to higher temperatures by roughly 70 °C. The other two samples do not deviate from the reference measurement and behave as expected for phase pure MnO₂.

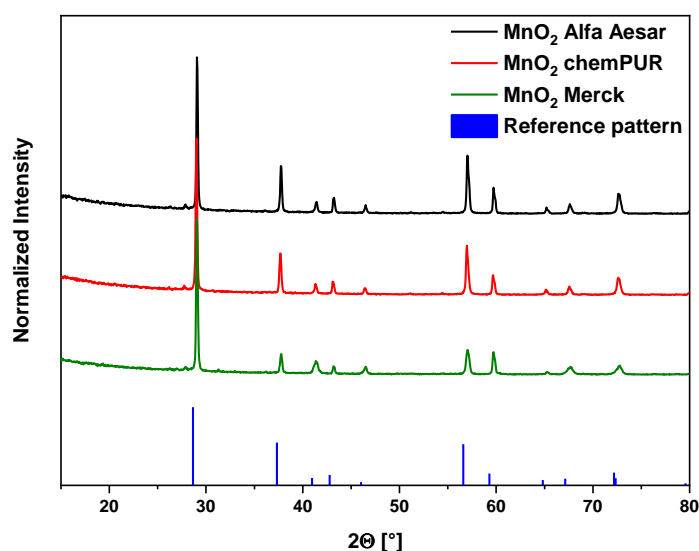


Figure 40: XRD patterns of the new sample batches of MnO₂ and the reference line pattern of MnO₂.

5. Catalysis of Mn oxides

The Raman measurements of the Alfa Aesar and chemPUR samples do not show any signs of impurities and give the expected reference pattern typical for measurements done with a 532 nm laser. The sample from Merck on the other hand exhibits additional Raman bands not commonly associated with MnO_2 measured with a 532 nm laser at 587, 397 and 186 cm^{-1} .

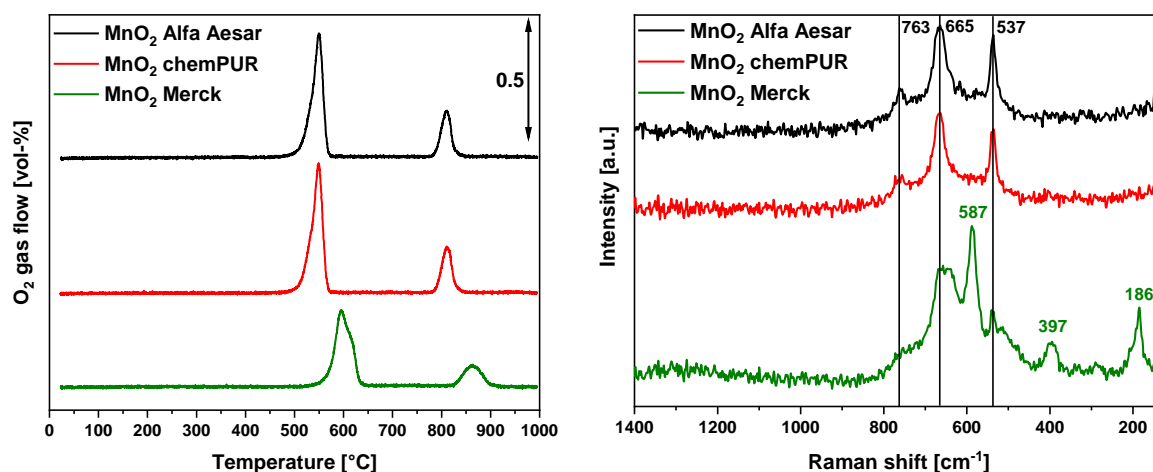


Figure 41: Left: TPO data of the new sample batches of MnO_2 . The Y-axis was offset for better visibility. The baseline concentration was 1.1 vol-% O_2 . Right: Raman spectra of the new sample batches of MnO_2 .

All these findings prove a phase impurity in the Merck sample, although it is not clear whether it is a completely different substance or maybe a slightly different structure of MnO_2 . Nevertheless, the other two samples seem to be of higher purity, and both would be suitable for further investigations. Thus, the sample from chemPUR was again arbitrarily chosen for the following experiments and together with the other chosen samples further characterized by means of fitting the respective data by the method after Rietveld (Figure 42).

The Rietveld analysis revealed all samples to be phase pure except for Mn_2O_3 which was found to contain trace amounts of Mn_3O_4 in a range of 1.2%. From this Fit lattice parameters, the strain of the system ϵ_0 and domain sizes L_{V0-IB} could be extracted and are given in Table 7.

5. Catalysis of Mn oxides

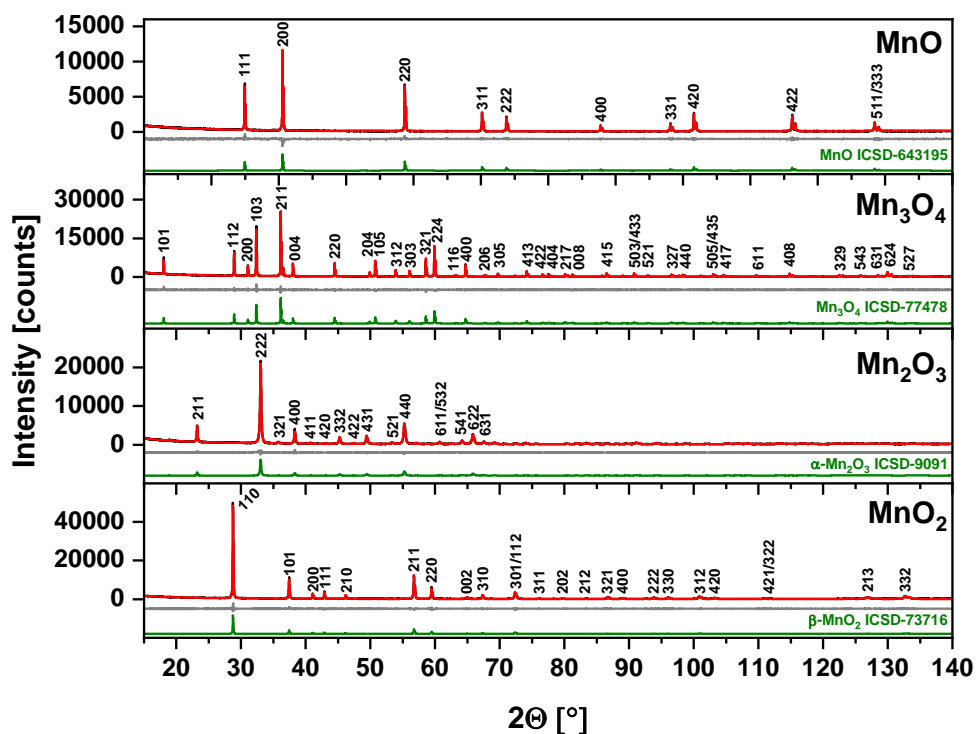


Figure 42: Results of the XRD analysis depicting the measured XRD pattern (black), the fitted data after the method of Rietveld (red), the difference between those two (grey) and the reference pattern from ICSD (green). Additionally, the Laue indices are given above the individual reflexes.

The surface area of a sample is of major importance for a catalytic reaction and was therefore determined for all samples in the highest accuracy possible. To this end, the standard procedure for a N_2 physisorption experiment was initially used and the analysis according to *Brunauer, Emmett and Teller* applied. All BET results discussed here are summarized in Table 8.

Table 7: Refined lattice parameters, domain sizes and microstrain (with estimated standard deviations) obtained from the Rietveld fits.

	MnO	Mn ₃ O ₄	Mn ₂ O ₃	MnO ₂
Space group	<i>Fm-3m</i>	<i>I4₁/amd</i>	<i>Ia-3</i>	<i>P4₂/mnm</i>
Crystal system	cubic	tetragonal	cubic	tetragonal
a [Å]	4.4450(1)	5.7616(1)	9.4122(1)	4.3987(1)
c [Å]		9.4676(1)		2.8731(1)
L_{Vol-IB} [nm]	124(2)	239(3)	133(6)	319(15)
ε₀	-	0.000059(2)	0.000684(11)	0.000286(5)

5. Catalysis of Mn oxides

The specific surface areas S_{BET} of all samples are very small (ranging from 0.38 to 2.88 m²/g) and N₂ is not best suited to reliably measure surface areas below 1 m²/g. Thus, a krypton physisorption experiment has been conducted in addition to the standard N₂ procedure to verify the results and gain more precise values for the measured surface areas.

For the MnO and MnO₂ samples both measurements give results which are in very good agreement and even for the other two samples the differences are not significantly large (roughly 10%). But as expected the krypton BET measurement does give a systematically smaller specific surface area for the diverging samples, since it is better suited to measure these small surface areas.

Additionally, a theoretical specific surface area S_{XRD} was calculated from the domain sizes found in the Rietveld analysis of the XRD data. For these calculations the materials were approximated to consist only of domains of the given size and all domains were assumed to be spherical. The areas calculated in this way are all bigger than the measured surface areas, but except for MnO this crude approximation gives results within the same order of magnitude.

In conclusion, a new sample set was chosen for the catalytic test reactions, and a thorough phase analysis was applied to ensure high purity of the samples. Furthermore, the combination of XRD, TPO and Raman spectroscopy was shown to give a comprehensive picture of the phase composition of a sample. In the end, multiple physisorption techniques have been applied to the chosen set of samples to accurately determine the surface area for the subsequent catalytical investigations.

Table 8: Specific surface area measured by N₂ and Krypton BET for the selected MnO_x samples.

	MnO	Mn₃O₄	Mn₂O₃	MnO₂
S_{BET, N₂} [m²/g]	0.38	0.92	2.88	2.03
S_{BET, Kr} [m²/g]	0.38	0.79	2.61	2.06
S_{XRD} [m²/g]	8.8±0.5	5.2±0.2	10.0±1.6	3.7±0.7

5.2 CO oxidation over MnO_x

For the first catalytic test reaction giving insights into the oxidation behavior of the binary manganese oxides, CO oxidation was selected due to the model nature of this reaction and the high amount of reference literature which can be found for a huge variety of catalytic systems. To gain a first overview over the sample behavior the conversion of CO to CO_2 was measured over a heating ramp of 10 K/min. The results are shown in Figure 43. MnO and MnO_2 do not show the expected S-shaped curve but instead give rise to a line shape which resembles a two-phase sample mixture. This behavior can be explained by a transformation of these samples analogously to the one found in the TPO experiments. The transformation of MnO starts at roughly 400 °C which is identical to the onset observed during the TPO experiment. MnO_2 on the other hand has a much earlier onset at roughly 250 °C which stands in contrast to the findings in TPO which exhibit a thermal reduction onset at roughly 500 °C. The explanation for this phenomenon can be found in the addition of reducing CO to the inlet feed of the reactor.

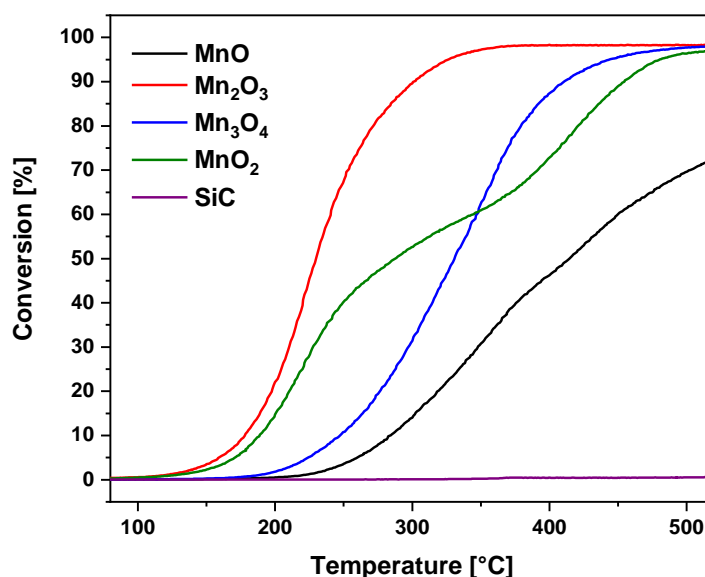


Figure 43: CO conversion of all MnO_x samples and inert SiC during a heating ramp of 10 K/min.

The MnO sample cannot be reduced further under the given conditions and thus only the O_2 present influences the reaction onset of the sample, whereas the MnO_2 is

5. Catalysis of Mn oxides

thermally reduced under slightly oxidizing conditions and thus the CO accelerates the reduction. Thus, only the initial degrees of conversion (temperatures < 250 °C) can give insight into the intrinsic oxidation behavior of the investigated samples. In this region a clear reactivity sequence can be found which is as follows: $\text{Mn}_2\text{O}_3 > \text{MnO}_2 > \text{Mn}_3\text{O}_4 > \text{MnO}$. The same sequence can also be found if the rate of CO_2 formation is normalized to the Krypton BET specific surface area (Figure 44). Although all samples exhibit very small surface areas, this normalization is imperative for a meaningful comparison of the results. The samples with the smallest surface area (MnO with $0.38 \text{ m}^2/\text{g}$) and the largest (Mn_2O_3 with $2.61 \text{ m}^2/\text{g}$) are almost one order of magnitude apart, which should also give an order of magnitude difference for the numbers of active sites and thus for the reaction rates observed. The normalization should correct of this deviation and give a more reliable comparison of the intrinsic activity of the individual materials. The fact that the sequence did not change after normalization proves the Mn(III) and Mn(IV) oxides to have a higher intrinsic activity in CO oxidation than the Mn(II) and Mn(II, III) oxides and shows this to not merely be an effect of the differing surface areas.

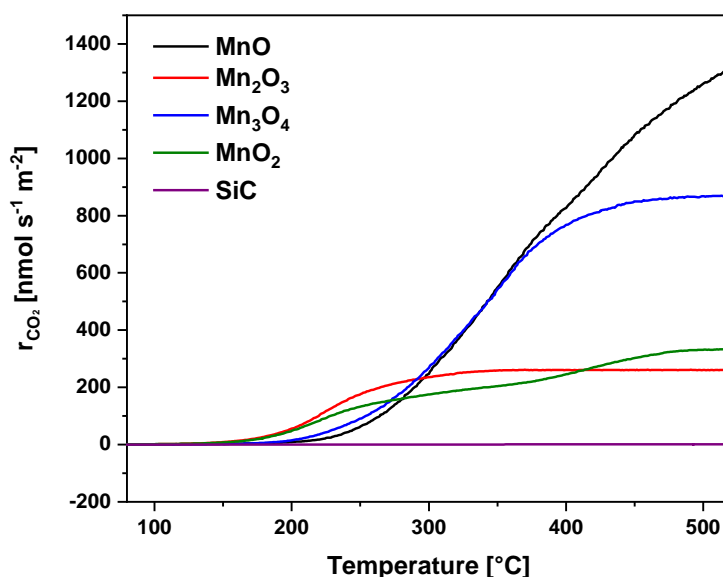


Figure 44: Rate of CO_2 formation normalized to the Krypton BET specific surface area for all MnO_x samples and SiC.

5. Catalysis of Mn oxides

At high temperatures the normalized formation rates are dominated by full conversion and thus the formation rate is inversely proportional to the specific surface area of the material. These trends do not yield significant information on the catalytic performance of the samples.

For a deeper insight into the catalytic processes of all thermodynamically stable MnO_x a series of experiments with isothermal steps was performed. Four temperatures between 1% and 10% conversion have been held until steady state conditions were reached, and the respective CO_2 formation rates were measured. This data was then used to construct an Arrhenius plot following equation (6). The results for all samples are illustrated in Figure 45 and the data is additionally compiled in Table 9.

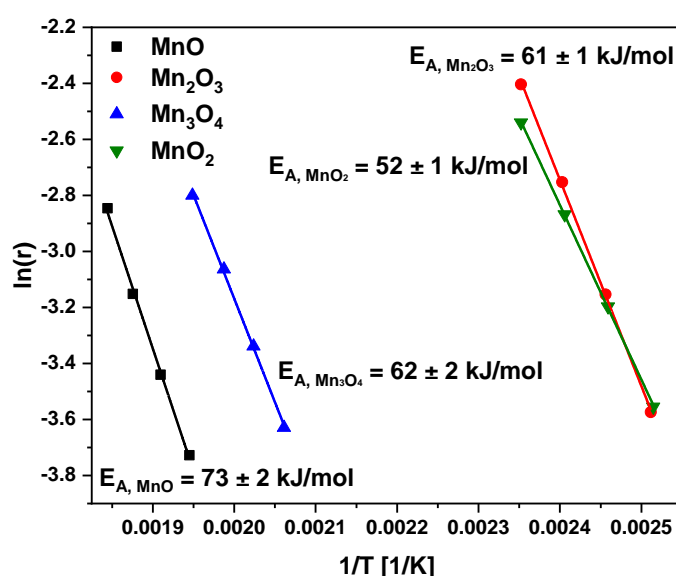


Figure 45: Arrhenius plots for all MnO_x samples and the respective apparent activation energies in the CO oxidation.

The apparent activation energies do not follow the same reactivity sequence as initially found for the reaction rates during the heating ramp. The MnO_2 sample has a lower apparent activation energy than Mn_2O_3 . Furthermore, the E_A of Mn_3O_4 is roughly the same as for Mn_2O_3 . The sequence of apparent activation energies in the CO oxidation is as follows: $\text{MnO}_2 < \text{Mn}_2\text{O}_3 \approx \text{Mn}_3\text{O}_4 < \text{MnO}$. Nevertheless, if the different redox pairs are considered the same conclusion as before might be drawn.

5. Catalysis of Mn oxides

The Mn(III)/Mn(IV) redox couple exhibits a higher activity towards the CO oxidation than the Mn(II)/Mn(III) couple. This assumption is in accordance with literature, where Mn(III) is often found to have highest activity and the combination of Mn(III) and Mn(IV) is reported to be even more beneficial for oxidation catalysis.^[85–88]

Additionally, the O₂ and CO reaction orders in the CO oxidation have been determined in an isothermal concentration variation study for all samples. The evaluation has been done according to equation (8) and the results are shown in Figure 46 and Figure 47 for O₂ and CO, respectively. All numerical values of the isothermal experiments are also compiled in Table 9.

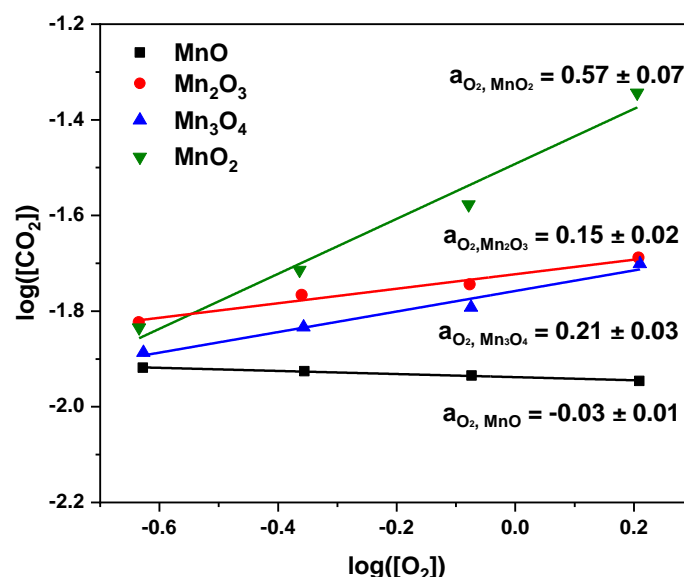


Figure 46: Determination of the O₂ reaction orders for all MnO_x samples in the CO oxidation.

The oxygen and carbon monoxide reaction orders vary strongly for the different samples ranging from roughly 0 to 0.6 and from 0.2 to 0.8, respectively. The different reaction orders show an inversely proportional behavior over the complete set of samples. Thus, a connection of the reaction orders to the adsorption behavior seems likely with a competitive adsorption being present. The CO and O₂ might use similar adsorption sites but feature different adsorption strengths which vary for the individual samples and thus give rise to the dependence between the two reaction orders. Furthermore, higher reactivity was observed for samples, which have intermediate reaction orders for both reactants, whereas the samples featuring very

5. Catalysis of Mn oxides

high CO reaction orders did not exhibit high activities. Thus, the conclusion that the surface of MnO is saturated with oxygen which poisons the CO adsorption can be drawn. A similar behavior although less pronounced can be assumed for Mn₃O₄. The most active compounds Mn₂O₃ and MnO₂ might have intermittent surface coverage degrees of both reactants which is most beneficial for the reaction and explains the higher activity of these samples.

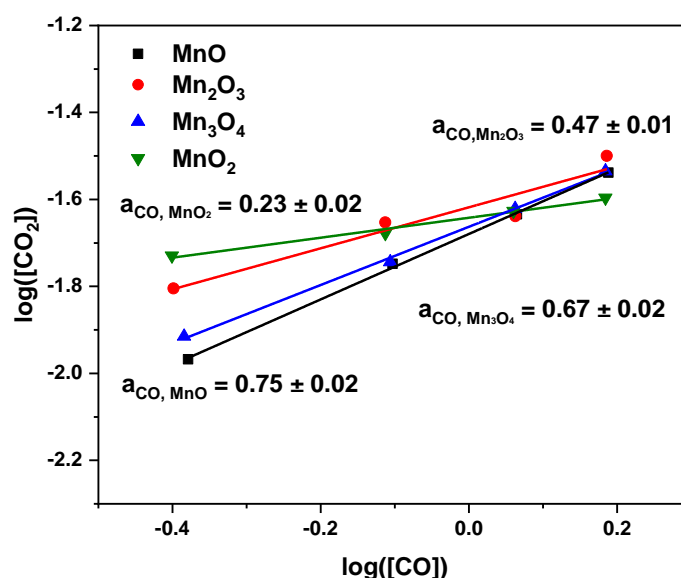


Figure 47: Determination of the CO reaction orders for all MnO_x samples in the CO oxidation.

In conclusion a Langmuir-Hinshelwood reaction mechanism seems plausible where the adsorption of the reactants is rate determining and too high surface coverages poison the catalyst surface leading to lower observed activities.

Table 10 lists activation energies and reaction orders for different metal oxide systems from literature. Comparing these results to the present data of the MnO_x samples reveals a comparably low activation energy of the Manganese oxides. Only nanoengineered CoO_x has lower activation energies than presented here and especially the MnO₂ sample ranges with the systems of lowest E_A values. The reaction orders of CO spread over a broad range (0.12 to 1.2) which is also in alignment with the data presented here and the most oxide systems show reaction orders in the range of 0.4 to 0.7 which is true for a multitude of the binary MnO_x samples as well. The O₂ reaction order on the other hand most commonly ranges

5. Catalysis of Mn oxides

from 0 to 0.3 which is also in agreement with the data presented here. The sole exception being MnO_2 which has the highest O_2 reaction order of all samples presented here but has been measured in literature as well and is in perfect agreement with the data presented in this study.

Table 9: Compiled apparent activation energies E_A and reaction orders a for all MnO_x samples in the CO oxidation.

	MnO	Mn₃O₄	Mn₂O₃	MnO₂
E_A [kJ/mol]	73 ± 2	62 ± 2	61 ± 1	52 ± 1
$a(\text{CO})$	0.75 ± 0.02	0.67 ± 0.02	0.47 ± 0.01	0.23 ± 0.02
$a(\text{O}_2)$	-0.03 ± 0.01	0.21 ± 0.03	0.15 ± 0.02	0.57 ± 0.07

5. Catalysis of Mn oxides

Table 10: Apparent activation energies E_A and reaction orders a in the CO oxidation for a variety of non-supported metal oxide materials from literature.

Sample	E_a kJ/mol	$a(\text{CO})$	$a(\text{O}_2)$	Reference
Ba ₂ Cu ₃ O ₅	165 ± 10	0.3 ± 0.1	0.3 ± 0.1	[106]
BaCoO ₃	50	0.4	0.3	[107]
BaCuO ₂	63 ± 5	1.2	0 ± 0.1	[106]
CeO ₂	123 ± 4	-	-	[108]
CeO ₂ sheets	89 ± 3	-	-	[108]
Co ₃ O ₄	79 ± 8	-	-	[109]
Co ₃ O ₄	84 ± 8	0.45 ± 0.1	0.46 ± 0.12	[110]
Co ₃ O ₄ nanorods	22	0.12	0.28	[111]
CoO _{1.00} NPs	38 ± 3	1	-	[112]
CoO _{1.07} NPs	30 ± 2	1	-	[112]
CoO _{1.21} NPs	24 ± 2	1	-	[112]
CoO _{1.33} NPs	18 ± 0	1	-	[112]
Cr ₂ O ₃	64	0.7	0.4	[107,113]
Cr ₂ O ₃ flux growth	49	0.9	-0.3	[107,113]
Cu _{0.8} Co _{2.2} O ₄	106	-	-	[114]
Cu ₂ O	58 ± 2	-	-	[115]
Cu ₂ O	48 ± 8	-	-	[116]
CuCr ₂ O ₄	96	0.7	0	[107]
CuCr ₂ O ₄	104	-	-	[114]
CuO	47 ± 4	-	-	[115]
CuO	92	0.7	0	[107]
Fe ₂ O ₃	71	0.9 - 1.1	0.3 - 0	[107]
Fe ₂ O ₃	110	-	-	[117]
FeCr ₂ O ₄	63	0.7	0	[107]
LaCoO ₂	59 ± 8	-	-	[109]
LaCoO ₃	79	0.6	0.3	[107]
LaMnO ₃	50	0.7	0	[107]
MnO ₂	54	0.2	0.6	[107]
MoO ₃	116.6	1	0	[118]
NiO (<220 °C)	63	0.55	0.47	[107,119]
NiO (>220 °C)	105	0.55	0.47	[107,119]
NiO (100-180 °C)	9	-	-	[120]
NiO (180-240 °C)	54	-	-	[120]
SnO ₂	59	0.55	0	[107]
ZnCr ₂ O ₄	78	-	-	[114]
ZrO ₂	71	0.6	0.2	[107]

5.3 2-propanol oxidation over MnO_x

The oxidation of 2-propanol is the second reaction in which the bulk Mn oxides were tested for their activity in oxidation catalysis. Contrary to the CO oxidation, where the total combustion to CO_2 was the only feasible reaction pathway, in this case different pathways are possible and product selectivity becomes an additional factor to be considered.

As before, the dependence of the conversion and selectivity on the temperature has been tested first during an experiment with a constant heating rate. The samples yielded only two products over the tested temperature window which are acetone and CO_2 (compare Figure 48). Furthermore, the formation of CO_2 starts only at elevated temperatures ($> 230\text{ }^\circ\text{C}$). Below this temperature all samples exhibit a selectivity of 100% towards acetone.

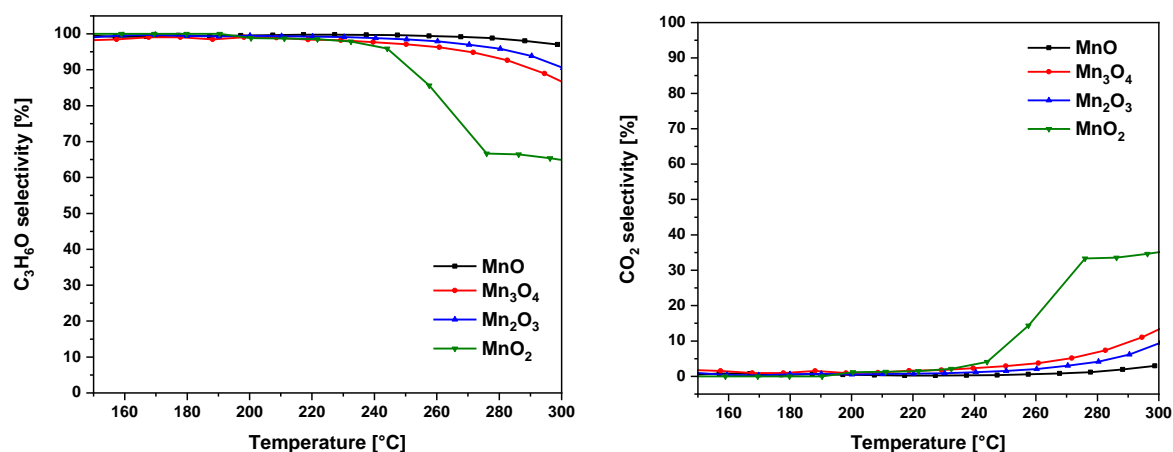


Figure 48: Product selectivities towards acetone (left) and CO_2 (right) as a function of the temperature in the 2-propanol oxidation for all MnO_x samples.

The CO_2 formation tendency in the tested temperature regime is small for all samples except MnO_2 which shows up to 40% selectivity towards the formation of CO_2 at temperatures $> 280\text{ }^\circ\text{C}$.

Looking at the conversion (shown in Figure 49) of the samples over the course of the heating experiment reveals a different reactivity pattern than observed in the CO oxidation. Up to temperatures of $230\text{ }^\circ\text{C}$ the MnO shows the highest conversion with

5. Catalysis of Mn oxides

a 100% selectivity towards acetone. This is even more pronounced when looking at the rate of acetone formation normalized to the Krypton BET surface area, since this sample offers the smallest amount of surface for the reaction to occur. At temperatures > 230 °C the MnO_2 sample shows higher conversion which can be attributed to the formation of CO_2 in big amounts changing the reaction pathway from selective oxidation to total combustion of 2-propanol.

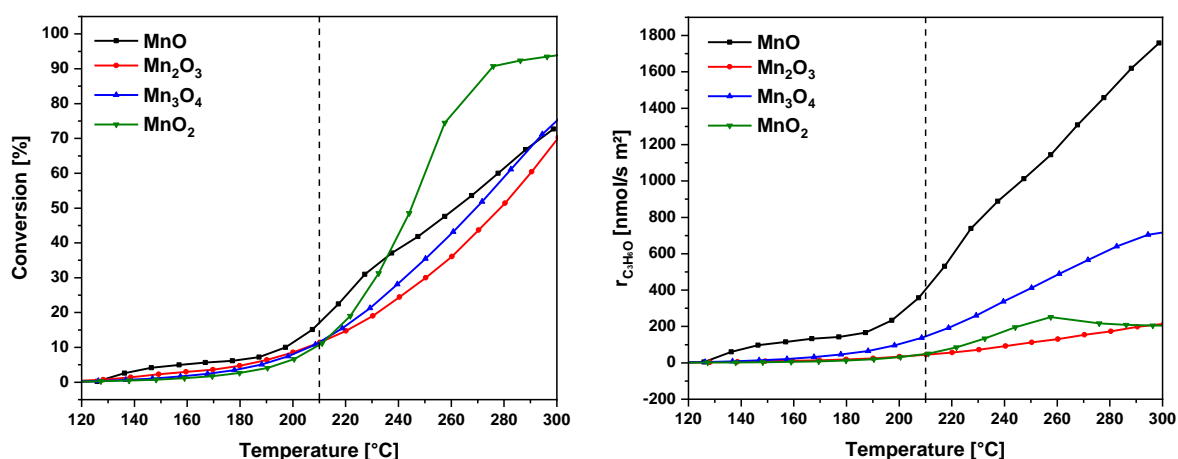


Figure 49: Conversion (left) and acetone formation rate normalized to the Krypton BET surface area (right) during a heating ramp in the oxidation reaction of 2-propanol for all MnO_x samples.

The normalized acetone formation rates clearly show the activity sequence of the different samples towards acetone formation as follows: $\text{MnO} > \text{Mn}_3\text{O}_4 > \text{MnO}_2 > \text{Mn}_2\text{O}_3$. In this case the lower valent oxides are performing better in the formation of acetone, whereas the higher valent oxides are more reactive in the total combustion of 2-propanol.

To gain further insights into the reaction mechanism of the present samples towards acetone, the oxygen was removed from the feed in an isothermal experiment and the response of the acetone formation was observed (illustrated in Figure 50). The acetone formation of the lower valent samples MnO and Mn_3O_4 initially decreases to zero after oxygen removal from the reaction feed. However, the formation increases again only to cease afterwards. This could indicate residual oxygen stored in the samples which is slowly consumed for further reaction until completely depleted. Afterwards the acetone formation of the MnO sample completely stops, whereas the Mn_3O_4 is the only sample where a slight acetone formation starts again after oxygen

5. Catalysis of Mn oxides

depletion. However, the amount of acetone formed in oxygen-free atmosphere is minimal and takes 10 h on stream to become distinguishable from the baseline. It needs to be noted that a small residual amount of acetone is visible for all samples (roughly 0.01 vol-%) which originates from the saturator where acetone is formed during the time on stream from the 2-propanol. The other two samples Mn_2O_3 and MnO_2 do not exhibit any delayed acetone release and the formation slowly ceases after oxygen is removed from the feed. Both samples do not show any further reaction without oxygen. Furthermore, none of the samples showed any additional products under exclusion of oxygen from the reaction. It was especially ensured no propylene formation was present during this experiment.

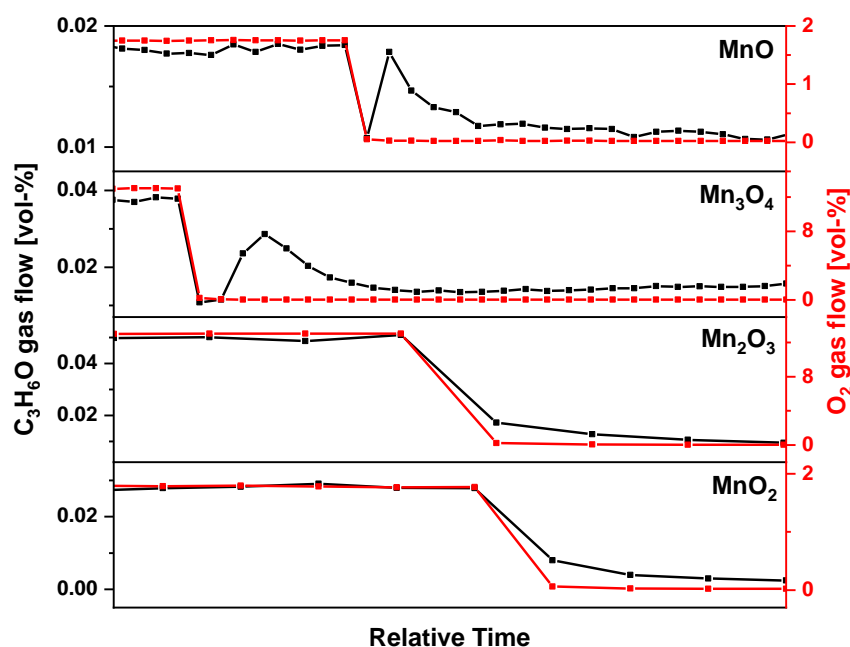


Figure 50: Acetone formation during the removal of oxygen from the reaction feed in the 2-propanol oxidation for all MnO_x samples. The time between two measurements is 45 min for all samples.

Thus, the formation of acetone is an oxygen driven oxidation reaction on all samples. It is likely, that the continuous formation of small amounts of acetone without dosed oxygen on Mn_3O_4 results from a dehydrogenation of 2-propanol in an acid-base catalyzed reaction on basic sites which has been previously reported for other systems.

5. Catalysis of Mn oxides

Isothermal experiments for the determination of the apparent activation energy and the reaction orders of 2-propanol and oxygen have been conducted analogously to the CO oxidation in a range of 1 to 10% conversion. All Arrhenius plots for the determination of E_A are visible in Figure 51 and the numerical values of the apparent activation energies and all reaction orders are additionally compiled in Table 11.

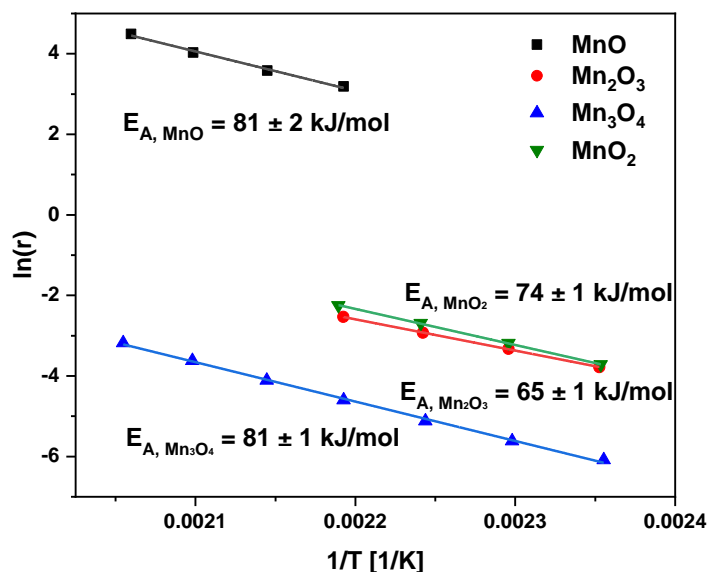


Figure 51: Arrhenius plots for all MnO_x samples and the respective apparent activation energies in the 2-propanol oxidation.

The apparent activation energies suggest a different reactivity pattern than observed in the conversion over temperature experiments. The sequence of apparent activation energies found in the Arrhenius analysis is: Mn₂O₃ < MnO₂ < Mn₃O₄ = MnO. Thus, the expected activity of the samples is inversed from what was previously found. This might be due to the integral nature of the apparent activation energy. All possible reaction pathways and the activation energies of every single reaction step are compounded into one numerical value. Since multiple reaction pathways are possible the value indicates the one with the lowest barrier and this might be the total combustion which is favored at higher temperatures. The selective oxidation of 2-propanol to acetone on the other hand is the reaction which is mostly present in the low temperature range. This might be a reason for the trends shown by the apparent activation energies and the actual

5. Catalysis of Mn oxides

conversion of the samples to strongly differ. Alternatively, the transition states on the different catalysts might be bound in different ways giving rise to a differing number of degrees of freedom which has a big influence on the preexponential factor of the Arrhenius equation. Thus, explaining the differences between activation energies and observed reactivity (a measure of k).

The determination of the 2-propanol and oxygen reaction orders for all MnO_x samples can be seen in Figure 52 and Figure 53, respectively. The reaction orders for both reactants do not spread very far apart and all values are in proximity of one another.

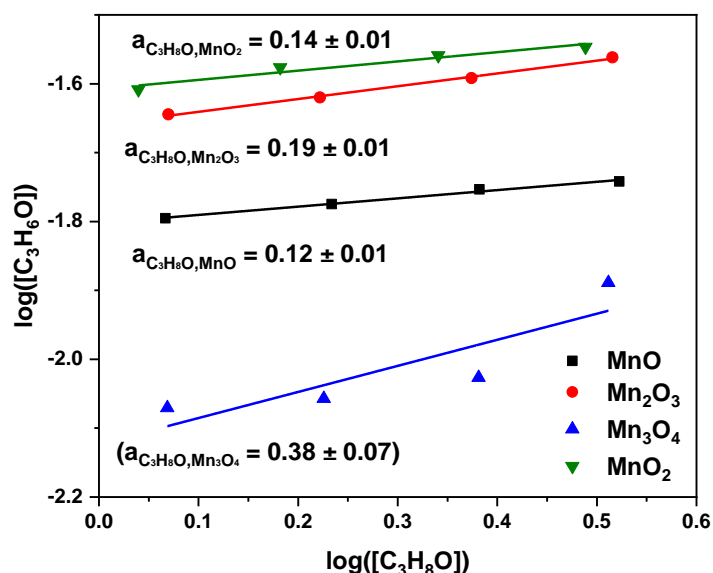


Figure 52: Determination of the 2-propanol reaction orders for all MnO_x samples in the 2-propanol oxidation.

The 2-propanol reaction orders range from 0.12 to 0.19 for MnO , Mn_2O_3 and MnO_2 while a stronger divergence can be found for Mn_3O_4 with 0.38. Unfortunately, this last value is not very reliable, since no satisfying linear dependence could be found for this experiment. This might be due to too low conversions and too much acetone formation in the saturator during the prolonged experiment, which makes the distinction of acetone formation from the baseline acetone present in the feed not feasible. The determination of the O_2 reaction orders on the other hand does yield nice linear dependences for all samples and the values range from 0.20 to 0.31. No clear correlation between the two reaction orders can be found for this reaction and

5. Catalysis of Mn oxides

due to the close numerical proximity, it can be assumed that no competitive adsorption is present.

If the samples indeed do not feature competitive adsorption and the two reactants are both present on the surfaces of all catalysts in similar amounts, the differences observed in the reactivity might originate from different catalytic pathways rather than differing adsorption behavior. This hypothesis is further encouraged when the oxygen storage capacities of the samples are considered. The lower valent samples seemed to store oxygen which was still available for the oxidation of 2-propanol after oxygen was no longer present in the feed. Thus, a limitation of the reaction speed due to oxygen adsorption seems implausible if enough is present to store it in the sample. These findings might even indicate a Mars-van-Krevelen type reaction mechanism for the lower valent samples, although the present data is not sufficient to prove or disprove this idea in any way.

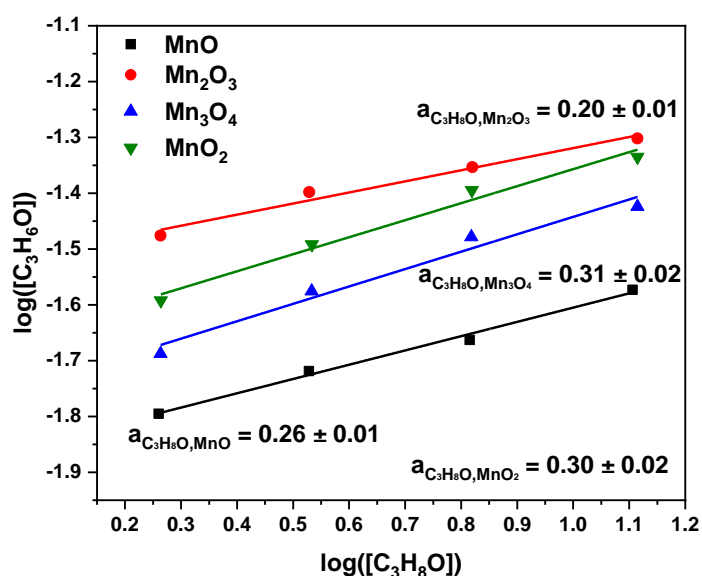


Figure 53: Determination of the O_2 reaction orders for all MnO_x samples in the 2-propanol oxidation.

To gain insight into the phase composition of the samples after catalysis they were run under steady state conditions for 16 h (Figure 54) and were afterwards characterized by means of TPO (Figure 55) and XRD (Figure 56).

5. Catalysis of Mn oxides

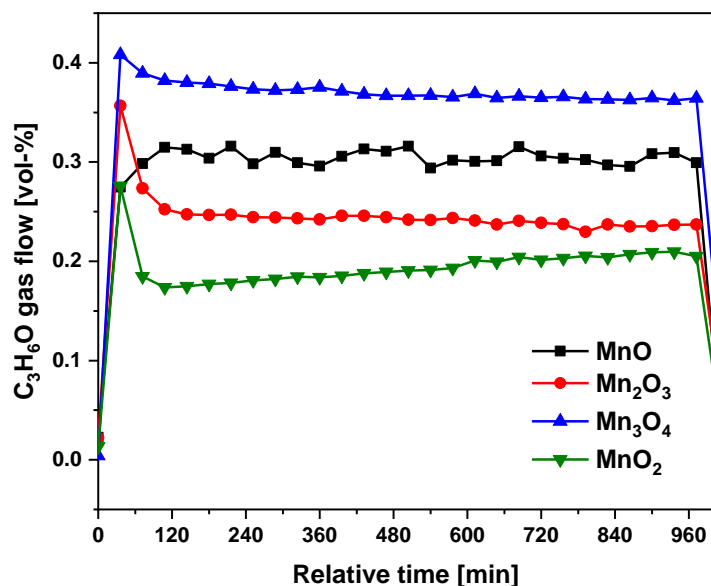


Figure 54: Acetone evolution during the 16 h of steady state conditions for all MnO_x samples in the 2-propanol oxidation.

The performance of all samples is stable over the course of 16 h of steady state catalysis except for MnO₂ which is steadily increasing in activity. MnO₂ is also the only sample which shows actual change in the sample composition after catalysis. TPO shows an additional phase which does not belong to any of the investigated binary oxides and the fitted XRD data reveals this phase to be MnOOH. The amount of the new phase is in the range of 10.9%.

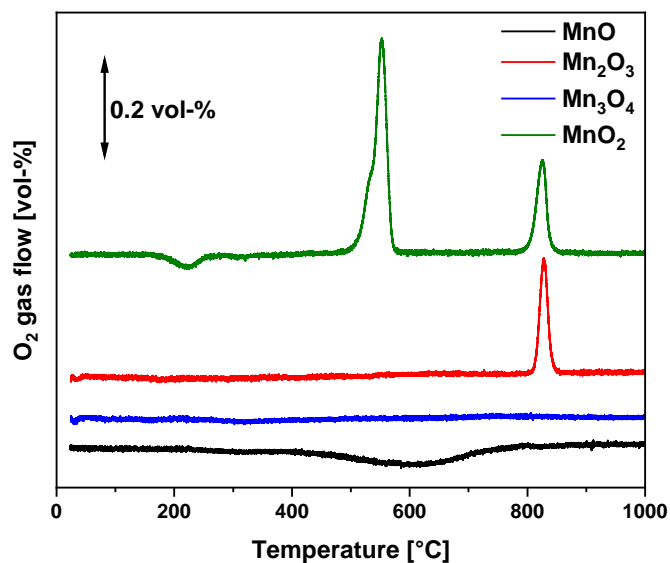


Figure 55: TPO analysis for the post-mortem samples after 16 h of steady state conditions. The Y-axis is offset for better visibility. The baseline of all samples is 1.0 vol-% of O₂.

5. Catalysis of Mn oxides

Thus, the activation process of the sample can be attributed to the formation of the new MnOOH phase during catalysis. The TPO and XRD data of the other samples reveal no bulk changes in the sample compositions. The only notable deviation from the bulk measurements can be found for the MnO sample, where reaction stopped after the oxidation to the Mn₂O₃ phase without further thermal reduction to Mn₃O₄ which was always observed for the bulk sample. Nevertheless, the XRD exhibits only MnO which indicates phase purity of the bulk structure.

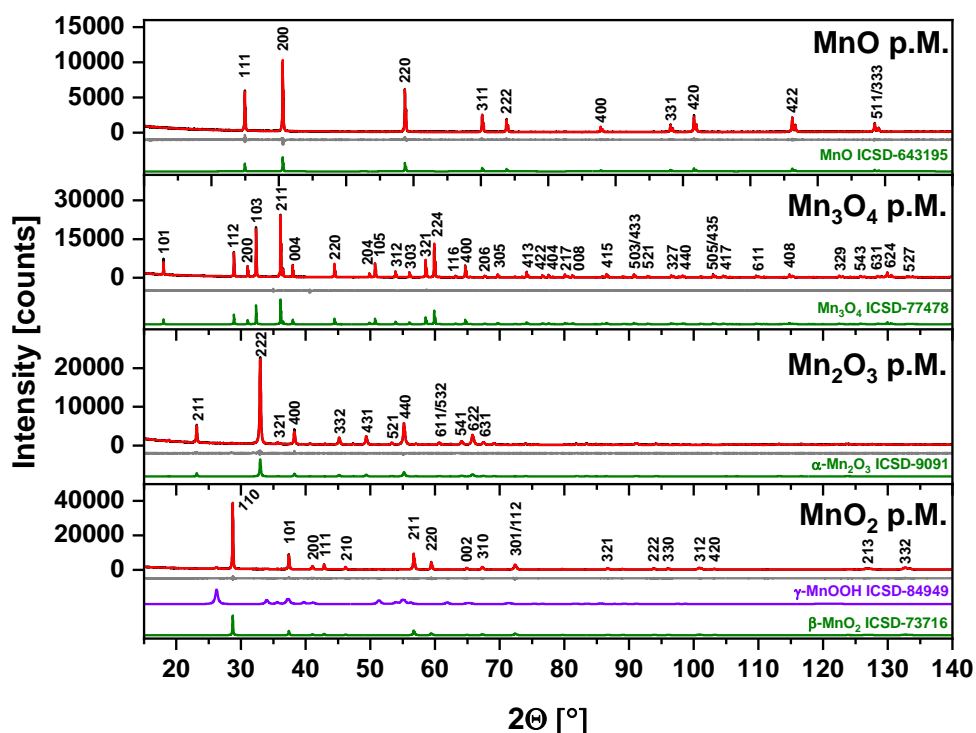


Figure 56: Results of the XRD analysis after catalysis depicting the measured XRD pattern (black), the fitted data after the method of Rietveld (red), the difference between those two (grey) and the reference pattern from ICSD (green and violet). Additionally, the Laue indices are given above the individual reflexes.

In conclusion, the 2-propanol oxidation over bulk MnO_x catalysts has a high selectivity at low temperatures towards acetone which shifts towards CO₂ with higher temperatures and especially for the higher valent oxides. A higher acetone formation rate could be observed for the low valent Mn oxides in the selective oxidation of 2-propanol, whereas the higher valent samples featured higher CO₂ formation rates in the total combustion reaction. Furthermore, an oxygen storage behavior of low valent oxides was assumed, and mechanistic insights could be gained from the

5. Catalysis of Mn oxides

determination of the reaction orders of 2-propanol and oxygen, which gave rise to a number of distinct mechanistic hypotheses that can be investigated in more detail in the future.

Table 11: Compiled apparent activation energies and reaction orders for all MnO_x samples in the low temperature (≤ 210 °C) 2-propanol oxidation.

	MnO	Mn₃O₄	Mn₂O₃	MnO₂
E_A [kJ/mol]	81 ± 2	81 ± 1	65 ± 1	74 ± 1
a(C₃H₈O)	0.12 ± 0.01	(0.38 ± 0.07)	0.19 ± 0.01	0.14 ± 0.01
a(O₂)	0.26 ± 0.01	0.31 ± 0.02	0.20 ± 0.01	0.30 ± 0.02

5.3 Comparison of MnO_x in the two oxidation test reactions

Taking all the results from the previously described test reactions into account (numerical data is compiled in Table 12), a few insights into MnO_x catalysis can be obtained. Looking at the normalized formation rates at low temperatures during both reactions shows differing behavior of the high valent and low valent samples towards selective oxidation and the total combustion of the reactants. In CO oxidation the high valent samples (meaning the redox couple Mn(III)/Mn(IV)) show a higher activity and the same holds for the 2-propanol oxidation in temperature regions where total combustion has a substantial influence on the measured conversion. The lower valent samples (i.e. the redox couple Mn(II)/Mn(III)) on the other hand exhibit a much higher low temperature activity towards the selective oxidation of 2-propanol to acetone. These findings indicate an oxidation state reliant trend towards total oxidation for high valent Mn oxides and a better suitability for the selective oxidation of the low valent oxides. This seems plausible, since the high valent samples have more oxygen bound in the oxidic structure and can thus shift the chemical reaction towards the products of highest oxygen content (i.e. total combustion). The low valent samples on the other hand are supplying single oxygen atoms at a time making a desorption of the partially oxidized product much more likely until temperatures are so high and reaction is so fast that a total combustion is initiated for these compounds as well.

The reaction order investigation of these samples gave rise to some mechanistic understanding about manganese oxides. Different reaction patterns can be suggested for these reactions. In CO oxidation a competitive adsorption of O₂ and CO seemed the most plausible explanation which probably drove the reaction and thus suggests a Langmuir-Hinshelwood type reaction. A different behavior was found for the 2-propanol oxidation which leaves room for speculation and needs further investigation to elucidate the matter at hand. Nevertheless, the high possibility of differing reaction mechanisms taking precedence for the different test reactions could be problematic for the direct comparison between the two reactions. If the reaction pathways are different in both cases the rate-determining step could very well also differ even for the same material between the two oxidation reactions. Thus, making

5. Catalysis of Mn oxides

comprehensive conclusions about the intrinsic catalytic activity of the investigated samples has to be done with caution. Further studies to illuminate the nature of the present reactions and more different oxidation reactions should be investigated to further the understanding of the activity trends found here.

Table 12: Compilation of all numerical values obtained in the catalytic test reactions of CO and 2-propanol oxidation for all MnO_x samples.

		MnO	Mn₃O₄	Mn₂O₃	MnO₂
CO oxidation	E_A [kJ/mol]	73 ± 2	62 ± 2	61 ± 1	52 ± 1
	a(CO)	0.75 ± 0.02	0.67 ± 0.02	0.47 ± 0.01	0.23 ± 0.02
	a(O₂)	-0.03 ± 0.01	0.21 ± 0.03	0.15 ± 0.02	0.57 ± 0.07
	Normalized CO₂ formation rate at 200 °C [mmol/s m²]	9.0	15.3	56.1	48.3
LT (≤ 210 °C) 2-propanol oxidation	E_A [kJ/mol]	81 ± 2	81 ± 1	65 ± 1	74 ± 1
	a(C₃H₈O)	0.12 ± 0.01	(0.38 ± 0.07)	0.19 ± 0.01	0.14 ± 0.01
	a(O₂)	0.26 ± 0.01	0.31 ± 0.02	0.20 ± 0.01	0.30 ± 0.02
	Normalized C₃H₆O formation rate at 200 °C [mmol/s m²]	234.1	96.3	34.0	31.2

6. Correlation between catalytic behavior and bulk properties

The analysis of the samples after catalytic testing showed no transformation of the bulk structure of MnO, Mn₃O₄ and Mn₂O₃. Therefore, correlating bulk properties with the catalytic behavior of the samples might yield insights into possible responses of the material during catalysis. For the sake of completeness, data for MnO₂ is also presented. It is pointed out that correlations found with the catalytic data might be arbitrary, since this sample undergoes structural changes during the reactions described before. Since the model reactions performed in this study are oxidation reactions special attention will be paid to properties which are likely to influence the redox character of the samples, i.e. the Mn-O bond (length L_{Mn-O} and strength E_{Mn-O}), the band structure (band gap energy E_g and work function WF) and the energy of formation ΔH^0 and ΔG^0 .

Table 13 reports literature values for the enthalpy of formation and the Gibbs energy of formation at room temperature. The values listed here are internally in good agreement and only minor divergences can be found. Both the enthalpy and the Gibbs energy follow the same trend for the four samples. For reasons of simplicity only the enthalpy which offers more reference values will be discussed later in the context of the catalytic properties.

Band gap energy references for the four different MnO_x species are reported in Table 14. Due to the significant variation of the data, the method from which the individual values are derived is included. Furthermore, any nanoscaling of the sample is also denoted, since this has a considerable influence on the band structure. All samples exhibit a large range of reported band gap energies which makes the accurate utilization of this parameter difficult. The physical origin for the spread of data arises from the sensitivity of this property on surface orientation, integrity, presence of adsorbates and the measuring environment. E_g values for MnO range from 1.8 to 4.0 eV, while for Mn₃O₄ reports on band gap energies can be found exclusively for nanoscaled materials ranging from 2.07 to 3.70 eV. Only a single value of $E_g = 1.35$ eV derived from a bulk sample is available for α -Mn₂O₃ while other

6. Correlation between catalytic behavior and bulk properties

band gap energies ranging from 1.20 to 3.69 eV result from nanoparticle samples. E_g values for β - MnO_2 are reported between 0.26 and 2.23 eV. Therefore, even though E_g might have an influence on the reactions at hand, it will not be discussed further in this work.

Table 13: Literature values for the enthalpy of formation $\Delta H^0_{298\text{K}}$ and Gibbs energy of formation $\Delta G^0_{298\text{K}}$ at RT.^[121]

$\Delta H^0_{298\text{K}}$ [kcal/mol]	$\Delta G^0_{298\text{K}}$ [kcal/mol]	Reference
MnO		
-92.04 ± 0.11	-86.76	[122]
-92.20 ± 0.18		[123]
-92.0 ± 0.5		[124]
-90.8		[125]
-93.1 ± 0.3		[126]
Mn₃O₄		
-331.7	-306.7	[127]
-331.2	-305.6	[128]
	-306.2	[129]
-331.4	-308.1	[130]
α-Mn₂O₃		
-232.1		[131]
-229.2 ± 0.9	-210.6 ± 2.2	[128,130,132]
-228.7 ± 0.2		[133]
-230.1		[134]
-229.5		[135]
-229.4		[136]
β-MnO₂		
-124.5	-111.4	[131]
-124.2 ± 0.2	-111.2	[128]
-124.45 ± 0.2	-111.35 ± 0.25	[130,132]
-124.0		[137]
	-111.1	[138]
	-110.1	[139]
	-109.9	[140]

6. Correlation between catalytic behavior and bulk properties

Table 14: Measured band gap energies E_g from literature. Compare also chapter 1.2.5.^[121]

E_g [eV]	Comment	Reference
MnO		
1.8	from thermoelectric power measurements	[141]
2.0	nanoparticles, from light absorption	[47]
2.09	from conductivity measurements	[142]
2.3	from conductivity	[143]
2.43 ± 0.08	from conductivity measurements	[144]
2.6 ± 0.2	from conductivity measurements	[145]
3.26	from augmented plane-wave method	[146]
3.6	from conductivity measurements	[147]
3.5 to 4.0	from UV absorption	[148]
3.6 to 3.8	from UV absorption	[149]
3.9 ± 0.4	from bremsstrahlung isochromat spectroscopy	[59]
Mn₃O₄		
2.07	nanosized, from light absorption	[48]
2.30	nanosized, from light absorption	[49]
2.50	nanosized, from light absorption	[50]
2.54	nanosized, from light absorption	[45]
3.28 to 3.75	nanosized, from light absorption	[51]
3.70	nanosized, from light absorption	[47]
α-Mn₂O₃		
1.20	nanoparticles, from light absorption	[52]
1.35	from Kelvin probe and photoemission	[150]
1.91	nanoparticles, from light absorption	[53]
2.01	nanoparticles, from light absorption	[53]
2.09	nanoparticles, from light absorption	[53]
2.99	nanoparticles, from light absorption	[54]
3.69	nanoparticles, from light absorption	[51]
β-MnO₂		
0.26	from conductivity measurements	[151]
0.37	from conductivity measurements	[152]
1.0	from x-ray spectroscopy	[58]
2.23	nanosheets, from light absorption	[56]

6. Correlation between catalytic behavior and bulk properties

Values for the work function, the Mn-O bond lengths and mean Mn-O bond strengths from literature are compiled in

Table 15. The bond lengths extracted from the ICSD patterns will be used for examining a correlation with the catalytic behavior, since these values are considered the most accurate. The work function of MnO will be averaged to 4.0 eV.

To visualize the catalytic behavior and the different parameters compiled above, the mean Mn oxidation state of all samples has been calculated (+2 for MnO, +2.67 for Mn₃O₄, +3 for Mn₂O₃ and +4 for MnO₂) and used as the x-axis for the data plots (Figure 57). In this way the differing behavior of the samples in the two test reactions can be illustrated comprehensibly. For the 2-propanol oxidation only the length of the shortest Mn-O bond in the different crystal structures seems to align to the normalized rate of acetone formation. The trend observed for the normalized rate of CO₂ formation from CO oxidation however can roughly be found in two different parameters illustrated here. On the one hand the longest Mn-O bond lengths in the given crystal structures show a similar behavior as the catalytic activity. This observation is especially interesting due to the correlation of 2-propanol oxidation activity with the shortest bond lengths. Since both reactions have differing reactivity patterns and consequently are expected to function via two different active sites this finding might indicate an involvement of two different kinds of Mn-O bonds in the formation of the respective products.

On the other hand, the work function also shows a similar trend as the rate of product formation in CO oxidation. This could indicate a rate limitation of the catalytic process by the electron transfer from the catalyst to the reactant.

The enthalpy of formation and Mn-O bond energy do not seem to correlate with the catalytic behavior of the samples investigated here. However, only a single value for the bond strength of each present sample could be found which excludes a reliability check of the data. Furthermore, the values are averaged over the whole sample in a mean Mn-O bond energy, which is not a good approximation in the presented study, since the catalytic activity seems to scale with specific Mn-O bonds. Thus, the individual bond strengths of the longest and shortest Mn-O bonds in the respective crystal structures could likely provide deeper insight into the processes observed here.

6. Correlation between catalytic behavior and bulk properties

Table 15: Literature values for the Mn-O bond length, bond strength and the work function.

Parameter	Value	Reference
MnO		
Mn-O bond length [Å]	2.222	ICSD-643195
Mean Mn-O bond strength [kcal/mol]	36	[153]
Work function [eV]	4.4	[154]
Work function [eV]	3.6 to 4.2	[155]
Mn₃O₄		
Octahedron Mn-O bond length [Å]	1.88	[156]
Tetrahedron Mn-O bond length [Å]	2.039	ICSD-77478
Tetrahedron Mn-O bond length [Å]	2.07	[156]
Octahedron Mn-O bond length [Å]	1.932 and 2.287	ICSD-77478
Mean Mn-O bond strength [kcal/mol]	55.4	[157]
Work function [eV]	4.0	[158]
α-Mn₂O₃		
Mn-O bond length [Å]	1.875 to 2.306	[159,160]
Mn-O bond length [Å]	1.897 to 2.412	ICSD-9091
Mean Mn-O bond strength [kcal/mol]	48.0	[157]
Work function [eV]	5.12	[150]
β-MnO₂		
Mn-O bond length [Å]	1.884	[161]
Mn-O bond length [Å]	1.85 and 1.91	[162]
Mn-O bond length [Å]	1.882 and 1.895	ICSD-73716
Mn-O bond strength [kcal/mol]	52	[153]
Work function [eV]	4.4	[163]

6. Correlation between catalytic behavior and bulk properties

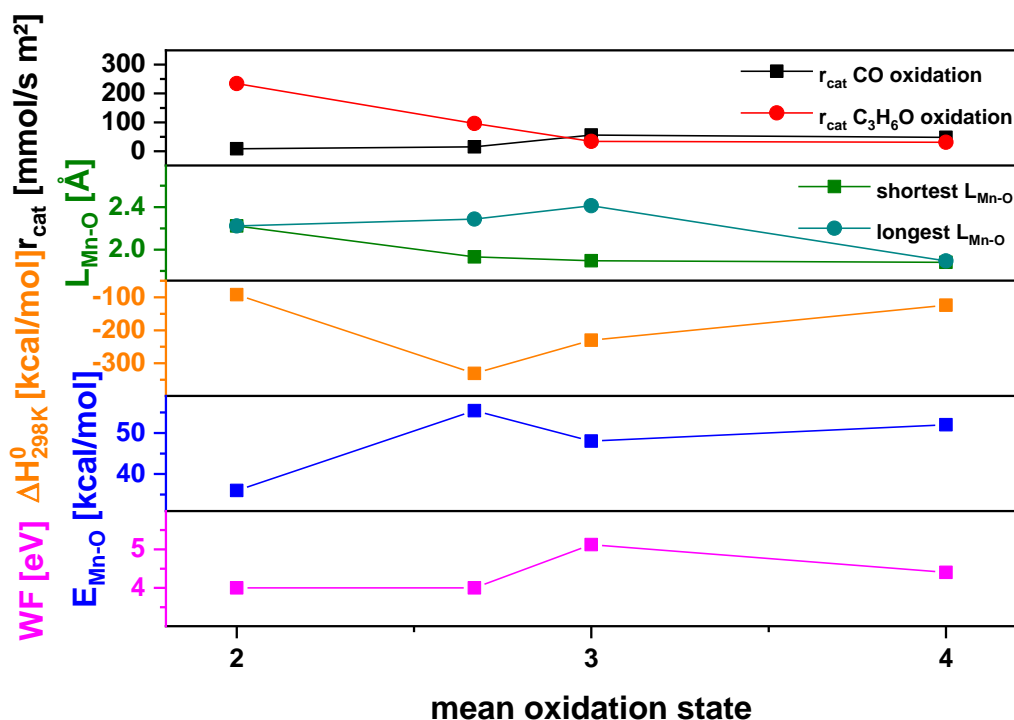


Figure 57: Normalized product formation rates at 200 °C r_{cat} , Mn-O bond length $L_{\text{Mn-O}}$, enthalpy of formation ΔH_{298K}^0 , mean Mn-O bond strength $E_{\text{Mn-O}}$ and work function WF plotted against the mean oxidation state of Mn in MnO_x .

This result can be rationalized in the following way. The shortest Mn-O bond is an indication for the basicity of the surface. It hence can be considered as a proxy for the ability of the surface to accept protons. Consequently, the above discussed reaction pathway for 2-propanol transformation as acid-base reaction is strongly supported. The regeneration of this bond after having accepted a proton and likely being desorbed as water molecule is hence not rate-limiting as probed by the kinetics of the conversion of the organic substrate.

The oxidation of CO can only be accomplished through an electron transfer reaction and is thus a redox reaction in the rate-limiting step. If one follows the notion that surface lattice oxygen is the oxidizing species for CO and the resulting defect is replenished by gas phase oxygen, then the expected active site is the weakest Mn-O bond.

In both reactions the Mn oxides follow the general concept of a Mars-van-Krevelen (MvK) mechanism. This concept states that the kinetics of the transformation of the organic substrate and the kinetics of the regeneration of the active site through

6. Correlation between catalytic behavior and bulk properties

reaction with oxygen follow different time laws that cannot be probed without studying the kinetics of oxygen consumption independent from the kinetics of the organic substrate transformation. Such an in-depth kinetic analysis was not the target of the present work. It remains thus at this state a likely but speculative conclusion to assign the catalytic reactivity of the Mn oxides studied to the concept of a MvK mechanism.

The phenomenological correlation of reactivity and local structural parameters does not mean that the samples are terminated with a regular crystal structure from which the Mn-O bond lengths were derived. It is rather likely that the values stand as proxies for the bond length anisotropy of Mn_xO_y coordination polyhedra that are expected to terminate the oxides in a molecular or disordered state without long-range order. Only then it is likely that Mn-O bonds can be exchanged with the adsorbates without exceedingly high activation barriers coming from the periodicity of an oxide structure. This view is supported by the lacking correlation of the reactivity with the bulk heat of formation of the oxides.

In summary, probing the chemical reactivity by two catalytic reactions exhibiting two different rate-determining steps proved to be a valuable method for finding out about the interface chemistry of binary oxides. The allegation that Mn oxides are strong oxidation agents and facile oxygen donor systems is not valid in this generalized form and under the conditions of testing applied here.

7. Conclusion and Outlook

The first aim of the present work was finding a suitable combination of techniques to analyze the phase composition and oxidation states of unknown manganese oxide samples. It was shown, that temperature programmed oxidation is a powerful technique to obtain the sought information and due to the chemical nature of the analysis no information on the composition is lost or altered during the experiment which cannot be excluded for spectroscopic techniques. The individual oxidation states in an oxidic sample can be quantified and deconvoluted except for the thermodynamically most stable form of MnO_x , the Hausmannite phase. It is inert in the experiment which limits the applicability and additional techniques are needed for a comprehensive analysis of an unknown MnO_x sample. To this end, temperature programmed reduction was introduced as a complementary technique to the TPO. Again, due to the chemical nature of this analysis method a loss of information to the fast reaction of the sample with electromagnetic radiation can be excluded. The amount of reduced species can be quantified as well and even though the individual reduction events are not as accurately deconvoluted in this reaction as in the oxidation, combining both results is sufficient for a complete oxidation state analysis of the sample. As a third complementary method Raman spectroscopy has been applied, aiming at minimal radiation damage due to the low energy of the incident beam. Although the acquisition of good spectra is hard due to the low intensities which are tolerated by the samples before alteration occurs, a set of reference spectra was recorded. These can be used to identify different manganese phases in unknown samples. Furthermore, the Hausmannite phase features the highest Raman intensity and is most stable under irradiation. Thus, it can be easily distinguished from all other MnO_x phases and provides the most needed qualitative information which is vital for the interpretation of the TPO data. This makes Raman spectroscopy a valuable complementary asset in the identification of MnO_x .

The usefulness of these methods was shown first on an amorphous sample where the phase composition was determined solely by means of TPO. Afterwards the combination of all techniques described above together with PXRD was utilized to identify the set of samples of highest purity for the second assignment of this work.

7. Conclusion and Outlook

The second part of this work is aimed at gaining a deeper understanding of the intrinsic catalytic properties of MnO_x . To this end, the thermodynamically most stable MnO_x have been used in the catalytic oxidation of CO and 2-propanol. For the CO oxidation a competitive adsorption and Langmuir-Hinshelwood type mechanism could be presumed, whereas the reaction mechanism in the 2-propanol oxidation was suggested to be of a different nature. All samples exhibited 100% selectivity towards acetone at low temperatures in the catalytic 2-propanol oxidation. It was demonstrated that acetone was formed by acid-base dehydration reaction in minimal amounts only on the Mn_3O_4 sample, most of the acetone was thus formed in an oxidation with oxygen. In addition, an oxygen storage behavior was identified for the low valent samples (MnO and Mn_3O_4) which enabled an ongoing reaction for a prolonged time after oxygen removal from the feed gas. This capability was not found for the high valent samples (Mn_2O_3 and MnO_2). Furthermore, the two different redox couples present in manganese oxide structures were found to be beneficial for different reaction pathways: samples with the Mn(II)/Mn(III) redox pair showing higher activity in the selective oxidation of 2-propanol to acetone than samples with the Mn(III)/Mn(IV) couple. The latter materials on the other hand exhibited higher activities in the total combustion reactions of CO and 2-propanol to CO_2 and H_2O . In addition to these findings a few open questions still persist and could be investigated in the future: What is the reaction mechanism of MnO_x in the 2-propanol oxidation and do the samples exhibit a Mars-van-Krevelen type behavior? This question could be answered by performing catalytic experiments with isotopically labeled oxygen to see whether oxygen from the sample or the feed gas can be found in the products. Furthermore, the recovered samples which contain labeled oxygen could be used for the investigation of the storage behavior of the low valent MnO_x . Furthermore, additional catalytic test reactions need to be considered if a comparative overview of the intrinsic catalytic activity of the investigated samples is to be obtained. Oxidation reactions with a multitude of different possible products could be used to determine a possible difference in the catalytic behavior of MnO_x .

8. References

- [1] R. Schlögl (Ed.) *Chemical energy storage*, De Gruyter, Berlin, **2013**.
- [2] A. Boudghene Stambouli, H. Koinuma, S. Flazi, Z. Khiat, Y. Kitamura, *REPQJ* **2013**, 1, 110.
- [3] F. Ausfelder, C. Beilmann, M. Bertau, S. Bräuninger, A. Heinzl, R. Hoer, W. Koch, F. Mahlendorf, A. Metzethin, M. Peuckert et al., *ChemBioEng Reviews* **2017**, 4, 144.
- [4] W. Liao, R. Heijungs, G. Huppel, *Renewable and Sustainable Energy Reviews* **2012**, 16, 996.
- [5] J. Emsley, *Nature's building blocks. An A-Z guide to the elements*, Oxford Univ. Press, Oxford, **2003**.
- [6] L. A. Paquette (Ed.) *Encyclopedia of reagents for organic synthesis. [(EROS)]*, Wiley, Chichester, **2009**.
- [7] K. V. Raghavan, B. M. Reddy, *Industrial Catalysis and Separations. Innovations for Process Intensification*, Apple Academic Press, Hoboken, **2014**.
- [8] J. Hagen, *Industrial catalysis. A practical approach*, Wiley-VCH, Weinheim, Germany, **2015**.
- [9] J. Barber, *Chemical Society reviews* **2009**, 38, 185.
- [10] W. Lubitz, E. J. Reijerse, J. Messinger, *Energy Environ. Sci.* **2008**, 1, 15.
- [11] *Gesamtausgabe der Energiedaten - Datensammlung des BMWi, Bundesministerium für Wirtschaft und Energie, 2018 Received from: <https://www.bmwi.de/Redaktion/DE/Artikel/Energie/energiedaten-gesamtausgabe.html> (Download 07.08.2018).*
- [12] *BP Statistical Review of World Energy, 2017, Received from: www.bp.com (Download: 07.08.2018).*
- [13] *NOAA ESRL Global Monitoring Division. 2016, updated annually. Atmospheric Carbon Dioxide Dry Air Mole Fractions from quasi-continuous measurements at Mauna Loa, Hawaii. Compiled by K.W. Thoning, D.R. Kitzis, and A. Crotwell. National Oceanic and Atmospheric Administration (NOAA), Earth System Research Laboratory (ESRL), Global Monitoring Division (GMD): Boulder, Colorado, USA. Version 2017-8 at <http://dx.doi.org/10.7289/V54X55RG>.*
-

8. References

- [14] T. Stocker (Ed.) *Climate change 2013. The physical science basis: Working Group I contribution to the Fifth assessment report of the Intergovernmental Panel on Climate Change*, Cambridge University Press, Cambridge, **2014**.
- [15] N. H. Stern, *The economics of climate change. The Stern review*, Cambridge Univ. Press, Cambridge, **2011**.
- [16] J. D. Holladay, J. Hu, D. L. King, Y. Wang, *Catalysis Today* **2009**, 139, 244.
- [17] S. Anantharaj, S. R. Ede, K. Sakthikumar, K. Karthick, S. Mishra, S. Kundu, *ACS Catal.* **2016**, 6, 8069.
- [18] B. Ohtani, *Physical chemistry chemical physics : PCCP* **2014**, 16, 1788.
- [19] C. Clarke, S. Upson, *Neurotoxicology* **2017**, 58, 173.
- [20] F. W. Boulger, R. C. Buehl, *JOM* **1952**, 4, 468.
- [21] B. Elvers, F. Ullmann (Eds.) *Ullmann's encyclopedia of industrial chemistry*, Wiley-VCH, Weinheim, **2011**.
- [22] A. Z. Weber, M. M. Mench, J. P. Meyers, P. N. Ross, J. T. Gostick, Q. Liu, *J Appl Electrochem* **2011**, 41, 1137.
- [23] G. Leclanché, *Les mondes* **1868**, 16, 532.
- [24] Gassner C., US373064A.
- [25] Krampitz H., Wohner G., US6706443B1.
- [26] A. E. Smith, H. Mizoguchi, K. Delaney, N. A. Spaldin, A. W. Sleight, M. A. Subramanian, *J. Am. Chem. Soc.* **2009**, 131, 17084.
- [27] P. J. Heyes, K. Anastasakis, W. de Jong, A. van Hoesel, W. Roebroeks, M. Soressi, *Scientific reports* **2016**, 6, 22159.
- [28] U. Zoller, *Applications*, Taylor & Francis, Boca Raton, **2009**.
- [29] R. Sundararaman, X. Ma, C. Song, *Ind. Eng. Chem. Res.* **2010**, 49, 5561.
- [30] J. Attenburrow, A. F. B. Cameron, J. H. Chapman, R. M. Evans, B. A. Hems, A. B. A. Jansen, T. Walker, *J. Chem. Soc.* **1952**, 1094.
- [31] <http://www.catxel.com/catalysts-and-compounds/existing-products/>
accessed: 26.07.2018.
- [32] S. Ristig, N. Cibura, J. Strunk, *Green* **2015**, 5, 189.
- [33] A. F. Holleman, E. Wiberg, N. Wiberg, *Lehrbuch der anorganischen Chemie*, De Gruyter, Berlin, **2007**.
- [34] D. Jarosch, *Mineralogy and Petrology* **1987**, 37, 15.
-

8. References

- [35] S. Geller, *Acta Cryst.* **1971**, *B27*, 821.
- [36] A. Bystrom, A. M. Bystrom, *Acta Cryst.* **1950**, *3*, 146.
- [37] A. M. Byström, *Acta Chemica Scandinavica* **1949**, *3*, 163.
- [38] B. Zachau-Christiansen, K. West, T. Jacobsen, S. Skaarup, *Solid State Ionics* **1994**, *70/71*, 401.
- [39] C. B. Azzoni, M. C. Mozzati, P. Galinetto, A. Paleari, V. Massarotti, D. Capsoni, M. Bini, *Solid State Communications* **1999**, *112*, 375.
- [40] E. R. Stobbe, B. A. de Boer, J. W. Geus, *Catalysis Today* **1999**, *47*, 161.
- [41] A. Aboukaïs, E. Abi-Aad, B. Taouk, *Materials Chemistry and Physics* **2013**, *142*, 564.
- [42] G. Picasso, M. Gutiérrez, M. P. Pina, J. Herguido, *Chemical Engineering Journal* **2007**, *126*, 119.
- [43] J. Carnö, M. Ferrandon, E. Björnbom, S. Järas, *Applied Catalysis A: General* **1997**, *155*, 265.
- [44] D. Delimaris, T. Ioannides, *Applied Catalysis B: Environmental* **2008**, *84*, 303.
- [45] R. Xu, X. Wang, D. Wang, K. Zhou, Y. Li, *Journal of Catalysis* **2006**, *237*, 426.
- [46] W. J. Rankin, van Deventer, J. S. J. **1980**, *80*, 239.
- [47] N. A. M. Barakat, K.-D. Woo, S. G. Ansari, J.-A. Ko, M. A. Kanjwal, H. Y. Kim, *Appl. Phys. A* **2009**, *95*, 769.
- [48] A. Jha, R. Thapa, K. K. Chattopadhyay, *Materials Research Bulletin* **2012**, *47*, 813.
- [49] D. P. Dubal, D. S. Dhawale, R. R. Salunkhe, S. M. Pawar, C. D. Lokhande, *Applied Surface Science* **2010**, *256*, 4411.
- [50] D. P. Dubal, D. S. Dhawale, R. R. Salunkhe, S. M. Pawar, V. J. Fulari, C. D. Lokhande, *Journal of Alloys and Compounds* **2009**, *484*, 218.
- [51] N. M. Hosny, A. Dahshan, *Materials Chemistry and Physics* **2012**, *137*, 637.
- [52] Q. Javed, F. P. Wang, M. Y. Rafique, A. M. Toufiq, Q. S. Li, H. Mahmood, W. Khan, *Nanotechnology* **2012**, *23*, 415603.
- [53] Q.-u.-a. Javed, W. Feng-Ping, M. Y. Rafique, A. M. Toufiq, M. Z. Iqbal, *Chinese Phys. B* **2012**, *21*, 117311.
- [54] H. Zhang, Z. Ji, T. Xia, H. Meng, C. Low-Kam, R. Liu, S. Pokhrel, S. Lin, X. Wang, Y.-P. Liao et al., *ACS Nano* **2012**, *6*, 4349.
-

8. References

- [55] Z.-R. Tian, W. Tong, J.-Y. Wang, N.-G. Duan, V. V. Krishnan, S. L. Suib, *Science* **1997**, 276, 926.
- [56] N. Sakai, Y. Ebina, K. Takada, T. Sasaki, *J Phys Chem B* **2005**, 109, 9651.
- [57] B. A. Pinaud, Z. Chen, D. N. Abram, T. F. Jaramillo, *J. Phys. Chem. C* **2011**, 115, 11830.
- [58] D. M. Sherman, *Geochimica et Cosmochimica Acta* **2005**, 69, 3249.
- [59] S. V. Faleev, M. van Schilfgaarde, T. Kotani, *Phys. Rev. Lett.* **2004**, 93.
- [60] F. Tran, P. Blaha, *Phys. Rev. Lett.* **2009**, 102.
- [61] M. Marsman, J. Paier, A. Stroppa, G. Kresse, *J Phys Condens Matter* **2008**, 20, 64201.
- [62] C. Franchini, R. Podloucky, J. Paier, M. Marsman, G. Kresse, *Phys. Rev. B* **2007**, 75.
- [63] D. A. Shaughnessy, H. Nitsche, C. H. Booth, D. K. Shuh, G. A. Waychunas, R. E. Wilson, H. Gill, K. J. Cantrell, R. J. Serne, *Environ. Sci. Technol.* **2003**, 37, 3367.
- [64] W. Janusz, A. Galgan, *Physicochemical Problems of Mineral Processing* **2001**, 35, 31.
- [65] S.E. O'Reilly, M. F. Hochella, *Geochimica et Cosmochimica Acta* **2003**, 67, 4471.
- [66] B. Pr elot, F. Villi eras, M. Pelletier, A. Razafitianamaharavo, F. Thomas, C. Poinسیون, *Journal of Colloid and Interface Science* **2003**, 264, 343.
- [67] M. J. Gray, M. A. Malati, M. W. Rophael, *J. Electroanal. Chem.* **1978**, 89, 135.
- [68] R. Natarajan, D. W. Fuerstenau, *International Journal of Mineral Processing* **1983**, 11, 139.
- [69] Q. Zhang, X. Cheng, C. Zheng, X. Feng, G. Qiu, W. Tan, F. Liu, *Journal of Environmental Sciences* **2011**, 23, 1904.
- [70] M. Kosmulski, *Adv Colloid Interface Sci* **2009**, 152, 14.
- [71] M. Kosmulski, *J Colloid Interface Sci* **2004**, 275, 214.
- [72] K. Arshak, O. Korostynska, *Ann. Phys.* **2004**, 13, 87.
- [73] K. Arshak, O. Korostynska, *Materials Science and Engineering: B* **2006**, 133, 1.
-

8. References

- [74] V. M. Browning, R. M. Stroud, W. W. Fuller-Mora, J. M. Byers, M. S. Osofsky, D. L. Knies, K. S. Grabowski, D. Koller, J. Kim, D. B. Chrisey et al., *Journal of Applied Physics* **1998**, *83*, 7070.
- [75] F. F. Marafatto, M. L. Strader, J. Gonzalez-Holguera, A. Schwartzberg, B. Gilbert, J. Peña, *Proceedings of the National Academy of Sciences of the United States of America* **2015**, *112*, 4600.
- [76] J. W. Niemantsverdriet, *Spectroscopy in Catalysis*, Wiley-VCH, Hoboken, **2007**.
- [77] M. A. Banares, I. E. Wachs, *Encyclopedia of Analytical Chemistry (EAC) online*.
- [78] P. W. Atkins, J. de Paula, *Physikalische Chemie*, Wiley-VCH, Weinheim, **2012**.
- [79] H. Lauron-Pernot, *Catalysis Reviews* **2006**, *48*, 315.
- [80] B. Bai, J. Li, J. Hao, *Applied Catalysis B: Environmental* **2015**, *164*, 241.
- [81] K. Li, J. Chen, Y. Peng, W. Lin, T. Yan, J. Li, *J. Mater. Chem. A* **2017**, *5*, 20911.
- [82] S. Liang, F. Teng, G. Bulgan, R. Zong, Y. Zhu, *J. Phys. Chem. C* **2008**, *112*, 5307.
- [83] X. Shen, Y. Ding, J. Liu, K. Laubernds, R. P. Zerger, M. Polverejan, Y.-C. Son, M. Aindow, S. L. Suib, *Chem. Mater.* **2004**, *16*, 5327.
- [84] A. Gil, P. Ruiz, B. Delmon, *Can. J. Chem. Eng.* **1996**, *74*, 600.
- [85] K. Ramesh, L. Chen, F. Chen, Y. Liu, Z. Wang, Y.-F. Han, *Catalysis Today* **2008**, *131*, 477.
- [86] S. Dey, G. C. Dhal, D. Mohan, R. Prasad, *Atmospheric Pollution Research* **2018**, *9*, 755.
- [87] S.S.T. Bastos, J.J.M. Órfão, M.M.A. Freitas, M.F.R. Pereira, J. L. Figueiredo, *Applied Catalysis B: Environmental* **2009**, *93*, 30.
- [88] K. A. Stoerzinger, M. Risch, B. Han, Y. Shao-Horn, *ACS Catal.* **2015**, *5*, 6021.
- [89] S. D. Robertson, B. D. McNicol, J. H. de Baas, S. C. Kloet, J. W. Jenkins, *Journal of Catalysis* **1975**, *37*, 424.
- [90] N. W. Hurst, S. J. Gentry, A. Jones, B. D. McNicol, *Catalysis Reviews Science and Engineering* **1982**, *24*, 233.
-

8. References

- [91] M. Fadoni, L. Lucarelli, *ADSORPTION AND ITS APPLICATIONS IN INDUSTRY AND ENVIRONMENTAL PROTECTION, VOL I: APPLICATIONS IN INDUSTRY* **1999**, 120, 177.
- [92] B. Jouguet, A. Gervasini, A. Auroux, *Chem. Eng. Technol.* **1995**, 18, 243.
- [93] P. Malet, A. Caballero, *J. Chem. Soc., Faraday Trans. 1* **1988**, 84, 2369.
- [94] D. A. M. Monti, A. Baiker, *Journal of Catalysis* **1983**, 83, 323.
- [95] F. Kapteijn, A. D. Vanlangeveld, J. A. Moulijn, A. Andreini, M. A. Vuurman, A. M. Turek, J. M. Jehng, I. E. Wachs, *Journal of Catalysis* **1994**, 150, 94.
- [96] N. Mironova-Ulmane, A. Kuzmin, M. Grube, *Journal of Alloys and Compounds* **2009**, 480, 97.
- [97] H-h. Chou and H. Y. Fan, *Phys. Rev. B* **1976**, 13, 3924.
- [98] C.M. Julien, M. Massot, C. Poinsignon, *Spectrochimica Acta Part A: Molecular and Biomolecular Spectroscopy* **2004**, 60, 689.
- [99] B. R. Strohmeier, D. M. Hercules, *J. Phys. Chem.* **1984**, 88, 4922.
- [100] H. D. Lutz, B. Müller, H. J. Steiner, *Journal of Solid State Chemistry* **1991**, 90, 54.
- [101] F. Buciuman, F. Patcas, R. Craciun, D. R. T. Zahn, *Phys. Chem. Chem. Phys.* **1999**, 1, 185.
- [102] H. Y. Xu, S. Le Xu, X. D. Li, H. Wang, H. Yan, *Applied Surface Science* **2006**, 252, 4091.
- [103] W. B. White, V. G. Keramidas, *Spectrochimica Acta Part A: Molecular Spectroscopy* **1972**, 28, 501.
- [104] Lopez de Mishima, B. A., T. Ohtsuka, N. Sato, *J. Electroanal. Chem.* **1988**, 243, 219.
- [105] D. Gosztola, M. J. Weaver, *Journal of Electroanalytical Chemistry and Interfacial Electrochemistry* **1989**, 271, 141.
- [106] I. Halasz, A. Brenner, M. Shelef, K. Y. Simon NG, *Catal Lett* **1990**, 6, 349.
- [107] Y. YAO, *Journal of Catalysis* **1975**, 39, 104.
- [108] Y. Sun, Q. Liu, S. Gao, H. Cheng, F. Lei, Z. Sun, Y. Jiang, H. Su, S. Wei, Y. Xie, *Nature communications* **2013**, 4, 2899.
- [109] L. Simonot, F. Garin, G. Maire, *Applied Catalysis B: Environmental* **1997**, 11, 167.
-

8. References

- [110] Y. YAO, *Journal of Catalysis* **1974**, 33, 108.
- [111] X. Xie, Y. Li, Z.-Q. Liu, M. Haruta, W. Shen, *Nature* **2009**, 458, 746.
- [112] Y.-J. Chen, D. Wu, C. Yeh, *Rev. Adv. Mater. Sci.* **2003**, 5, 41.
- [113] Y. YAO, *Journal of Catalysis* **1973**, 28, 139.
- [114] A. Terlecki-Baric'evic', B. Grbic', D. Jovanovic', S. Angelov, D. Mehandz'iev, C. Marinova, P. Kirilov-Stefanov, *Applied Catalysis* **1989**, 47, 145.
- [115] G. G. Jernigan, G. A. Somorjai, *Journal of Catalysis* **1994**, 147, 567.
- [116] W. E. Garner, F. S. Stone, P. F. Tiley, *Proc. R. Soc. Lond. A* **1952**, 211, 472.
- [117] J. WALKER, *Journal of Catalysis* **1988**, 110, 298.
- [118] Y. Iizuka, M. Sanada, J. Tsunetoshi, N. Yamauchi, S. Arai, *J. Chem. Soc., Faraday Trans.* **1994**, 90, 3449.
- [119] Y. YAO, *Journal of Catalysis* **1973**, 28, 124.
- [120] G. Parravano, *J. Am. Chem. Soc.* **1953**, 75, 1448.
- [121] L. Gmelin, E. H. E. Pietsch, A. Kotowski, *Gmelins Handbuch der anorganischen Chemie. MANGAN Teil C1*, Verlag Chemie, Weinheim, Germany, **1973**.
- [122] J. C. Southard, C. H. Shomate, *J. Am. Chem. Soc.* **1942**, 64, 1770.
- [123] C. B. Alcock, S. Zador, *Electrochimica Acta* **1967**, 12, 673.
- [124] O. Kubaschewski, C. B. Alcock, A. L. Evans, *Oxford : Pergamon 4th ed.* **1967**, 495.
- [125] H. Le Chatelier, *Compt. Rend.* **1896**, 122, 80.
- [126] H. Ulich, H. Siemonsen, *Archiv für das Eisenhüttenwesen* **1940**, 14, 27.
- [127] D. D. Wagman, W. H. Evans, V. B. Parker, I. Halow, S. M. Bailey, R. H. Schumm, *Natl. Bur. Std. [U.S.] Tech. Note* **1969**, 270-4, 106.
- [128] L. Brewer, *Chem. Rev.* **1953**, 52, 1.
- [129] O. Bricker, *Am. Mineralogist* **1965**, 50, 1296.
- [130] C. E. Wicks, F. E. Block, *U.S. Bur. Mines Bull.* **1963**, 605, 1.
- [131] F. D. Rossini, D. D. Wagman, W. H. Evans, S. Levine, I. Jaffe, *Natl. Bur. Std. [U.S.] Circ.* **1952**, 500, 274.
- [132] J. P. Coughlin, *U.S. Bur. Mines Bull.* **1954**, 542, 1.
- [133] E. M. Otto, *J. Electrochem. Soc.* **1964**, 111, 88.
- [134] T. R. Ingraham, *Canadian Metallurgical Quarterly* **2013**, 5, 109.
-

8. References

- [135] D. Q. Kim, Y. Wilbert, F. Marion, *Compt. Rend., Ser. C*, **1966**, 262, 756.
- [136] F. Shenouda, S. Aziz, *J. Appl. Chem.* **1967**, 17, 258.
- [137] E. M. Otto, *J. Electrochem. Soc.* **1965**, 112, 367.
- [138] W. M. Latimer, *Oxidation Potentials-The Oxidation States of the Elements and Their Potentials in Aqueous Solutions*, Englewood Cliffs, N.Y., **1952**.
- [139] G. Jangg, *Z. Anorg. Allg. Chem.* **1961**, 311, 186.
- [140] K. K. Kelley, G. E. Moore, *J. Am. Chem. Soc.* **1943**, 65, 782.
- [141] C. Crevecoeur, H. J. de Wit, *Solid State Communications* **1968**, 6, 295.
- [142] H. L. McKinzie, *Diss. Arizona State Univ.* **1968**, 1.
- [143] N. G. Eror, J. B. Wagner, *J. Electrochem. Soc.* **1971**, 118, 1665.
- [144] A. Z. Hed, D. S. Tannhauser, *The Journal of Chemical Physics* **1967**, 47, 2090.
- [145] M. Gvishi, *Solid State Communications* **1971**, 9, 2089.
- [146] T. M. Wilson, *Proc. Intern. Symp. At. Mol. Solid State Theory. Quantum Biol.*, Sanibel Island, Florida, **1970**.
- [147] Y. M. Ksendzov, V. V. Makarov, *Fiz. Tverd. Tela (Leningrad)* **1970**, 12, 3166.
- [148] G. W. Pratt, R. Coelho, *Phys. Rev.* **1959**, 116, 281.
- [149] R. N. Iskenderov, I. A. Drabkin, R. N. Emel'yanova, Y. M. Ksendzov, *Fiz. Tverd. Tela (Leningrad)* **1968**, 10, 2573.
- [150] A. Ginsburg, D. A. Keller, H.-N. Barad, K. Rietwyk, Y. Bouhadana, A. Anderson, A. Zaban, *Thin Solid Films* **2016**, 615, 261.
- [151] J. P. Chevillot, J. Brenet, *Schweizer Archiv. Angew. Wiss. n. Tech* **1960**, 26, 10.
- [152] P. H. Klose, *J. Electrochem. Soc.* **1970**, 117, 854.
- [153] A. A. Appen, V. B. Glushkova, S. S. Kayalova, *Izv. Akad. Nauk SSSR, Neorg. Mater*, **1965**, 1, 576.
- [154] H. Hsin-Kuei, J.W. Rabalais, *Surface Science* **1981**, 107, 376.
- [155] B. Lescop, *Applied Surface Science* **2006**, 252, 2276.
- [156] K. Satomi, *J. Phys. Soc. Jpn.* **1961**, 16, 258.
- [157] K. Klier, *Journal of Catalysis* **1967**, 8, 14.
- [158] P. Legutko, T. Jakubek, W. Kaspera, P. Stelmachowski, Z. Sojka, A. Kotarba, *Catalysis Communications* **2014**, 43, 34.
-

8. References

- [159] R. Norrestam, *Acta Chem. Scand.* **1967**, *21*, 2871.
- [160] L. Pauling, M. D. Shappell, *Zeitschrift für Kristallographie - Crystalline Materials* **1930**, *75*.
- [161] J. Brenet, *Bulletin de Minéralogie* **1950**, *73*, 409.
- [162] K. Siratori, S. Iida, *J. Phys. Soc. Jpn.* **1960**, *15*, 2362.
- [163] J. Chang, M. Jin, F. Yao, T. H. Kim, V. T. Le, H. Yue, F. Gunes, B. Li, A. Ghosh, S. Xie et al., *Adv. Funct. Mater.* **2013**, *23*, 5074.

9. Eidesstattliche Erklärung

Hiermit versichere ich, die vorliegende Arbeit mit dem Titel

**„Fundamental studies on the catalytic properties of manganese oxides in
oxidation reactions “**

selbständig verfasst und keine außer den angegebenen Hilfsmitteln und Quellen verwendet zu haben. Sowohl inhaltlich als auch wörtlich entnommene Stellen wurden als solche kenntlich gemacht.

Zudem erkläre ich, dass diese Arbeit nicht in dieser oder einer ähnlichen Form bei einer anderen Fakultät eingereicht wurde.

Niklas Cibura

Essen, im Juli 2019

10. Curriculum Vitae

Der Lebenslauf ist in der Online-Version aus Gründen des Datenschutzes nicht enthalten.

10. Curriculum Vitae

Der Lebenslauf ist in der Online-Version aus Gründen des Datenschutzes nicht enthalten.

10. Curriculum Vitae

Der Lebenslauf ist in der Online-Version aus Gründen des Datenschutzes nicht enthalten.